Dynamic and Quasi-Static Response of Warm and Hot Formed Aluminum Beams Under Three-Point Bending

by

Samuel Kim

A thesis

presented to the University of Waterloo

in fulfillment of the

thesis requirement for the degree of

Master of Applied Science

in

Mechanical and Mechatronics Engineering

Waterloo, Ontario, Canada, 2018

I hereby declare that I am the sole author of this thesis. This is a true copy of the thesis, including any required final revisions, as accepted by my examiners.

I understand that my thesis may be made electronically available to the public.

ABSTRACT

This thesis investigates the effect of elevated temperature forming on the impact resistance of three aluminum alloys, AA6013-T6, AA7075-T6, and a developmental 7000-series alloy (designated AA7xxx-T76). Both die quenching and warm forming processes were considered to investigate their potential to form high strength structural components for automotive applications. The die quenching process simultaneously forms and quenches the material from a solutionized condition to a supersaturated solid state solution (SSSS) after which aging treatments are applied to reach final strength. The warm forming process forms the material below the solutionization temperature.

In this work, the 7000-series aluminum alloys were die quenched and brought back to their original tempers with standard T6 or T76 aging treatments as well as experimental aging schedules (denoted with the letters “IPB” after the emulated temper designation) designed to incorporate the automotive paint bake cycle (177°C for 30 minutes). The IPB aging treatments reduce the aging time by 65-78% depending on alloy composition. After aging, the die quenched beams exhibited a Vickers hardness of 180 HV for AA7075-T6, 179 HV for AA7075-T6IPB, 166 HV AA7xxx-T76, and 166 HV for AA7xxx-T76IPB.

The three aluminum alloys were also warm formed under isothermal (blank and tooling heated to the same temperature) and non-isothermal (heated blank and room temperature tooling) conditions at 200°C and 233°C. The non-isothermal warm forming process resulted in a higher peak strength compared to the isothermal warm forming process for all alloys, but AA7075 was more susceptible to cracking when non-isothermally formed.

In addition, under aged AA6013 and AA7xxx blanks were warm formed and then subjected to a paint bake cycle. This processing route makes use of the thermal energy from the forming process and paint bake cycle to complete aging and increase the strength of the beams. The final result was a part that is at a near peak aged (T6 temper) condition. Additional optimization of the under-aged temper is necessary to further balance formability and peak strength.

All beams were then subjected to quasi-static three-point bend experiments, while the die quenched beams were also subjected to additional dynamic three-point bend tests. All warm formed material followed the same trend in which the non-isothermally formed beams had a 6-19.5% increase in force over a standard T6 condition, but had a higher tendency to fracture than their isothermally formed counterparts depending on alloy composition. The beams that were formed at the lower isothermal temperature had a 1.4-9.4% lower peak force but had similar fracture characteristics as the beams formed at a higher isothermal temperature. The peak force for the die quenched IPB and standard heat treatment scheduled beams were within 0-6% depending on the aluminum alloy composition. Both the IPB and standard heat treatment T6 or T76 beams exhibited the same fracture pattern.

Numerical models were developed using LS-DYNA to simulate the forming and subsequent three-point bend response of the die quenched beams. The models predicted the peak force to within 4% of the measured data.

ACKNOWLEDGEMENTS

First and foremost, I would like to thank my supervisors, Dr. Michael Worswick, for providing the invaluable opportunity to contribute to this research project and providing me with support and guidance throughout, and Dr. Clifford Butcher, whose direction in the development of the material and fracture models were vital for this project.

This project would not be possible without the immense support from our sponsors, Honda R&D Americas Inc., Arconic Ground Transportation Group, Promatek Research Centre, the Natural Sciences and Engineering Research Council, the Canada Foundation for Innovation, the Ontario Research Fund and the Canada Research Chairs Secretariat.

None of the experiments would be possible without the help of the lab technicians and Research Associates/Engineers: Andy Barber, Eckhard Budziarek, Tom Gawel, Ryan George, Richard Gordon, Mark Griffett, Neil Griffett, José Imbert, Karl Janzen, and Jeff Wemp.

Acknowledgements are due to the engineering and student machine shop: Graeme Adair, Fred Bakker, Charlie Boyle, Jorge Cruz, Rick Forgett, Rob Kaptein, Rob Kraemer, Mark Kuntz, Phil Laycock, Brian Shuh, and Andrew Urschel. Although I never needed to use either machine shops for this project, you guys were always fun to talk with and were never shy to impart your wisdom to me.

I would like to thank Kaab Omer and Taamjeed Rahmaan for being on “Team Die Quenching” with me, as well as the members of “Team Warm Forming/Italy,” Sante DiCecco and Massimo DiCiano for being worthy adversaries and allies.

Finally, I would like to thank my parents and sister for their support and encouragement during my years here.

Dedicated to my parents

Table of Contents

AUTHOR'S DECLARATION ii

ABSTRACT iii

ACKNOWLEDGEMENTS v

DEDICATION vii

LIST OF FIGURES xii

LIST OF TABLES xx

1 INTRODUCTION 1

1.1 Precipitation Hardening 4

1.2 Die Quenching Process 9

1.3 Warm Forming Process 12

1.4 Numerical Modeling of the Die Quenching Process 15

1.5 Numerical Modeling of Impact Experiments 18

1.6 Die Quench Material Characterization 23

1.7 Current Work 26

2 ELEVATED TEMPERATURE FORMING 28

2.1 Overview of Forming Program 28

2.2 Die Quenching Experiments 31

2.2.1 Die Quenching Forming Parameters 36

2.2.2 Die Quench Lubricant Selection 38
2.2.3 Post-Forming Heat Treatment 40
2.2.4 Microhardness Measurements of Die Quenched Parts 42
2.3 Warm Forming Experiments 43
2.3.1 Warm Forming Parameters 48
2.3.2 Warm Forming Lubricant 51
2.4 Test Matrix 51
3 STRUCTURAL THREE-POINT BEND EXPERIMENTAL METHODOLOGY 53
3.1 Three-Point Bend Test Specimen Preparation 53
3.2 Quasi-Static Test Setup 54
3.3 Dynamic Test Setup 56
4 NUMERICAL MODEL OF DIE QUENCHING AND SUBSEQUENT THREE-POINT BEND RESPONSE 60
4.1 Die Quenching Model 60
4.1.1 Modeling Strategy 60
4.1.2 Finite Element Mesh 61
4.1.3 Material Properties for the Tooling 63
4.1.4 Material Model for Blank 63
4.1.5 Model Parameters 66
4.2 Three-Point Bend Simulations 72
4.2.1 Material Constitutive Model and Failure Criteria 72
4.2.2 Three-Point Bend Meshes 78

4.2.3 Rivet Model 79
4.2.4 Boundary Conditions – Quasi-static Model 81
4.2.5 Boundary Conditions – Dynamic 82

5 EXPERIMENTAL RESULTS AND MODEL PREDICTIONS 83

5.1 Die Quenching Results 83
5.1.1 Effective Plastic Strain and Temperature History during Quenching 83
5.1.2 Thinning during Die Quenching 86
5.1.3 Measured Micro Hardness in Die Quenched Parts 87

5.2 Quasi-Static Three-point Bend Experiments 89
5.2.1 Warm Formed Beams 90
5.2.2 Die Quenched Beams 96

5.3 Dynamic Three-point Bend Test 98

5.4 Numerical Predictions 100
5.4.1 Calibration of Failure Criteria – Regularization Approach 100
5.4.2 Quasi-Static Numerical Model – Comparison with Experiment 106
5.4.3 Dynamic Numerical Model Comparison 110

5.5 Discussion 113

6 CONCLUSIONS AND RECOMMENDATIONS 121

6.1 Conclusions 121

6.2 Recommendations 122

7 Bibliography 124

Appendix A 142

Appendix B.....146

B.1 Quasi-static Warm Formed Three-Point Bend Test Data 146

B.2 Quasi-static Die Quenched Three-Point Bend Test Data 150

B.3 Dynamic Die Quenched Three-Point Bend Test Data 152

LIST OF FIGURES

Figure 1: Fuel economy standards for new passenger vehicles by country per year [1] 1

Figure 2: Next generation Audi A8 Space Frame design [15] 3

Figure 3: Qualitative representation of the evolution of strength and corrosion within the T7 temper [42] 7

Figure 4: Die quenching process for heat-treatable aluminum alloys [27].....10

Figure 5: Effects of solutionization temperature on hardness after T6 heat treatment for AA7050 [66] 11

Figure 6: Hardness vs. aging time for different quench rates [67].....12

Figure 7: Warm deep drawing tooling and process [22] 13

Figure 8: a) Percent elongation vs. strain rate and b) percent elongation vs. temperature for aluminum with varying percentage of magnesium [73] 14

Figure 9: Flow stress evolution as a function of strain rate at T=296 K and ε=0.1 [92] 19

Figure 10: Visual representation of damage within the surface of an element [98].22

Figure 11: MTS Criterion 49 tensile machine with MTS 651 furnace (left). Hydraulic grips and quenching nozzles (right) [110] 24

Figure 12: ASTM-E8 standard and subsize specimen geometry [111] 25

Figure 13: Dimensions (top) [100] and shape (bottom) of the pre-formed blank.....29

Figure 14: Impact beam cross-section and oblique view.....30

Figure 15: Beam geometry and nomenclature. 30

Figure 16: Furnace and door orientation [118].....32

Figure 17: Transfer system [118].....33

Figure 18: Forming tooling components and cooling channels 34

Figure 19: Nitrogen springs mounted on the die platform 35

Figure 20: Cross-sectional view of the tooling movement during the forming process 36

Figure 21: Surface quality for forming with a) no lubricant, b) OKS and c) PTFE Spray.....39

Figure 22: Visual representation of the post die quenching heat treatment schedules.....42

Figure 23: Epoxy resin puck with specimens mounted for micro-hardness measurements 43

Figure 24: 900 ton Macrodyne press and its components.....44

Figure 25: Oven placement with respect to the press and oven tray system.....45

Figure 26: Press and transfer system setup for warm forming 46

Figure 27: Heating cartridge, thermocouple and heating zone locations [127] 47

Figure 28: Measured temperature versus time history for AA7xxx quenched at 60 ton normal force....49

Figure 29: Backing plate dimensions and rivet pitch....54

Figure 30: Quasi-static Test Frame....55

Figure 31: a) Schematic of the quasi-static three-point bend setup [129] and b)test article placement....56

Figure 32: CAD drawing of the dynamic three-point test setup [129]....57

Figure 33: a) Photographs of sled and b) barrier wall assemblies....57

Figure 34: View from both cameras at the point of sled impact....58

Figure 35: The data acquisition laser trigger....59

Figure 36: Tooling discretization and orientation in numerical model....62

Figure 37: Temperature and strain rate-dependent hardening curves for AA7075 [110]....65

Figure 38: Temperature and strain rate-dependent hardening curves for AA7xxx [124]....65

Figure 39: Sinusoidal velocity profile of the die tooling....68

Figure 40: Cooling channel node locations....69

Figure 41: Hardening curves for AA7075-T6 [119]....73

Figure 42: Hardening curves for AA7xxx-T76 [119]....74

Figure 43: Hardening curves for AA6013-T6 [119] 74

Figure 44: Loci of failure strain versus stress triaxiality due to Rahmaan [139]. In this case, v-bend specimens were used to acquire the failure strains in the plane strain regime (triaxiality = 0.577). 76

Figure 45: Regularization curves for AA7075-T6 [139] 77

Figure 46: Regularization curves for AA6013-T6 [139] 77

Figure 47: Regularization curves for AA7xxx-T76 [139] 78

Figure 48: Backing plate mesh and location with respect to the channel 79

Figure 49: Rivet location and beam element nodes 80

Figure 50: Setup of the quasi-static three-point bend test model 81

Figure 51: Contours of effective plastic strain on top surface of the AA7075 channel during the die quenching simulation 84

Figure 52: Contour plot of predicted percent thickness reduction for die quenched AA7075 channel. 84

Figure 53: Contours of temperature during the die quenching simulation of AA7075 in degrees Kelvin 85

Figure 54: Simulated temperature drop of the blank during the die quenching process 85

Figure 55: Thickness specimen locations with respect to the channel length 86

Figure 56: Formed channel thickness measurement locations 87

Figure 57: Folding during quasi-static three-point bend loading in experiments (top) and simulation (bottom) 89

Figure 58: Experimental quasi-static force-displacement (left) and absorbed energy (right) comparison for warm formed AA6013 beams.....91

Figure 59: AA6013 folded region of a) 200°C isothermally formed b) 232°C isothermally formed c) 232°C non-isothermally formed d) under-aged beams.92

Figure 60: Experimental quasi-static force-displacement (left) and absorbed energy (right) comparison for warm formed AA7075 93

Figure 61: AA7075 folded region of a) 200°C isothermally formed b) 232°C isothermally formed c) 232°C non-isothermally formed 94

Figure 62: Experimental quasi-static force-displacement (left) and energy absorbed (right) comparison for warm formed AA7xxx 95

Figure 63: AA7xxx folded region of a) 200°C isothermally formed b) 232°C isothermally formed c) 232°C non-isothermally formed d) under-aged beams.96

Figure 64: Experimental quasi-static force-displacement (left) and energy absorbed (right) comparison for die quenched AA7075 97

Figure 65: Experimental quasi-static force-displacement (left) and energy absorbed (right) comparison for die quenched AA7xxx 97

Figure 66: Deformed AA7075-T6/T6IPB and AA7xxx-T76/T76IPB beams 98

Figure 67: Experimental dynamic force-displacement (left) and energy absorbed (right) comparison for die quenched AA7075 99

Figure 68: Experimental dynamic force-displacement (left) and energy absorbed (right) comparison for die quenched AA7xxx 100

Figure 69: Quasi-static regularization curve comparison for AA7075-T6 101

Figure 70: Dynamic regularization curve comparison for AA7075-T6 102

Figure 71: Quasi-static material failure for models using different regularization curves at set impactor displacement for AA7075-T6 104

Figure 72: Dynamic material failure for models using different regularization curves at set impactor displacement for AA7075-T6 105

Figure 73: Quasi-static die quenched AA7075-T6 and -T6IPB force-displacement comparison 106

Figure 74: Visual comparison of the predicted and measured region of fracture for AA7075-T6 107

Figure 75: Quasi-static die quenched AA7075-T6 energy absorbed comparison ...107

Figure 76: Quasi-static die quenched AA7xxx-T76 force displacement comparison 108

Figure 77 Quasi-static die quenched AA7xxx-T76 energy absorbed comparison ..109

Figure 78: Visual comparison of the predicted and measured region of fracture for AA7xxx-T76 110

Figure 79: Dynamic die quenched AA7075-T6 force-displacement comparison....111

Figure 80: Dynamic die quenched AA7075-T6 energy absorbed comparison.....111

Figure 81: Dynamic die quenchedAA7xxx-T76 force-displacement comparison ...112

Figure 82: Dynamic die quenched AA7xxx-T6 energy absorption comparison.....112

Figure 83: Measured peak force for all beams subjected to the warm forming processing route. Bars indicate average values, while scatter bars are indicated. 114

Figure 84: Measured absorbed energy for all beams subjected to the warm forming processing route at a punch displacement of 60 mm.....114

Figure 85: Peak force of all beams subjected to the die quench processing route 115

Figure 86: Absorbed energy for all beams subjected to the die quench processing route at a punch displacement of 60 mm 116

Figure 87: Peak force for the die quenched beams subjected to dynamic three-point bend loading.....117

Figure 88: Absorbed energy for the die quenched beams subjected to dynamic three-point bend loading at a sled displacement of 60 mm 117

Figure 89: Peak force comparison between warm forming and die quenching for AA7xxx.....118

Figure 90: Energy absorbed comparison between warm forming and die quenching for AA7xxx.....119

Figure 91: Peak force comparison between warm forming and die quenching for AA7075 119

Figure 92: Energy absorbed comparison between warm forming and die quenching for AA7075 120

Figure 93: Lap shear specimen with 5 kN rivet 142

Figure 94: Load versus displacement response of 5 kN rivets for lap shear test ..143

Figure 95: Cross tension fixture and specimen with 5 kN rivet 143

Figure 96: Load versus displacement response of 5 kN rivets for cross tension test 144

Figure 97: Coach peel test specimen with 5 kN rivet 144

Figure 98: Load versus displacement response of 5 kN rivets for coach peel test 145

Figure 99: Typical load versus displacement response for all three rivet strength tests 145

LIST OF TABLES

Table 1: Main alloying element in the alloy designation system [41] 5

Table 2: Subdivisions of T temper and their respective descriptions [41] 6

Table 3: Assigned additional digits to T7 temper [42] 7

Table 4: Nominal chemical compositions for AA6013-T6 [112], AA7075-T6 [113], and AA7xxx-T76 [114] 28

Table 5: Mechanical properties for AA6013-T6 [31], AA7075-T6 [68], and AA7xxx-T76 [115] 29

Table 6: Heat treatment schedule for AA7075-T6 [68] and the developmental AA7xxx-T76 [116] alloy 40

Table 7: IPB heat treatment schedules for AA7075 and AA7xxx [124] 41

Table 8: Under-aged heat treatment schedule for AA6013 and AA7xxx [126], [128] 50

Table 9: Under-aged warm forming parameters for AA6013 and AA7xxx [126], [128] 51

Table 10: Test matrix for forming and structural testing 52

Table 11: 5 kN Rivet measurements 54

Table 12: Elastic and thermal properties of tool steel [132], [133] 63

Table 13: Thermal properties of the blank [134].....64

Table 14: r-values to define the Barlat-89 yield surface in LS-DYNA for AA7075 and the developmental AA7xxx series alloy [119] 66

Table 15: Convection, radiation, and effective heat transfer coefficients 71

Table 16: Contact heat transfer coefficient vs applied pressure [124] 72

Table 17: Barlat YLD2000 coefficients for all three materials [139].....75

Table 18: 5 kN Rivet measurements 80

Table 19: Measured and predicted percent thickness reductions.....87

Table 20: Hardness measurements of die quenched beams at various locations in HV 88

1 INTRODUCTION

Strict government regulations and new standards to lower vehicle emissions and reduce environmental impact have driven automotive manufactures to make more fuel-efficient vehicles. In addition, fuel economy regulations are becoming increasingly more stringent every year globally as shown in Figure 1.

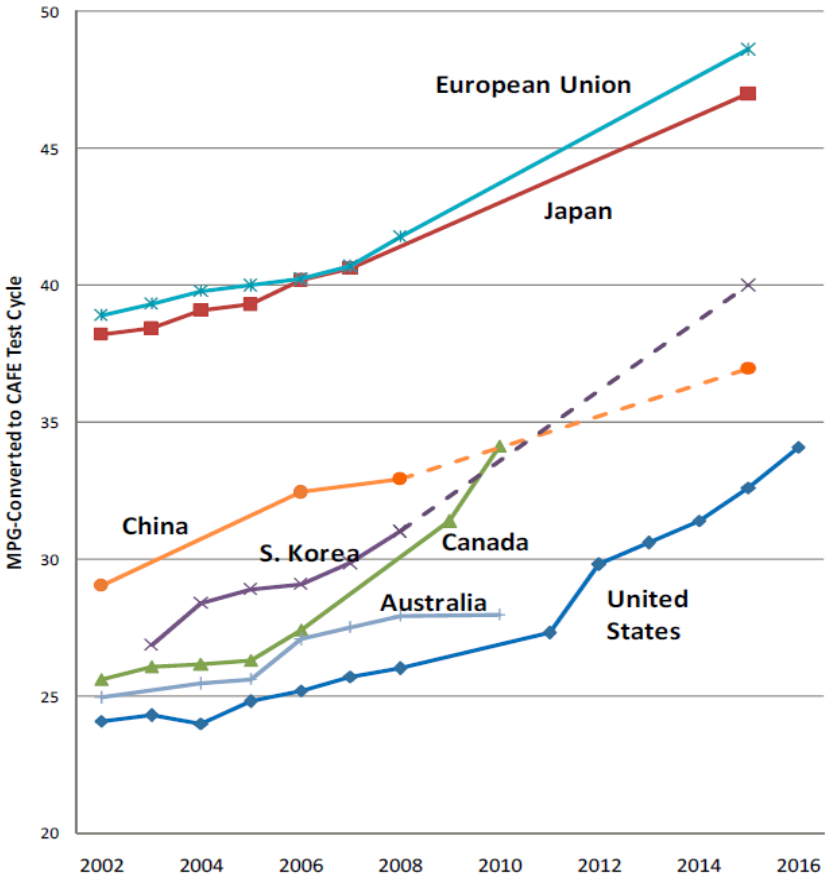

Figure 1: Fuel economy standards for new passenger vehicles by country per year [1]

Current standards include the Corporate Average Fuel Economy (CAFÉ) standard in the United States of America, which requires the fuel economy for cars and light-duty trucks to achieve 54.5 miles per gallon (mpg) by 2025 [2]. Given this very large increase in fuel economy by 2025, there is need for new and innovative

technologies to be implemented into high production vehicles in order for automotive companies to meet CAFÉ requirements.

Original equipment manufacturers (OEMs) can increase fuel economy by three primary means: more efficient powertrains [3]–[5], more refined aerodynamics [6], and decreasing vehicle mass [7]. All three approaches applied in parallel are thought necessary to achieve current targets [8], [9].

Reduction of vehicle mass is the main motivation for work done in this thesis. Automotive designers commonly decrease vehicle mass through introduction of lower density materials or higher strength (thinner) materials [10], [11]. Today, OEMs use steel extensively as the main material for major structural and non-structural components [12]. Over the past years, even though steel has evolved to have higher strength, such as the generation 3 advanced high-strength steels (AHSS), there is a need to incorporate more lower density materials to reduce the curb weight of vehicles [13], [14].

OEMs are considering materials such as aluminum, magnesium and composites, to reduce vehicular weight while still maintaining structural integrity and crashworthiness. A prominent example of the extent of lightweight materials being used in the body-in-white (BIW) is the Audi A8 Space Frame design. The components made of aluminum comprise 58% of the BIW, reserving steel only for the lower section of the front bulkhead, B-Pillar, side sills and the front section of the roofline as shown in Figure 2 [15].

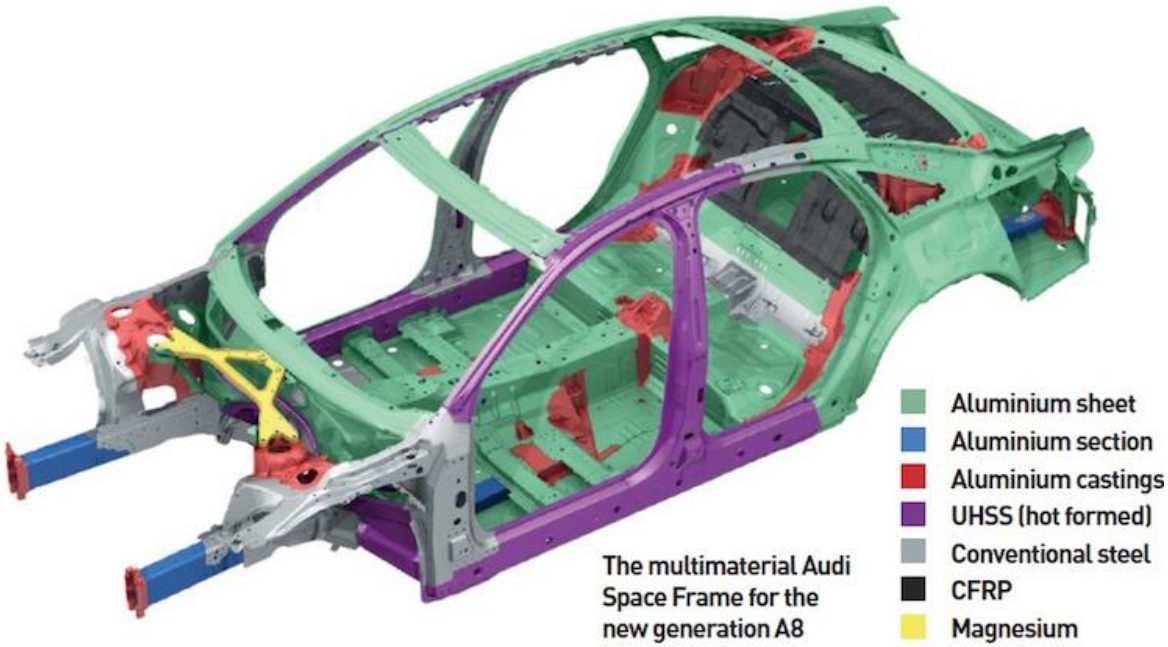

Figure 2: Next generation Audi A8 Space Frame design [15]

Aluminum alloys are attractive options to substitute conventional steel in automotive body and structural applications. High strength precipitation hardened aluminum alloys such as the 6000- and 7000-series alloys have good tensile strength, while being 30% of the weight of ultra-high-strength steels (UHSS). As a result, such alloys have strength-to-weight ratios that are comparable UHSS and has improved corrosion resistance.

The increase in strength for aluminum alloys comes with a caveat of having lower formability at room temperature [16]–[22].To increase formability and enable manufacturing of complex shaped structural components, elevated temperature forming is often used [23]–[27]. Unfortunately, under such conditions, the final strength of age hardenable alloys (*e.g.* 6000- and 7000- alloys) can be diminished due to over-aging of the aluminum [28]–[35].

One such method to improve formability while maintaining the strength of precipitation hardened aluminum is the die quench forming process [26], [27],

[36]–[40]. In die quenching, the blank is heated to the solutionizing temperature and quickly transferred to a cooled die and formed. The blank is simultaneously formed and quenched in the die, resulting in the final part to be in a super-saturated solid state (SSSS). This process is further explained in Chapter 1.2. The forming of the blank in the solutionizing temperature allows for high ductility and formability, making it ideal to manufacture complex shaped parts. The as-formed part will then require a subsequent artificial aging process to recover the material's strength.

Another method to improve formability and maintain the strength of precipitation hardened aluminum is the warm forming process. Warm forming involves heating the blank below the solutionization temperature and forming in either a die at room temperature or a heated die. The forming can take place in an isothermal or non-isothermal state, and the initial blank temperature can be varied depending on formability requirements and allowable strength degradation. The strength degradation of precipitation hardened aluminum is further explained in the next chapter.

1.1 Precipitation Hardening

Aluminum alloys are categorized by a four-number designation system based on major alloying elements, as can be seen in Table 1.

.

Table 1: Main alloying element in the alloy designation system [41]

Alloy	Main Alloying Element	Heat Treatable
1xxx	Mostly pure aluminum, no major alloying additions	No
2xxx	Copper	Yes
3xxx	Manganese	No
4xxx	Silicon	Yes
5xxx	Magnesium	No
6xxx	Magnesium and Silicon	Yes
7xxx	Zinc	Yes
8xxx	Other elements (*e.g.*, iron or tin)	No
9xxx	Unassigned	N/A

Table 1 shows that only a select series of alloys are capable of being solutionized and heat treated, 2xxx, 6xxx, 7xxx, while 4xxx can be depending on specific alloy composition.

After the numerical designation, there is a temper designation which is signified by the letters F, O, H, W, or T, which stands for as fabricated, annealed, strain hardened, solution heat-treated, and thermally heat-treated respectively. Due to the degree and amount of heat being applied to the material during and immediately prior to and after forming, the thermally heat-treated temper designations are of interest for this thesis. The different thermal tempers are shown in Table 2.

Table 2: Subdivisions of T temper and their respective descriptions [41]

Temper	Definition
T1	Cooled from elevated temperature-shaping process and naturally aged
T2	Cooled from elevated temperature-shaping process, cold worked, and naturally aged
T3	Solution heat treated, cold worked, and naturally aged
T4	Solution heat treated and naturally aged
T5	Cooled from an elevated temperature-shaping process and artificially aged
T6	Solution heat treated and artificially aged
T7	Solution heat treated and artificially over aged
T8	Solution heat treated, cold worked, and artificially aged
T9	Solution heat treated, artificially aged, and cold worked
T10	Cooled from an elevated temperature-shaping process, cold worked, and artificially aged

Each temper in Table 2 can be even further subdivided by adding a second number. In the case of this work, the subdivision of the T7 temper is of interest, due to its overaged nature. The overaging processes creates a compromise between exfoliation corrosion resistance, stress corrosion resistance, fracture toughness, and tensile strength. The variations of the T7 temper are shown in Table 3 and Figure 3 shows the qualitative evolution of strength and corrosion resistance with these tempers.

Table 3: Assigned additional digits to T7 temper [42]

Additional T7 Digits	Definition
T79	Very limited overaging to achieve some improved corrosion resistance with limited reduction in strength.
T76	Limited overaging to achieve moderate corrosion resistance with some reduction in strength.
T74	Overaging to achieve good corrosion resistance with greater reduction in strength.
T73	Full overaging to achieve best corrosion resistance of all T7 tempers
T77	Aged condition providing strength at or near T6 temper and corrosion resistance similar to T76 temper.

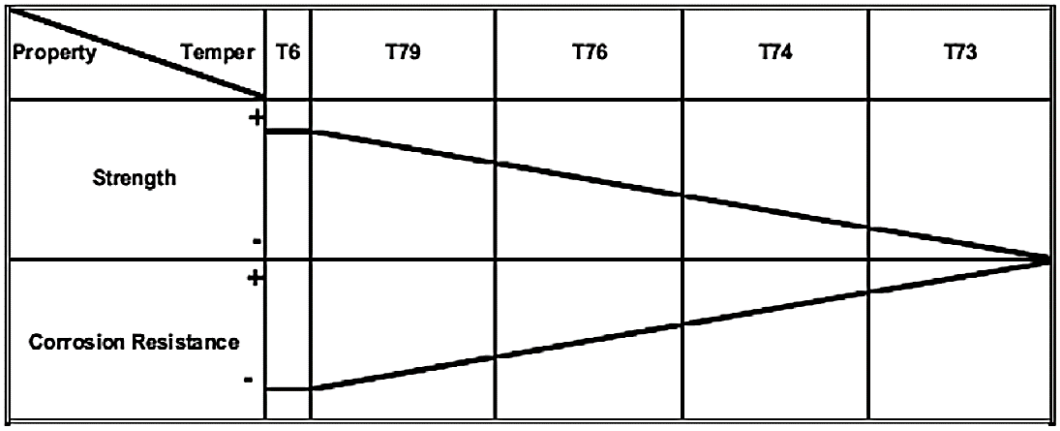

Figure 3: Qualitative representation of the evolution of strength and corrosion within the T7 temper [42]

The primary alloying elements are silicon and magnesium for 6000 series aluminum, and zinc and magnesium for 7000 series aluminum. In addition, manganese, copper, chromium and zirconium are also used to aid in the

precipitation process. The aluminum alloys are subjected to a heat treatment process to increase their strength through a precipitation hardening process.

The beginning of the precipitation hardening process begins when the alloy is heated to the solutionization temperature to dissolve the alloying elements into the aluminum matrix. Once dissolved, the alloy is quenched at a high enough rate to suppress precipitation during quenching, creating a homogenous super saturated solid solution, SSSS. From the SSSS state, the formation and growth of precipitates are divided into three stages: (1) nucleation of precipitates, (2) precipitate growth, and (3) coarsening of precipitates without change in volume fraction. The precipitates are classified as being coherent, semi-coherent, and incoherent. These classifications are dictated by their crystal structure and thus, their interfacial energy. Coherent precipitates have the same crystal structure and lattice spacing as their surroundings, having a higher interfacial energy due to the high amount of cohesion between structures. As the size of the precipitate increases, it becomes increasingly incoherent with the parent matrix, transitioning to semi-coherent, then incoherent precipitates.

The main alloying elements in creating strengthening precipitates are silicon (Si) and magnesium (Mg). The formation sequence of the strengthening precipitates for 6000-series aluminum are as follows [43]

$$SSSS \rightarrow GP(I) \rightarrow \beta''/GP(II) \rightarrow \beta' \rightarrow \beta$$

The main strengthening elements in both alloys are Mg and zinc (Zn). The formation sequence of the strengthening precipitates for 7000-series aluminum are as follows [28], [44].

$$SSSS \rightarrow GP\ Zones \rightarrow \eta' \rightarrow \eta$$

Although the formation sequence of precipitates is similar for both alloy series, the peak strength is attained at different stages for each series. The 6000-series alloy gains peak hardness by the precipitation of the β" within the main aluminum matrix. The β" precipitates form from spherical GP(I) particles to ordered clusters and zones of constituents which develop into a needle shape [43]. The needle-shape strengthening precipitates have been observed in various 6000-series alloys, including 6061 [45], 6056 [46], 6011 [47], 6016 [48], and 6022 [49].

For 7000-series aluminum, the peak hardness is attained when the η' precipitates form. The η' precipitate are metastable semi-coherent precipitates [28]. These metastable precipitates originate from thin platelet precipitates that grow into larger η' precipitates with platelet morphology [44].

1.2 Die Quenching Process

Extensive research has been done on the die quenching process with UHSS [50]–[53] since the quench rate from the austenitic state dictates the resulting steel microstructure and overall strength and ductility [54]–[56]. Only recently, within the last 10 years, has there been significant interest in die quenching aluminum [57]. These studies have their emphasis on lower strength precipitation hardenable aluminums such as 2xxx, 4xxx, and 6xxx series alloys [26], [27], [37], [38], [40]. With the need for higher strength lightweight material increases, there is a need for more research on higher strength precipitation hardenable aluminums such as the 7xxx series alloys.

The die quenching (DQ) process serves to overcome the low room temperature formability of precipitation hardened aluminum and allows its full potential to be exploited. As mentioned, the DQ process requires heating of the

aluminum blank to the solutionization temperature in order to dissolve all constituents into the aluminum matrix. Once the material is homogenized, it is quenched at a rapid rate while simultaneously being formed within a cooled die-set [26], [27], [40], [58]. The part is held in the die set to ensure that the material is fully quenched. The formed part is now in a SSSS and is subjected to specified heat treatments to control the precipitation hardening and achieve the appropriate mechanical properties [59]–[65]. The full process can be visualized in Figure 4.

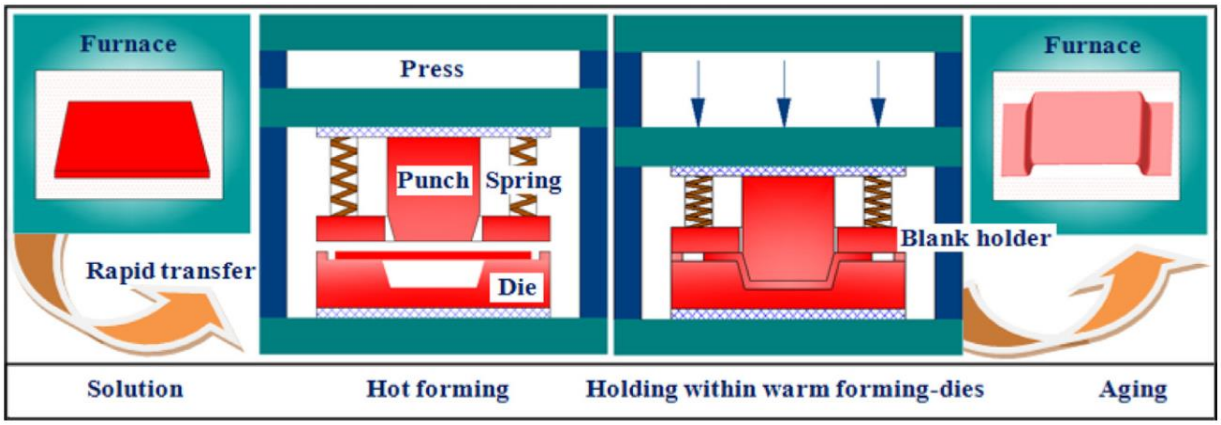

Figure 4: Die quenching process for heat-treatable aluminum alloys [27]

The benefits of die quenching are that there is minimal springback and thermal distortion due to the high cooling rate and lower material strength during forming [26]. The formed part can also be heat treated to any desired temper.

In die quenching, it is critical that the material reaches a SSSS state after forming in order to fully recover the material's strength post-forming. Therefore, the solutionization temperature, duration held at solutionization temperature and quench rate are very important. If the material is not at the solution temperature, or held for only a short duration, then not all of the precipitates will dissolve into the matrix and the strength potential of the material is compromised. The

material's dependency on the solutionization temperature has a significant impact on its overall peak strength, as shown in Figure 5.

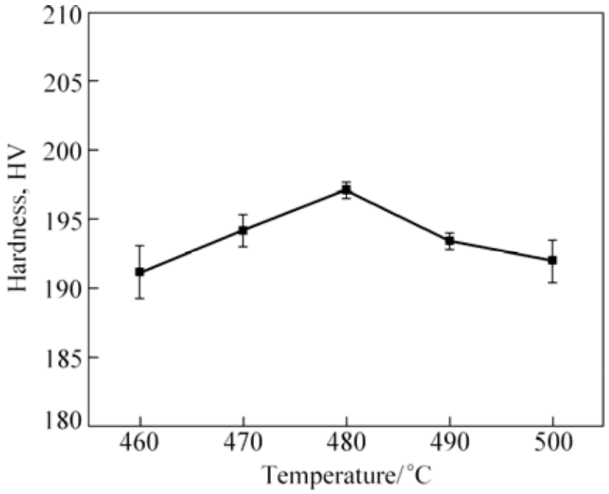

Figure 5: Effects of solutionization temperature on hardness after T6 heat treatment for AA7050 [66]

If the material is not quenched at a quick enough rate, unwanted quench-induced precipitates form within the aluminum matrix in a non-uniform manner. As a result, there is a lower volume fraction of solute present in the material to create fine-scaled precipitates during aging treatment which reduces the materials potential increase in strength [67]. This decrease in strength due to slower quench rates can be seen in Figure 6.

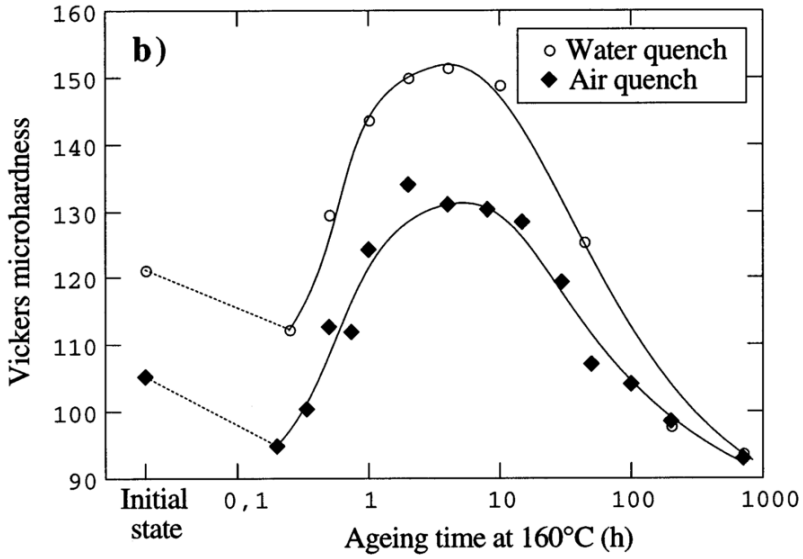

Figure 6: Hardness *vs.* aging time for different quench rates [67]

Once the material is in the SSSS state, the final temper can be tailored to the application. Typically most precipitation hardened aluminum will be used in application at a T6 temper, but achieving this requires up to a 24h aging treatment for some alloys [68].

1.3 Warm Forming Process

Warm forming consists of forming below the solutionization temperature and has been studied extensively for age-hardenable and strain hardening alloys [16], [17], [19], [21], [27], [27], [69]–[73]. Typically in the literature, warm formability of materials has been assessed using a warm deep drawing test [17], [21], [22], [69], [71], [72], [74]–[78]. The tooling and resulting specimen are shown in Figure 7.

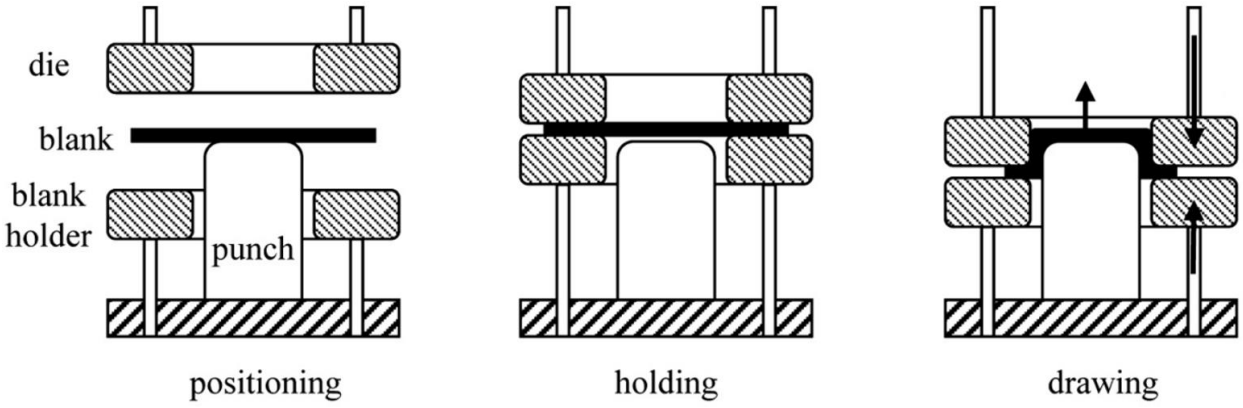

Figure 7: Warm deep drawing tooling and process [22]

Adding thermal energy has shown to significantly increase the ductility and formability of aluminum alloys, even at moderate temperatures of 150°C [76]. In comparison to die quenching, there are more complexities to consider when warm forming because of the wide range of blank and tooling temperatures that can be used. Therefore, the temperature of the blank, die, punch and blank holder needs to be properly calibrated for the material composition and temper.

It was shown that increasing tooling temperature uniformly resulted in improved formability [16]. Varying the temperature of the blank, binder and punch separately in so-called non-isothermal forming processes, allowed for even greater draw depths to be achieved by suppressing localized necking near the punch circumference compared to a uniform tooling temperature (isothermal) conditions [69], [72].

In addition to varying tool temperature, strain rate sensitivity at elevated temperatures was found to be another complexity associated with punch velocity. The combined effect of temperature and strain rate was studied and was found that percent elongation of the material increased with lower strain rates. This effect can be seen in Figure 8.

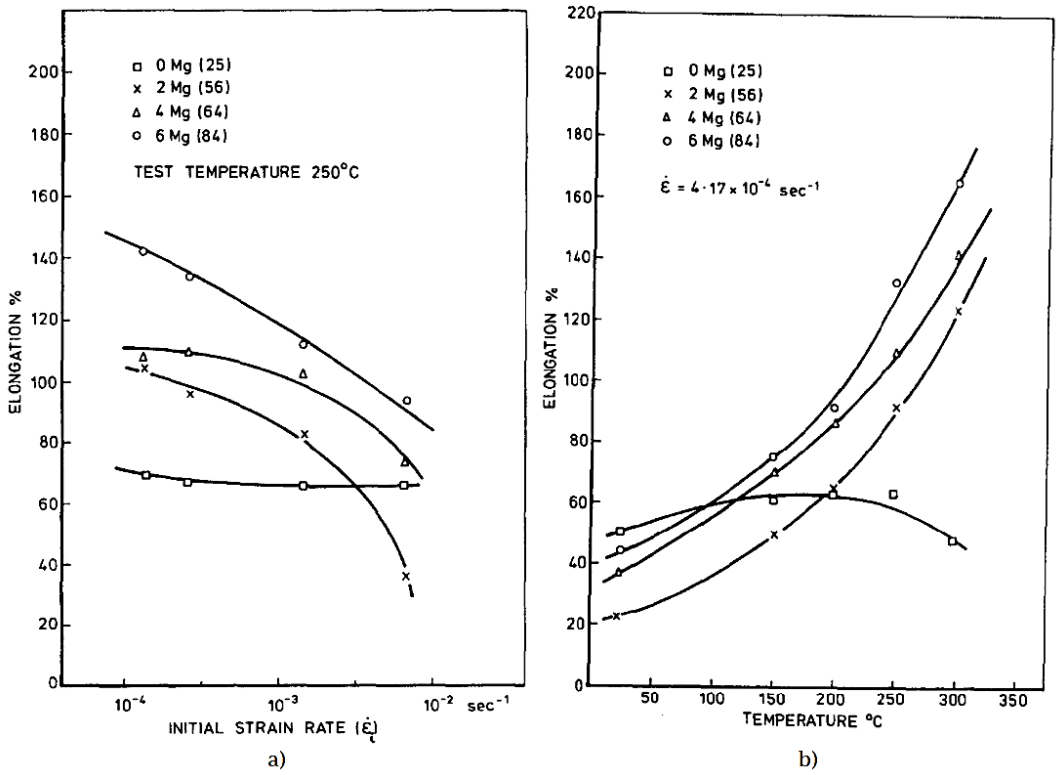

Figure 8: a) Percent elongation *vs.* strain rate and b) percent elongation *vs.* temperature for aluminum with varying percentage of magnesium [73]

It was also found that heating time also influenced the degradation of material strength [79]. Investigations showed that short heating times, within 2 minutes, were obtained using an infrared heater to heat the material to warm forming temperatures. The short heating time allowed for the material to exhibit high formability while retaining its peak strength after forming.

Another method of obtaining peak strength after warm forming of precipitation hardenable aluminum alloys is to apply the warm forming process to under-aged blanks. This would allow the material to experience only a brief moment of aging during the warm forming process and reach near peak strength. The crux would be discovering the appropriate under-aged temper and warm forming processing route that would allow material to reach peak strength after

forming. Currently, there are no published studies on warm forming precipitation hardenable aluminum in the under-aged state.

1.4 Numerical Modeling of the Die Quenching Process

Simulation of the die quenching process entails a two-part process, first the deformation of the blank into the desired shape, then the quenching process. The deformation process involves the behavior of the blank during the forming process including the plastic deformation, springback, and blank temperature. The quenching process involves the tooling temperature, heat transfer and boundary conditions.

To model the die quenching process, a coupled thermo-mechanical approach is utilized to increase accuracy at the cost of computational time [80]. The tooling is typically modelled using tetrahedral solids elements [39] or shell elements that are non-deforming and rigid.

The blank's material property during forming is largely dependent on the heat transfer between the blank and tooling which is dictated by the heat transfer coefficient (HTC). Similar to die quenching of steels, the HTC is governed by the contact pressure between the tooling and blank [54], [81]–[83]. The correlation between HTC and contact pressure can be calculated using mathematical formulas, or through experimental results.

Since temperature heavily influences the material properties during forming, a temperature-dependent constitutive model is necessary. Takuda *et al.* [75] captured the hardening behavior of AA5182-O under conditions corresponding to elevated temperature forming using a power-law plasticity equation and Keum *et al.* [84] used a rate sensitive power law plasticity equation that contained

temperature dependent coefficients. These can be seen in Equations 1 and 2, respectively.

$$\sigma = K\varepsilon_p^N \quad (1)$$

$$\sigma = K\varepsilon_p^N \dot{\varepsilon}_p^m \quad (2)$$

Where K is a stress constant and N is the strain-hardening exponent. In equation 2, $\dot{\varepsilon}_p$ is the plastic strain rate and m is the strain rate-hardening exponent.

Mohamed *et al.* [40] found the use of a rate sensitive material model resulted in more accurate results and determined that a strain-rate sensitive model was necessary for elevated temperature forming above $0.5T_m$.

Abedrabbo *et al.* [85] showed that temperature and strain dependent user defined material models (UMAT) more adequately capture the material behavior during forming. Such UMAT subroutines, in conjunction with a Barlat Yld96 [86] yield function, were used to create a constitutive model. This was further developed by replacing the Barlat Yld96 yield function to a Yld2000 [87] yield function.

The Barlat Yld96 is an anisotropic yield function that accounts for yield stress and Lankford parameters (r-value) directionalities. It is a phenomenological yield surface which utilizes a stress tensor with six components and follows the form:

$$\phi = \alpha_1|S_2 - S_3|^a + \alpha_2|S_3 - S_1|^a + \alpha_3|S_1 - S_2|^a = 2\bar{\sigma}^a \quad (3)$$

The coefficient a = 6 for BCC and a = 8 for FCC materials. The isotropic plasticity equivalent stress (IPE) [88] is defined as:

$$S = L\sigma \quad (4)$$

The fourth order tensorial operator, L, is defined as:

$$L = \begin{bmatrix} \frac{(c_2+c_3)}{3} & \frac{-c_3}{3} & \frac{-c_2}{3} & 0 & 0 & 0 \\ \frac{-c_3}{3} & \frac{(c_3+c_1)}{3} & \frac{-c_1}{3} & 0 & 0 & 0 \\ \frac{-c_2}{3} & \frac{-c_1}{3} & \frac{(c_1+c_2)}{3} & 0 & 0 & 0 \\ 0 & 0 & 0 & c_4 & 0 & 0 \\ 0 & 0 & 0 & 0 & c_5 & 0 \\ 0 & 0 & 0 & 0 & 0 & c_6 \end{bmatrix} \quad 5$$

For plane stress where ($\sigma_z = \sigma_{yz} = \sigma_{xz} = 0$), equation 4 reduces to:

$$S_{ij} = \begin{bmatrix} S_x \\ S_y \\ S_z \\ S_{xy} \end{bmatrix} = \begin{bmatrix} \frac{(c_2+c_3)}{3} & \frac{-c_3}{3} & \frac{-c_2}{3} & 0 \\ \frac{-c_3}{3} & \frac{(c_3+c_1)}{3} & \frac{-c_1}{3} & 0 \\ \frac{-c_2}{3} & \frac{-c_1}{3} & \frac{(c_1+c_2)}{3} & 0 \\ 0 & 0 & 0 & c_6 \end{bmatrix} \begin{bmatrix} \sigma_x \\ \sigma_y \\ 0 \\ \sigma_{xy} \end{bmatrix} \quad 6$$

The principle values of S_{ij} for equation 1 are as follows:

$$S_{1,2} = \frac{S_x + S_y}{2} \pm \sqrt{\left(\frac{S_x - S_y}{2}\right)^2 + S_{xy}^2}$$

$$S_3 = -(S_1 + S_2) \quad 7$$

The coefficients $c_{1\text{-}6}$, and $\alpha_{1\text{-}3}$ are the anisotropic coefficients that are derived experimental material testing data.

The Barlat Yld2000 yield function better describes the aluminum alloys subjected to the plane stress condition and is as follows:

$$\phi = |X_1' - X_2'|^a + |2X_2'' - X_1''|^a + |2X_1'' - X_2''|^a = 2\bar{\sigma}^a \quad 8$$

The exponent a is the same as in equation 3. The stress tensor undergoes two separate linear transformation:

$$X' = L'\sigma \qquad X'' = L''\sigma \quad 9$$

L' and L'' are defined as follows:

$$\begin{bmatrix} L'_{11} \\ L'_{12} \\ L'_{21} \\ L'_{22} \\ L'_{66} \end{bmatrix} = \begin{bmatrix} \frac{2}{3} & 0 & 0 \\ \frac{-1}{3} & 0 & 0 \\ 0 & \frac{-1}{3} & 0 \\ 0 & \frac{2}{3} & 0 \\ 0 & 0 & 1 \end{bmatrix} \begin{bmatrix} \alpha_1 \\ \alpha_2 \\ \alpha_7 \end{bmatrix} \qquad \begin{bmatrix} L''_{11} \\ L''_{12} \\ L''_{21} \\ L''_{22} \\ L''_{66} \end{bmatrix} = \frac{1}{9} \begin{bmatrix} -2 & 2 & 8 & -2 & 0 \\ 1 & -4 & -4 & 4 & 0 \\ 4 & -4 & -4 & 1 & 0 \\ -2 & 8 & 2 & -2 & 0 \\ 0 & 0 & 0 & 0 & 9 \end{bmatrix} \begin{bmatrix} \alpha_3 \\ \alpha_4 \\ \alpha_5 \\ \alpha_6 \\ \alpha_7 \end{bmatrix} \qquad 10$$

The coefficients $\alpha_{1\text{-}8}$ are determined from uniaxial tensile yield stress with specimens orientated 0°, 45° and 90°, and the yield stress and r-value from a biaxial tension test. The principle values of *X'* and *X''* are defined as follows:

$$X_{1,2} = \frac{1}{2}\left(X_{xx} + X_{yy} \pm \sqrt{\left(X_{xx} - X_{yy}\right)^2 + 4X_{xy}^2}\right) \qquad 11$$

Mohamed *et al.* [40] used constitutive equations that couple deformation and damage have been used to predict failure in forming in die quenching. The failure model was phenomenological and describes damage based on dislocation density. The model uses a strain rate dependent power law equation. The plastic strain rate term is replaced with an equation involving terms that relate material hardening with normalized dislocation density.

1.5 Numerical Modeling of Impact Experiments

The strain rates seen in metallic structures undergoing dynamic loading can reach $500s^{-1}$ [89]. It was found that in Al-Mg alloys, for strain rates below 10^{-1} s, the maximum flow stress decreases with increases in strain rate but increases above this rate [90], [91]. It was found that the negative strain rate sensitivity at lower strain rates was caused by dynamic strain aging due to the Portevin-Le Chatelier (PLC) effect. At elevated strain rates, PLC band propagation is suppressed. This trend can also be seen in Al-Mg-Si and Al-Zn alloys, as well shown in Figure 9 [92].

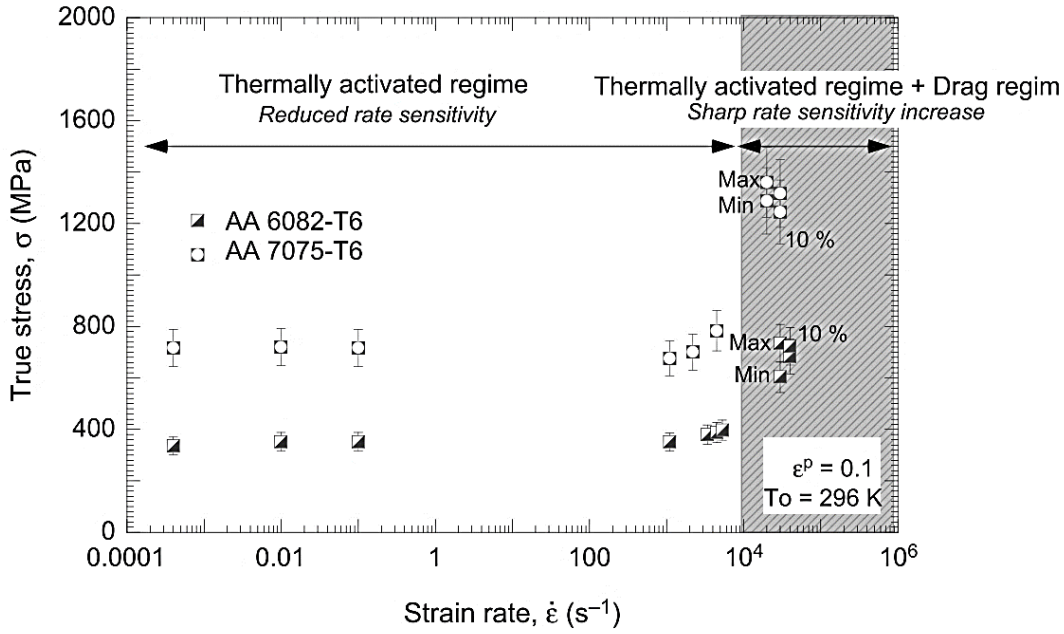

Figure 9: Flow stress evolution as a function of strain rate at T=296 K and ε=0.1 [92]

To capture the evolving material behavior due to strain, strain rate, and temperature, multiple models have been developed. Johnson-Cook [93], Zerilli-Armstrong [94], modified Voce [95], and Hockett-Sherby [96] are some of the models that have been developed over the years.

The Johnson-Cook model is shown below:

$$\sigma_{true} = (A + B\varepsilon_p^n)(1 + Cln(\dot{\varepsilon}^*))(1 - T^{*m}) \qquad 12$$

where σ_{true} is the true stress, ε is the equivalent plastic strain, $\dot{\varepsilon}^*$ is the normalized strain rate from the reference strain ε_0, and T^{*m} is the thermal softening term. The material constants are defined as follows: A is the yield stress, B and n are the hardening behavior, C is the strain rate sensitivity and m is the material softening term.

The Zerilli-Armstrong material model initially was developed for high strain rate conditions and moderate temperatures, but also serves to model higher

temperature conditions depending on crystal structure. The general form of the Zerilli-Armstrong equation and the elevated temperature equation for FCC material is given below:

$$\sigma = \Delta\sigma_G + \Delta\sigma_{thermal} + kl^{-0.5} \quad (13)$$

$$\sigma_{thermal} = C_2\varepsilon^{0.5}\exp(-C_3T + C_4Tln\dot{\varepsilon}) \quad (14)$$

where $\Delta\sigma_G$ represents the athermal stress component, $kl^{-1/2}$ represents the grain size, $\Delta\sigma_{thermal}$ incorporates the thermal and strain rate effects, C_i are material constants, ε and $\dot{\varepsilon}$ are equivalent strain and strain rate, and T is the absolute temperature.

The Voce material model allows for the capturing of stress saturation that is observed in some material behavior at larger strains. The Voce model is shown below:

$$\sigma_V(\varepsilon_p) = \left[\sigma_{sat} + (\sigma_y - \sigma_{sat})e^{\left(\frac{-\varepsilon_p}{\varepsilon_r}\right)}\right] \quad (15)$$

where σ_{sat} is the saturation stress, σ_y is the yield stress, ε_p is effective plastic strain and ε_r is the relaxation strain.

The Hockett-Sherby model also captures the stress saturation and is shown below:

$$\sigma_{flow} = \sigma_{sat} - e^{\left(-(N\varepsilon_p)^k\right)}(\sigma_{sat} - \sigma_y) \quad (16)$$

where many of the terms used in the Voce correspond to those in the Hockett-Sherby model, with N and k being calibration parameters.

Another aspect in properly modeling material behavior in loading experiments is accounting for failure. Failure can be characterized by a micromechanical damage model, resulting in a physically-based approach to

fracture, or a continuum damage model, which relates damage to a global material level with parameters which are often phenomenological.

Physically based approaches model material softening and ductile fracture through the nucleation, growth and coalescence of voids within non-homogeneous unit cell representations of the material microstructure [97]. Due to their complexity, such models are computationally expensive and difficult to implement in industry.

Instead, Lemaitre [98] introduced a continuum damage model where a damage parameter is used in calculations based on void nucleation and growth. This approach considers the material at a macroscopic scale and simplifies all microcracks and cavities (damage) within an element surface into one parameter. The damage parameter can be seen below:

$$D = \frac{S_D}{S} \qquad 17$$

where D is the damage parameter, S is the total surface area of the element defined by a normal vector and S_D is the total area of voids and microcracks within a specified element surface. Subtracting the total area of the element with the area of the voids, an updated, and increased effective stress is calculated. This can be seen in Figure 10 below.

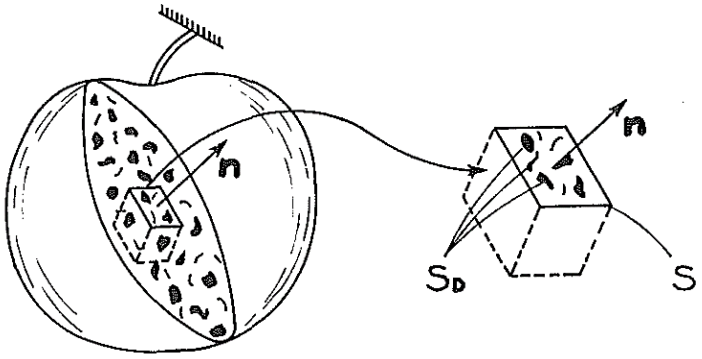

Figure 10: Visual representation of damage within the surface of an element [98]

When D=0, the element is in an undamaged state, when D=1, the element is damaged and resulting in rupture of the element, when 0<D<1 then the element is in a damaged state.

A common approach included in LS-DYNA is the generalized incremental stress state dependent damage model (GISSMO) [50], [99]–[101]. This damage model was developed to capture ductile fracture of materials and was developed by Daimler and DYNAmore [102]. The GISSMO model defines the damage term as a scalar parameter as follows:

$$D = \left(\frac{\varepsilon_p}{\varepsilon_f}\right)^n \tag{18}$$

where ε_p is the plastic strain and ε_f is the equivalent plastic strain at failure. The above equation is only valid for proportional loading. To capture the damage evolution at varying stress states, an incremental damage model is necessary as follows:

$$dD = \frac{n}{\varepsilon_f(\eta,\xi)} D^{\frac{n-1}{n}} d\varepsilon_p \tag{19}$$

where dD is the incremental damage, n is the non-linearity exponent, D is the current damage, $d\varepsilon_p$ is the incremental plastic strain, and ε_f is the failure strain.

When the above equation is integrated, the current damage is found and is as follows:

$$D = \int \frac{n}{\varepsilon_f(\eta,\xi)} D^{\frac{n-1}{n}} d\varepsilon_p \qquad 20$$

Similar to equation 17, when D is null, the element is undamaged and when D reaches unity, the element is deleted.

The failure strain used in the GISSMO damage model is a function of stress triaxiality and is measured experimentally. These fracture points are then used to create a fracture locus. Studies have shown that calibration of the fracture locus should account for Lode angle parameter to maintain accuracy [103], [104]. A fracture locus that includes both triaxiality and Lode angle parameter is the Bai-Wierzbicki [103] model:

$$\hat{\varepsilon}_f(\eta,\xi) = \left[\frac{1}{2}(C_1 e^{-C_2\eta} + C_5 e^{-C_6\eta}) - C_3 e^{-C_4\eta}\right]\xi^2 + \frac{1}{2}(C_1 e^{-C_2\eta} - C_5 e^{-C_6\eta})\xi + C_3 e^{-C_4\eta} \qquad 21$$

where $C_{1\text{-}6}$ are material constants found experimentally.

1.6 Die Quench Material Characterization

Literature typically obtains the flow stress curve of a material at an elevated temperature isothermally, where the material is heated to a desired temperature and then tested at that temperature [40], [105]–[109]. These data sets are not of use because unlike other forming processes, the die quenching process requires the material to first be solutionized and then formed such that the deformation occurs after the material reaches the solutionization temperature. In order to properly characterize the material, it must be at a SSSS immediately prior to the mechanical testing.

Omer et al [110] conducted tensile tests to determine the stress-strain properties that is required to properly model the die quenching process. The tensile tests were done with the AA7075 and the developmental 7xxx series material. The testing was done on a servo-hydraulic MTS Criterion 49 machine with hydraulic high-temperature grips. This machine accommodates the MTS 651 furnace to bring the test article to temperature, shown in Figure 11.

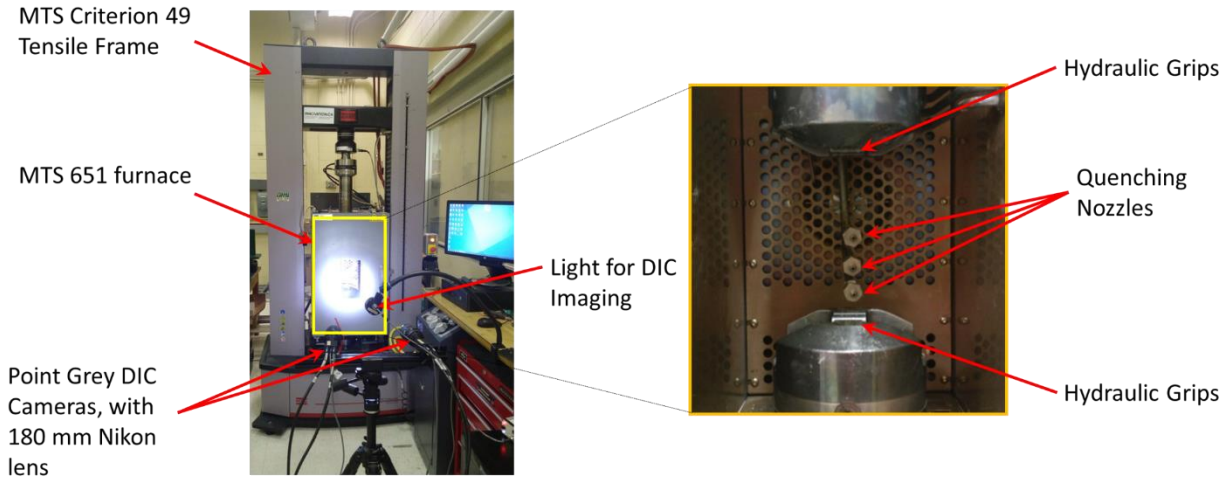

Figure 11: MTS Criterion 49 tensile machine with MTS 651 furnace (left). Hydraulic grips and quenching nozzles (right) [110]

The material was tested under three different strain rates, 0.01 s^{-1}, 0.1 s^{-1}, and 0.5 s^{-1}. The 0.01 s^{-1} and 0.1 s^{-1} tests used the ASTM-E8 standard geometry [111] while the 0.5 s^{-1} used a subsize ASTM-E8 geometry and the dimensions can be seen in Figure 12.

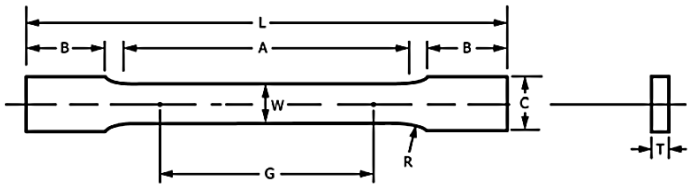

	Dimensions		
	Standard Specimens		Subsize Specimen
	Plate-Type, 40 mm [1.500 in.] Wide	Sheet-Type, 12.5 mm [0.500 in.] Wide	6 mm [0.250 in.] Wide
	mm [in.]	mm [in.]	mm [in.]
G—Gauge length (Note 1 and Note 2)	200.0 ± 0.2 [8.00 ± 0.01]	50.0 ± 0.1 [2.000 ± 0.005]	25.0 ± 0.1 [1.000 ± 0.003]
W—Width (Note 3 and Note 4)	40.0 ± 2.0 [1.500 ± 0.125, -0.250]	12.5 ± 0.2 [0.500 ± 0.010]	6.0 ± 0.1 [0.250 ± 0.005]
T—Thickness (Note 5)		thickness of material	
R—Radius of fillet, min (Note 6)	25 [1]	12.5 [0.500]	6 [0.250]
L—Overall length, min (Note 2, Note 7, and Note 8)	450 [18]	200 [8]	100 [4]
A—Length of reduced parallel section, min	225 [9]	57 [2.25]	32 [1.25]
B—Length of grip section, min (Note 9)	75 [3]	50 [2]	30 [1.25]
C—Width of grip section, approximate (Note 4 and Note 9)	50 [2]	20 [0.750]	10 [0.375]

Figure 12: ASTM-E8 standard and subsize specimen geometry [111]

In order to replicate the die quenching process, the oven was heated to 470°C and the tensile specimens were solutionized while being held within the grips of the test apparatus. Once at SSSS, the specimens were quenched using cold pressurized air from three nozzles within the furnace seen in Figure 11. The air was fed from a vortex chiller with an exit temperature of 4°C. The tensile specimens were quenched to six different temperatures: 25°C, 115°C, 200°C, 300°C, 400°C, 470°C. The temperature of 115°C was chosen because the quenching apparatus could not reach 100°C at a high enough quench rate. Once at the desired temperature, the tensile test began.

The 25°C specimens were heated in a separate convection furnace away from quenched in a set of flat quenching dies mounted on a separate forming press. Once quenched it was then immediately put into the tensile frame grips and tested at room temperature.

1.7 Current Work

The work done in this thesis is part of a broader project that is sponsored by Honda R&D Americas, Arconic Ground Transportation Group, and Promatek Research Centre. The purpose and goals of the overall project are to evaluate different thermo-mechanical processing routes for precipitation hardened aluminum alloys, develop constitutive models of the as-processed material behavior, and assess these models through the simulation of component-level forming and impact experiments.

The thermo-mechanical processing routes examined are die quenching and warm forming. These processing routes can significantly improve the formability of precipitation hardened aluminum alloys while maintaining the strength of the overall part. Most of the work described in the foregoing literature review were experiments done with the deep draw and hemispherical dome tests. There is very little published work on investigating aluminum alloys formed into structural components using the above-mentioned processing routes, such as component-level impact beams.

In the current work, component-level impact beams were formed using both the warm forming and die quenching processing routes. The materials considered are high strength 6000- and 7000-series aluminum alloy sheet, as described in Chapter 2 of this thesis. The forming experiments considered both as-received material, as well as custom tempers and aging treatments. A key aspect of this research has been to assess the use of so-called under-aged (UA) tempers as a starting point for warm forming such that the combination of the warm forming operation and subsequent paint bake cycle used in automotive manufacturing will result in a desirable final temper (strength) condition. In addition, custom aging

treatments after die quenching, that leverage the paint bake thermal cycle to complete aging will also be considered.

The formed parts were subjected to quasi-static and dynamic three-point bend tests to assess the material performance under each forming condition. In addition, non-linear finite element analysis was used to model the die-quenching forming process and structural tests in order to assess the capabilities of current modeling techniques.

The balance of this thesis is organized as follows. Chapter 2 describes the experimental forming procedure for both warm forming and die quenching processes, as well as the determination of their respective forming and heat treatment process parameters. Chapter 3 describes the quasi-static and dynamic three-point bend structural testing of the formed parts. Chapter 4 describes the forming modeling and three-point bend simulations. Chapter 5 describes the experimental results and numerical simulations, and makes comparisons between model and experiment. Chapter 6 presents the conclusions drawn from this research and recommendations for future work.

2 ELEVATED TEMPERATURE FORMING

2.1 Overview of Forming Program

A series of structural channel sections were fabricated using the warm forming and die quenching processes and then subjected to quasi-static and dynamic structural testing in order to ascertain the effect of forming process on mechanical response.

Three different aluminum alloys were investigated, AA6013, AA7075, and a developmental 7000-series alloy, herein designated AA7xxx, with initial tempers being T6, T6, and T76, respectively, and initial thickness of 2 mm. The nominal chemical compositions and mechanical properties for all three alloys is given in Table 4 and Table 5.

Table 4: Nominal chemical compositions for AA6013-T6 [112], AA7075-T6 [113], and AA7xxx-T76 [114]

	AA6013-T6	AA7075-T6	AA7xxx-T76
Aluminum	94.9-96.9%	87.1-91.4%	87.6-90.4%
Zinc	0.25%	5.1-6.1%	7-8%
Magnesium	0.8-1.2%	2.1-2.9%	1.2-1.8%
Copper	0.6-1.1%	1.2-2.0%	1.3-2%
Zirconium	Negligible	Negligible	0.08-0.15%
Iron	0.5%	0.5%	0.08%
Chromium	0.10%	0.18-0.28%	0.04%
Silicon	0.6-1.0%	0.4%	0.06%
Manganese	0.2-0.8%	0.3%	0.04%
Titanium	0.10%	0.2%	0.06%

Table 5: Mechanical properties for AA6013-T6 [31], AA7075-T6 [68], and AA7xxx-T76 [115]

	AA6013-T6	AA7075-T6	AA7xxx-T76
Density [g/cm^3]	2.71	2.81	2.85
Elastic modulus [GPa]	69.6	71.7	69.6
Yield Strength [MPa]	370	503	476
Ultimate Tensile Strength [MPa]	405	572	510
Percent Elongation [%]	9	11	7

Figure 13 shows the blank geometry which was common to both forming processes. The blank has tabs on both ends to position the blank on alignment pins incorporated in the tooling.

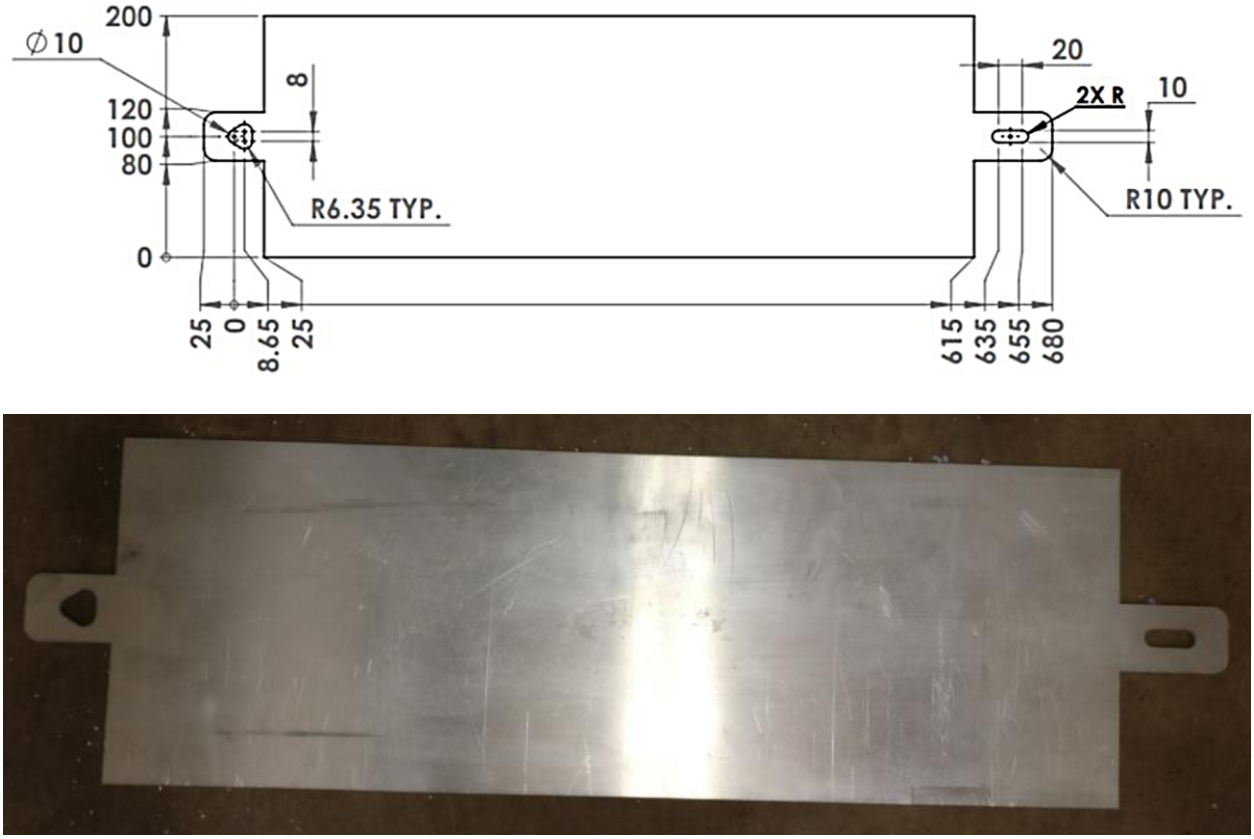

Figure 13: Dimensions (top) [100] and shape (bottom) of the pre-formed blank

The formed channels have a top hat cross-section with flanges on both sides and a c-channel section in between, shown in Figure 14.

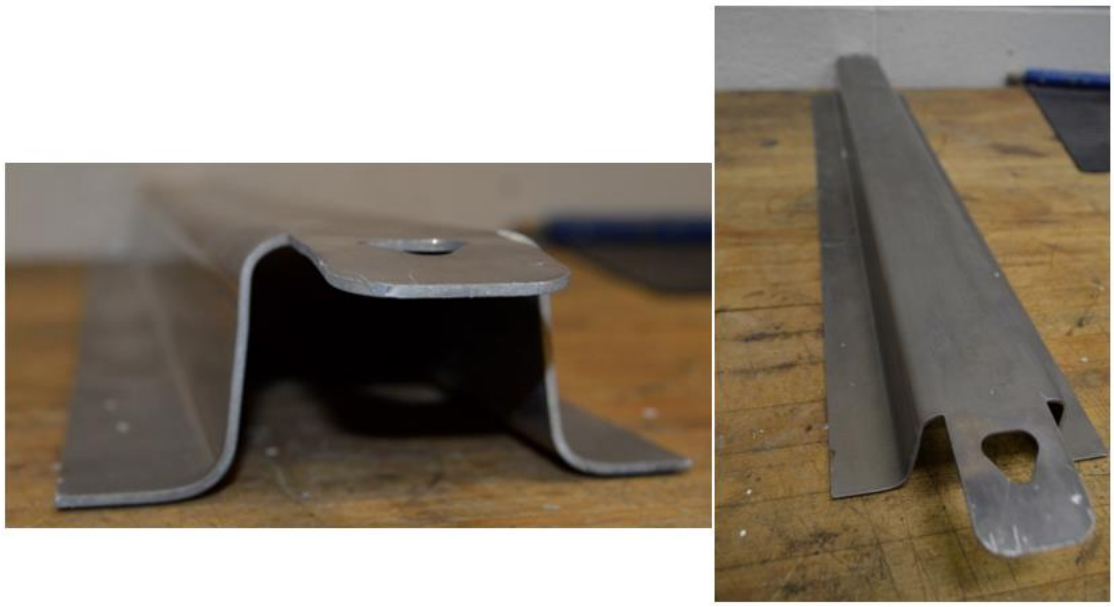

Figure 14: Impact beam cross-section and oblique view

The width of the beam is 120mm and length is 595mm. The nomenclature and dimensions of the beam can be seen in Figure 15. A backing plate is added to the channel section to close the cross-section, as also shown in the figure (and described in greater detail in Chapter 3).

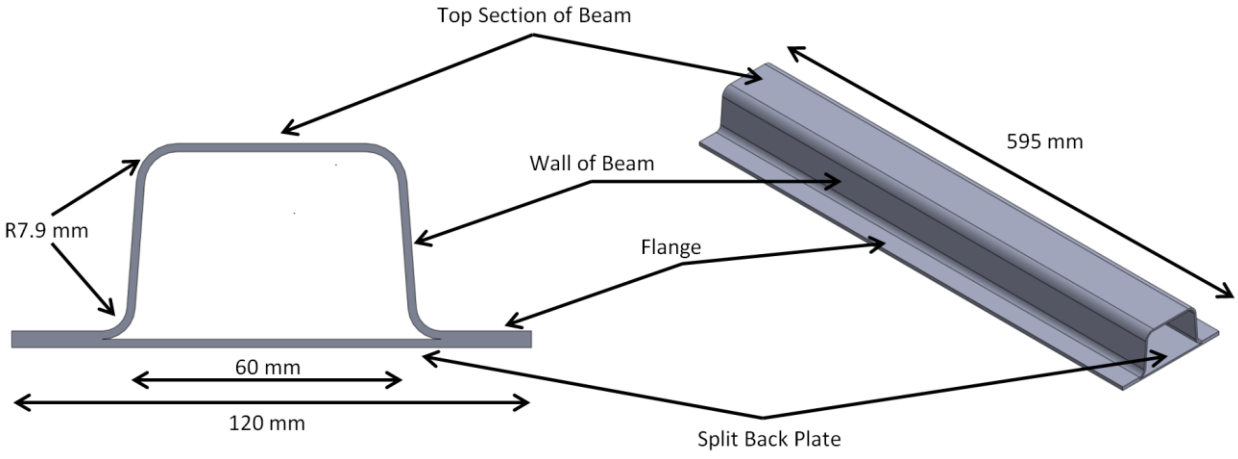

Figure 15: Beam geometry and nomenclature.

As described in Chapter 1, the die quench process allows for full customization of the final temper of the material through specific post-forming heat treatments. This allows the user to tailor the temper according to the required strength, corrosion resistance, and allotted time for aging. The heat treatments to achieve the ideal T6 temper from a SSSS are very lengthy, for most alloys taking upwards of 24 hours [68], [116]. One approach to shorten the heat treatment time is to leverage the paint bake cycle that vehicles go through during manufacturing. The paint bake cycle nominally corresponds to 177°C for 30 minutes [117]. This approach was considered in the experiments as detailed in Section 2.2.3

In warm forming, it is desired to achieve peak aging at the end of forming process; one approach is to form the blank in an under aged starting condition prior to warm forming and paint bake processing. Initial under-aged tempers were explored with the selected forming temperatures and durations to achieve the optimal peak temper. This is further explained in Section 2.3.1.2

The balance of this chapter serves to detail the forming experiments, while the structural testing methodology is described in Chapter 3.

2.2 Die Quenching Experiments

The die quenched impact channels were formed in a 120 Ton hydraulic press manufactured by Macrodyne Technologies Inc. The press has a bed that measures 1372 mm by 762 mm. The hydraulic system incorporates two 15 gallon hydraulic accumulators and a 100 GPM servo valve that enable the 120 Ton actuator to move at a rate of 254mm/s [118].

The press operates under closed-loop position control through a MTS FlexTest servo controller. A custom LabVIEW program controls a PC-based Digital-

to-Analog data acquisition (DAQ) card creating the program signals. Displacement of the punch was measured using a string potentiometer and load measurements were calculated from the difference in pressure within the oil inlet and outlet of the actuator and the pressurized areas. The pressure on the actuator was measured with pressure transducers and recorded using Analog-to-Digital channels on the DAQ card used by the controller.

To heat the blank to the solutionization temperature, a custom-built furnace manufactured by Deltech Inc. was used, shown in Figure 16. The furnace was located as close as possible to the tooling to reduce heat loss from the blank during transfer. The internal height, width, and depth of the furnace were 610 mm, 203 mm and 915mm respectively. The furnace has a pneumatically powered door at the front.

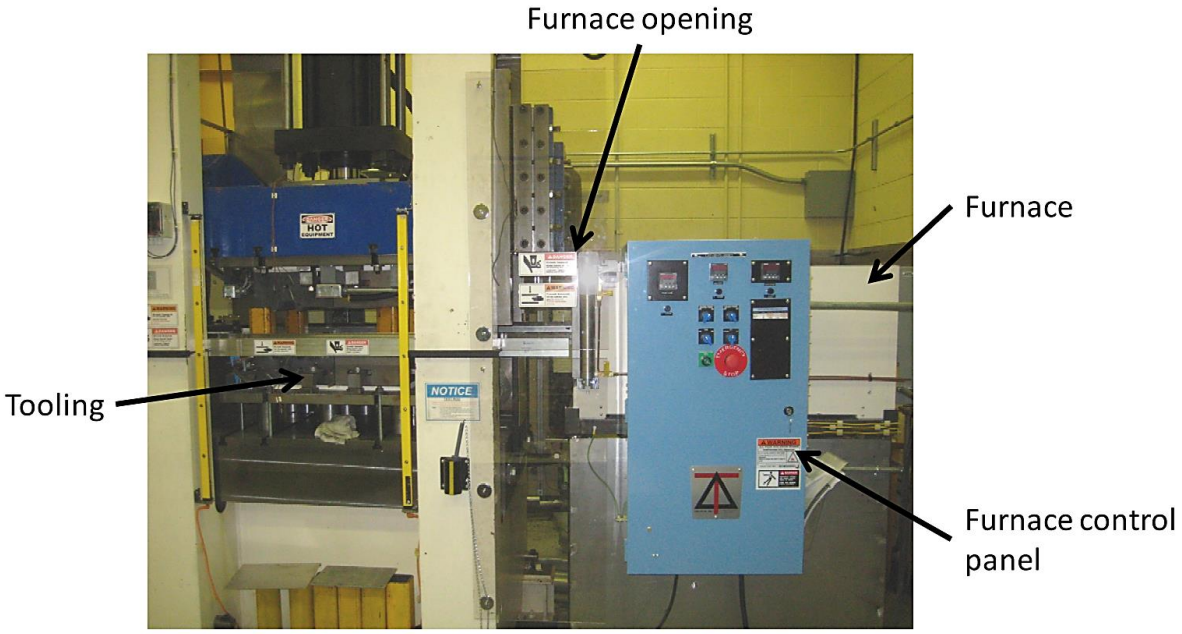

Figure 16: Furnace and door orientation [118]

The furnace has a heating capacity of 18kW and a total of six heating elements, three each along the top and bottom of the furnace. The heaters are

equally spaced along the length of the furnace to ensure uniform heating. The furnace is separated into three regions along its length, front, middle and back. The front is located closest to the door. Each zone has an upper and lower heating element and each zone is independently controlled.

In order to accurately and consistently move the blank to and from the furnace and press, a manually-operated transfer mechanism is used. The transfer system (developed by George [118]) and its components are shown in Figure 17.

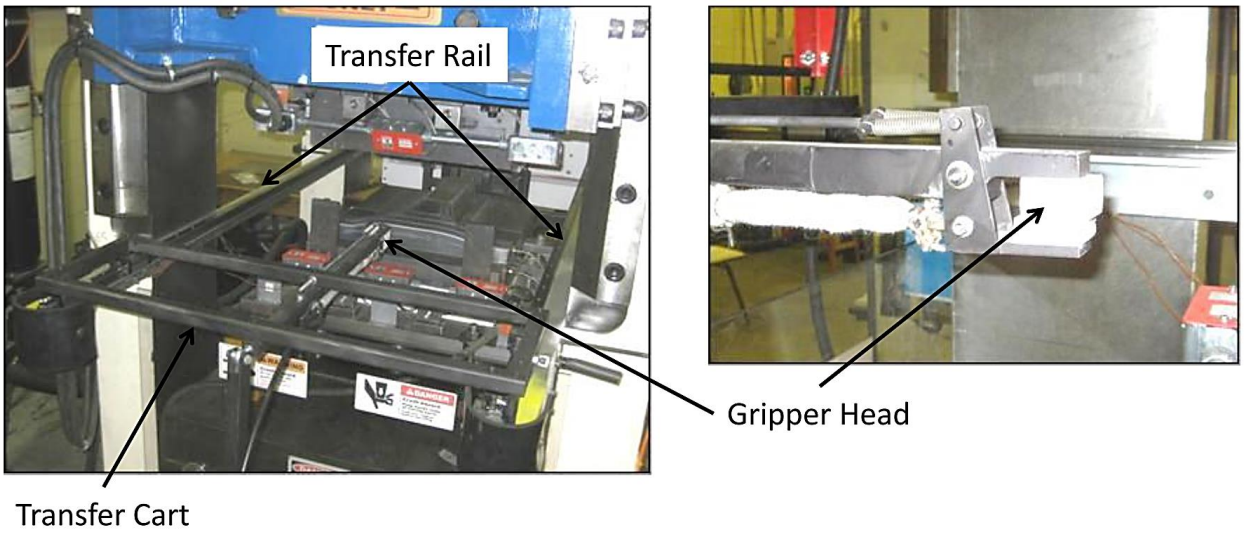

Figure 17: Transfer system [118]

The transfer system consists of a cart supporting a griping mechanism. The cart is mounted on two horizontal profile rail guides that are attached to the supporting columns of the press actuator. The transfer system allows for the gripping mechanism to move within the press bed area, towards and within the furnace. This allows the gripper head to grasp and drag the blank from within the oven onto the tooling which sits on the press bed. The grip is insulated and pulls the blank by the tab located at the end of blank to minimize heat loss. The transfer mechanism's movement requires the user to manually move it along the rails with

an extended handle mounted on the cart. The gripper is operated by a manual push-pull cable system attached to the handle.

The tooling was designed by Omer [119] and consists of the die, binder and punch. The tooling for die quenching was designed to incorporate cooling channels throughout the length of the binder and die. To maximize tool life and forming consistency, all components are hardened. The tooling components can be seen in Figure 18.

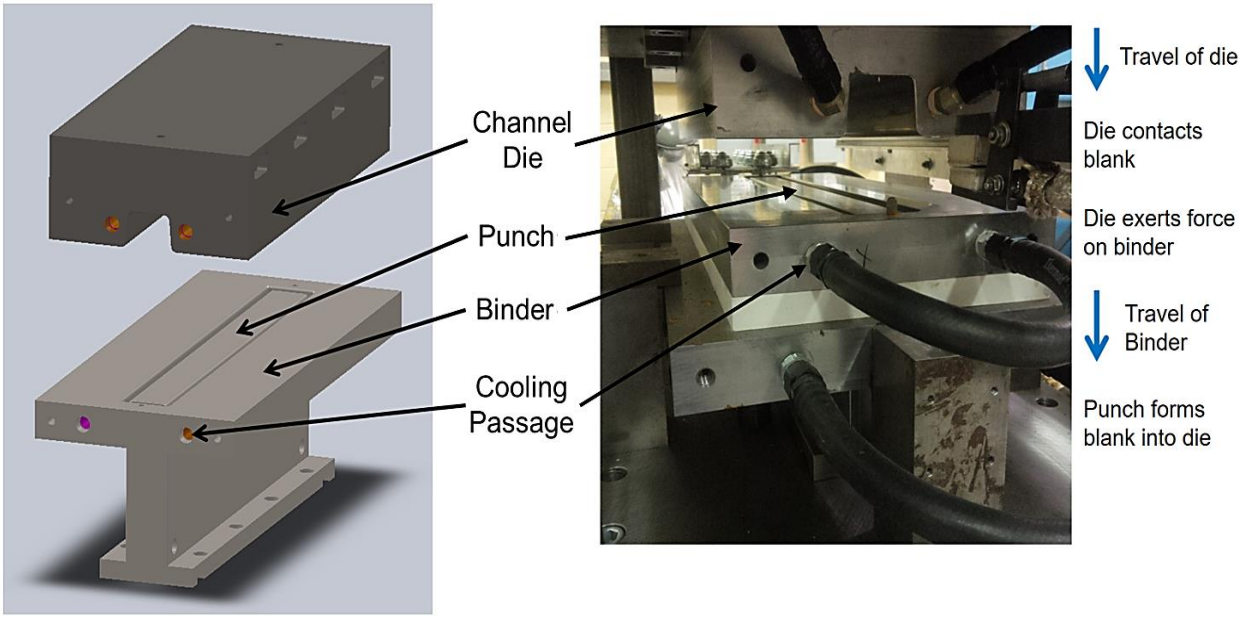

Figure 18: Forming tooling components and cooling channels

The cooling channels limit the temperature of the die and maximize the quench rate during forming. The die is attached to the ram of the hydraulic press. The punch is attached to the base of the die platform and is stationary during forming. Four nitrogen springs are mounted to the die platform and can be seen in Figure 19.

Figure 19: Nitrogen springs mounted on the die platform

The nitrogen springs are pressurized to 11.2 MPa, creating 12.25 kN of force at the start of the tooling stroke, increasing to 15 MPa and 16 kN of force by the end of the stroke. The binder rests on the nitrogen springs which ensure proper normal force on the blank and die throughout forming. During forming, the blank rests upon the binder. When the die moves downwards, it comes into contact with the blank and pushes the binder down (Figure 20) with the nitrogen springs creating the normal force on the binder. As the die begins to move the blank and binder downwards, the punch protrudes through the binder opening, contacting the blank and forming of the blank begins. The part is fully formed once the die reaches the end of the stroke.

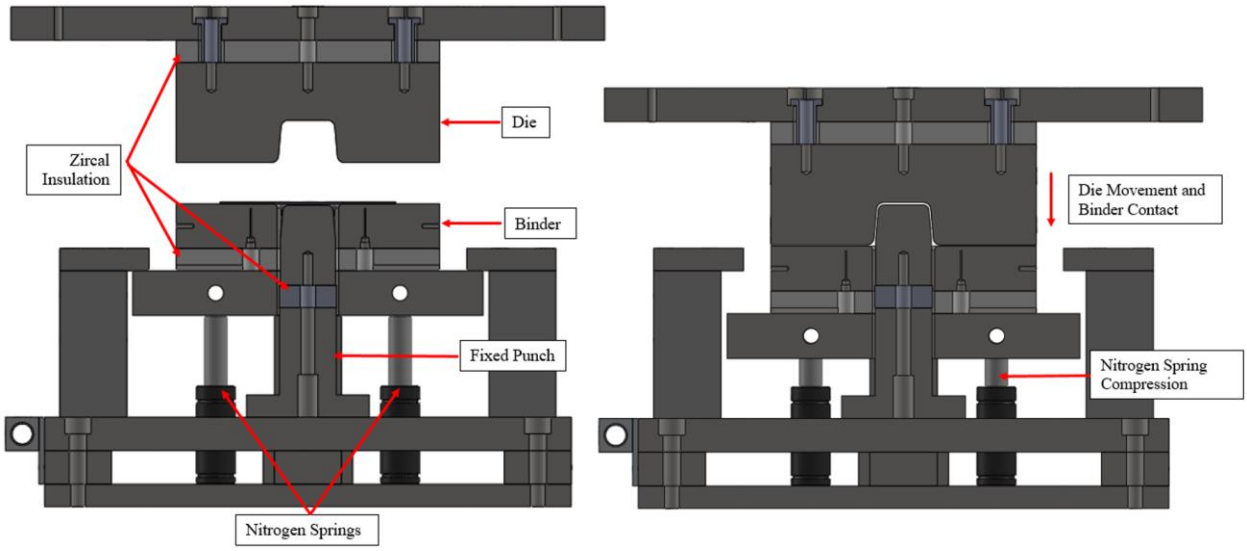

Figure 20: Cross-sectional view of the tooling movement during the forming process

The specific procedure followed for the die quenching process is as follows:

1. The blank was placed in an oven at the solutionization temperature of 470°C and held for the appropriate time of 8 minutes.
2. The blank was then transferred into the die set using the manual transfer system, and aligned using the locating pins on the tooling
3. The blank is then formed within the chilled tooling and held for 10 seconds at a force of 890 kN
4. The formed beam is manually transferred out of the tooling and cooled at room temperature

2.2.1 Die Quenching Forming Parameters

The experiments considering the die quenching process were limited to the 7000-series alloys. Due to the high energy consumption and cost of the die quenching process, it is more attractive for use with higher strength 7000-series alloys. In addition, it was found that in initial die quench studies with AA6013, the

higher solutionization temperature of 538°C [31] caused significant thermal softening of the blank. As a result, the binder pressure and coefficient of friction between the tooling and blank was too high and the channel began to undergo diffuse necking at the radius where the top of the beam meets the sidewall and eventually failed. In contrast, the solutionization temperature of the 7000-series alloys is in the range 470-480 °C at which temperature the 7000-series alloys exhibit reasonable handling and forming characteristics.

The solutionization temperature of 470 °C for the 7000 series alloys is widely reported in the published literature [120], [121]. Unfortunately the soak time is often drastically over-estimated and a soak time of 30 minutes is often used [63], [122]. A soak time of 30 minutes is far too long to allow this process to be used in a high-volume production process, and thus a study on solutionization time is required. Omer et al. [123], [124], did studies on minimum solutionization time required for AA7075 and AA7xxx. It was concluded that the minimum required time for solutionization was 8 minutes.

The effect of the transfer time from the solutionization furnace to the tooling (and in-die quenching process) was also studied by Omer *et al.* [124] to determine the maximum transfer time before ductility and strength is significantly affected. They found that for AA7075, the tensile ductility dropped approximately 10% for a transfer time of 15 seconds whereas no degradation in ductility was observed for a transfer time of 6 seconds. The developmental AA7xxx alloy had no change in ductility and UTS when transferred in 15 seconds. To be conservative, for forming of the AA7075 alloy, a transfer time of 6 seconds (or less) was chosen.

As mentioned, quench rate is very important in the die quenching process since it dictates whether or not the material reaches a SSSS. Omer *et al.* [124]

conducted quench rate sensitivity tests on AA7075 and the developmental AA7xxx alloy, varying the quench rate through die contact pressure. Five different quench rates were observed and it was found that the minimum quench rate for AA7075 was 40°C/s and that the developmental AA7xxx alloy was insensitive to quench rate. In the current work, the contact force during quenching (press force of 60 Tons) was found to provide a quench rate of 40°C/s and was deemed acceptable.

2.2.2 Die Quench Lubricant Selection

Due to the low hardness of the material at the solutionizing temperature, galling and surface scoring can occur with pick-up of the aluminum material accumulating on the tooling surface due to friction. This results in poor surface quality as can be seen on the sheet surface in Figure 21 a). Current warm forming lubricants such as Fuchs Forge Ease AL278 are not intended to be used at the solutionizing temperature of AA7075 and burn as a result after insertion within the furnace (note that application of the Fuchs lubricant directly to the tool instead of the blanks was not considered). In addition, the residual pick-up of material on the tooling made forming conditions worse for subsequent parts.

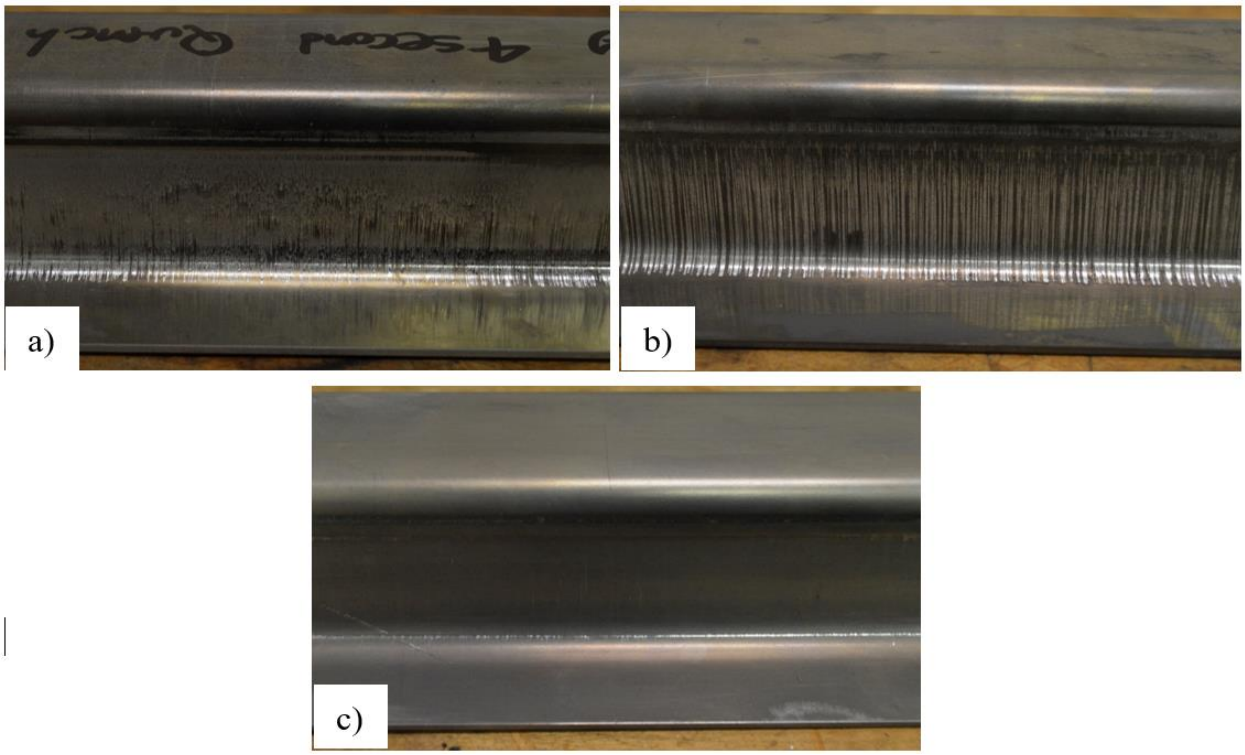

Figure 21: Surface quality for forming with a) no lubricant, b) OKS and c) PTFE Spray

Two different alternative lubricants were tested, OKS 546 lubricant and a LPS dry film PTFE spray lubricant. The OKS lubricant comprises a graphite particle suspended in water with an organic binder and was applied onto the test blank with a brush, while the PTFE was applied with an atomizer spray. The lubricants were applied on the blanks prior to solutionizing, as well as to the tooling prior to forming. Neither lubricant burned at the solutionizing temperature. The surfaces of the formed part with both lubricants are shown in Figure 21 b) and c). Although the graphite lubricant did improve the surface quality compared to the part without lubricant, it did not eliminate scoring/galling and tooling pick-up. The PTFE lubricant allowed for the best surface quality for which no visible scratches

were present. As a result, all subsequent forming operations used the PTFE lubricant for the blank and tooling.

2.2.3 Post-Forming Heat Treatment

As a baseline, it was chosen to heat treat some of the as-die quenched channels back to their as received temper. For these channels, the conventional T6 and T76 heat treatment schedules for both 7000-series alloys, shown in Table 6 were applied after die quenching.

Table 6: Heat treatment schedule for AA7075-T6 [68] and the developmental AA7xxx-T76 [116] alloy

	AA7075-T6		AA7xxx-T76	
	Temperature	**Time**	**Temperature**	**Time**
Heat treatment	121°C	24 hours	120°C then 163°C	5 hours 15 hours

Additional final tempers were chosen for the die quenching process that coincide with tempers achieved using an experimental heat treatment schedule developed by Omer *et al.* [124] who considered the same materials used in this thesis. The materials were solutionized and then subjected to a heat treatment schedule which leveraged the paint bake cycle to accelerate the time it would take to reach either a peak age (T6) condition for the AA7075 alloy or an over aged condition for the developmental AA7xxx alloy. Omer *et al.* [124] considered a two-step heat treatment process; the first heat treatment is at the same or similar temperature to what is prescribed in the literature (and in Table 6) for the target

material temper, but for a shorter period. This first aging stage serves to nucleate fine precipitates within the material matrix before undergoing the second heat treatment step, the paint bake cycle during which the material will achieve its final strength. The experimental heat treatment schedule results in a temper which is denoted by the IPB (Interrupted Paint Bake) designation after the emulated temper designation. The experimental heat treatment schedules can be seen in Table 7.

Table 7: IPB heat treatment schedules for AA7075 and AA7xxx [124]

	AA7075-T6IPB		AA7xxx-T76IPB	
	Temperature	**Time**	**Temperature**	**Time**
Initial heat treatment	121°C	8 hours	100°C	4 hours
Paint bake cycle	177°C	30 minutes	177°C	30 minutes

The post forming heat treatment schedules are shown in Figure 22.

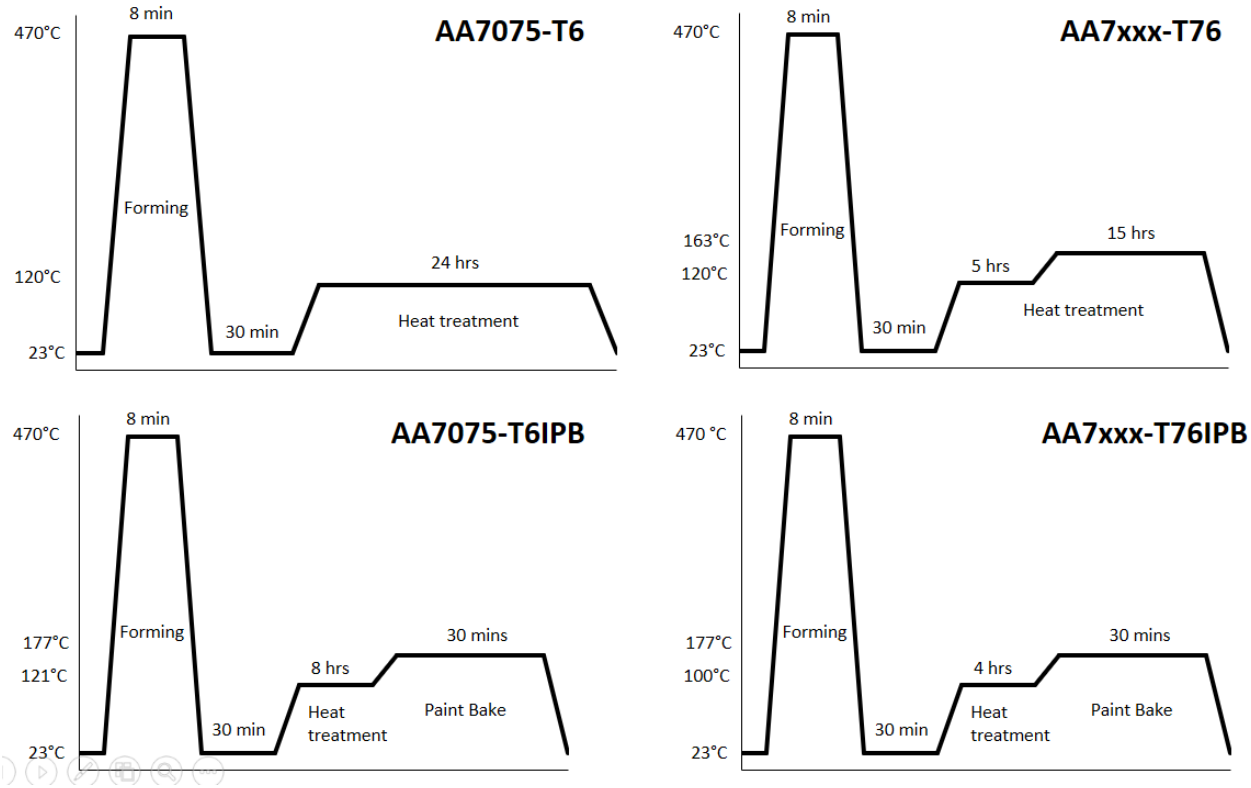

Figure 22: Visual representation of the post die quenching heat treatment schedules

2.2.4 Microhardness Measurements of Die Quenched Parts

The Vickers Hardness (HV) of all three alloys in the as-received conditions, was measured to serve as a baseline for the various die quenching and subsequent aging process routes. The peak hardness can be correlated to the ultimate tensile strength of aluminum alloys [125] and as a result it is indicative of the temper.

To assess the temper of the as-formed channels, micro hardness samples were taken from the top section, sidewall and flange of the channels. The beam was sectioned along the length into 25 mm strips using a horizontal bandsaw with a strong coolant flow. These sections were then cut into specimens under 20 mm x 15 mm in dimension using a Struers Accutom-50 wet saw. These specimens were placed into a binder clip and mounted into metallurgical pucks that were made

with a mixture of epoxy and low exothermic epoxy hardener shown in Figure 23. Once hardened, the pucks were polished using grit SiC paper in the following order: 220/320, 500, 800, 1200, 2400 and 4000.

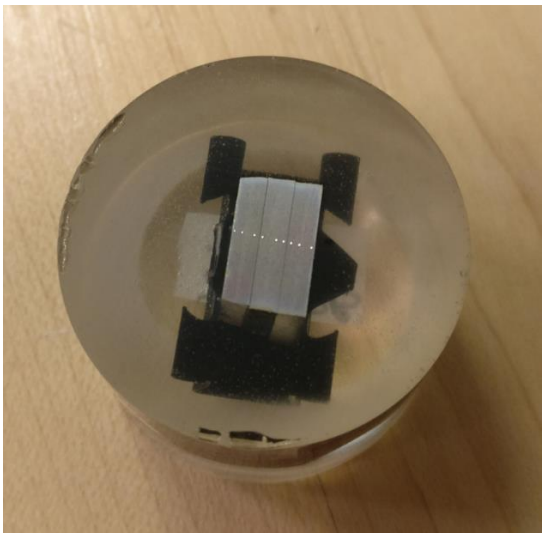

Figure 23: Epoxy resin puck with specimens mounted for micro-hardness measurements

The pyramidal indentations for the hardness measurements were done using a LECO MHT series 200 hardness tester with 1000g of force. To view the indentations for measurements, a MicroPublisher 5.0 RTV microscope was used and ImagePro 5.1 software was used to measure the diagonals of the indentations. From the diagonal measurements, the Vickers hardness was calculated.

2.3 Warm Forming Experiments

The warm forming operation was performed on another Macrodyne press, in this case with a 900 Ton capacity, shown in Figure 24. This press consists of a main 600 Ton cylindrical actuator and four smaller 75 Ton binder actuators. This press is comparable to a press in a production facility and therefore capable of exerting 600 tons of force with the main cylinder and 300 tons of binder force. The

main cylinder also has a pair of “fast approach kicker cylinders” offering 60 Tons of force. For the current work, the fast approach cylinders were sufficient and the main 600 Ton actuator was disabled. Measurement of the main cylinder force also used pressure transducers placed at the inlet and outlet of the cylinder.

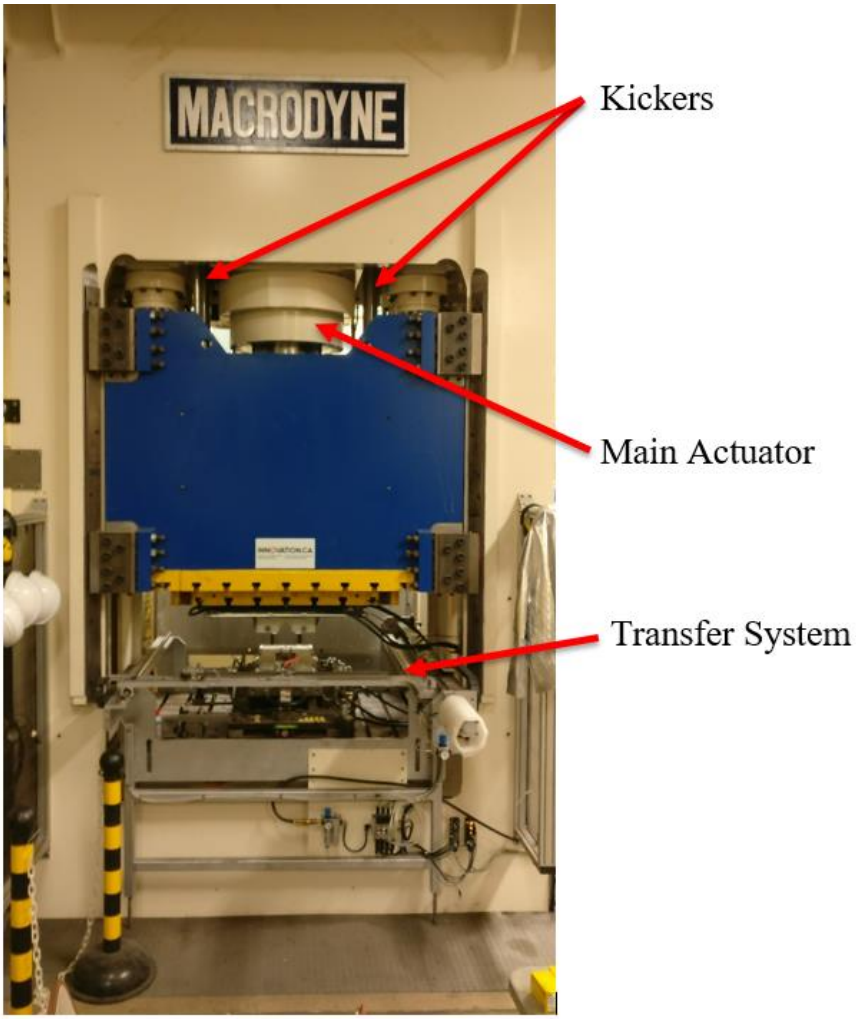

Figure 24: 900 ton Macrodyne press and its components

To heat the blanks, an oven was placed behind the press. The oven has a heating capacity of 60 kW and has 18 heating elements, 9 on the top and 9 on the bottom. The internal width, height, and length of the oven is 1575mm x 152 mm x 1219 mm. The heaters are equally spaced along the length and width of the furnace to ensure uniform heating. The furnace is separated into three regions

along its length, front, middle and back, with the front located closest to the press. Each zone is independently controlled. The oven has two doors, one at the front zone and one at the back zone. An automatic pneumatic tray system is installed inside the oven and could move to and from both front and back doors. This allows for the user to place the blank on the tray and be a safe distance from the oven. Once the heating cycle is completed the front door will open and the tray will move to the front. The oven orientation and tray system can be seen in Figure 25.

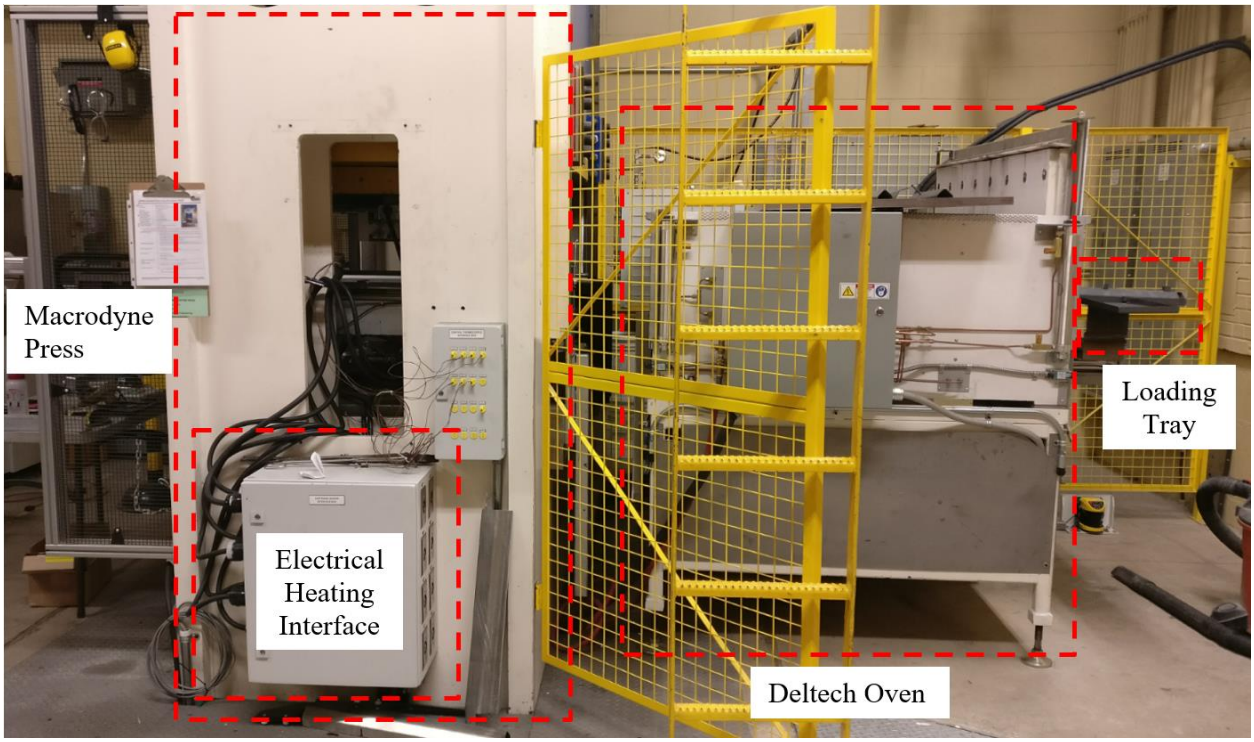

Figure 25: Oven placement with respect to the press and oven tray system

To move the blanks to and from the oven, an automated pneumatic-powered transfer system is integrated within the press system as shown in Figure 26. The system consisted of a transfer rail that moved on round linear bearing rails. The transfer rail had adjustable pneumatic grips which reached the tray within the oven and transferred the blank from the oven to the press. The grips are insulated and only contact the blank at the end tab to minimize heat loss.

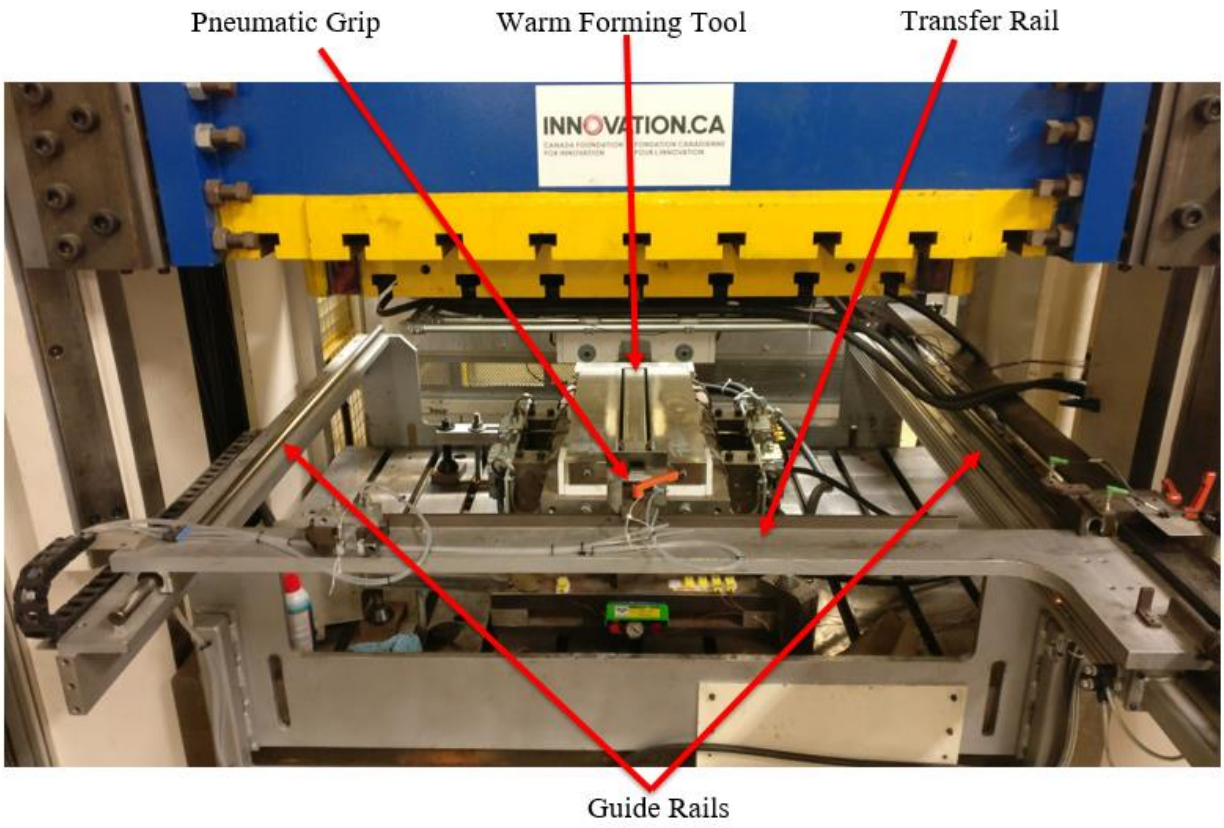

Figure 26: Press and transfer system setup for warm forming

The tooling was designed by DiCecco [126] and consists of the die, binder and punch, as can be seen in Figure 27. The tooling for warm forming was designed to incorporate heating elements and thermocouples throughout the length of the punch, binder and die. A total of 56 cartridge resistance heating elements and 5 thermocouples were used in the tooling. Cooling channels were placed along the length of the binder mounting plate, which is in-between the nitrogen springs and thermal insulation just below the binder. Thermal insulation was placed between the heating cartridges in the tip of the punch and the lower bolster plate. Lastly, thermal insulation was placed between the die and the upper bolster plate. The cooling channels and insulation isolate the heat from the binder and prevent the nitrogen springs from heating up.

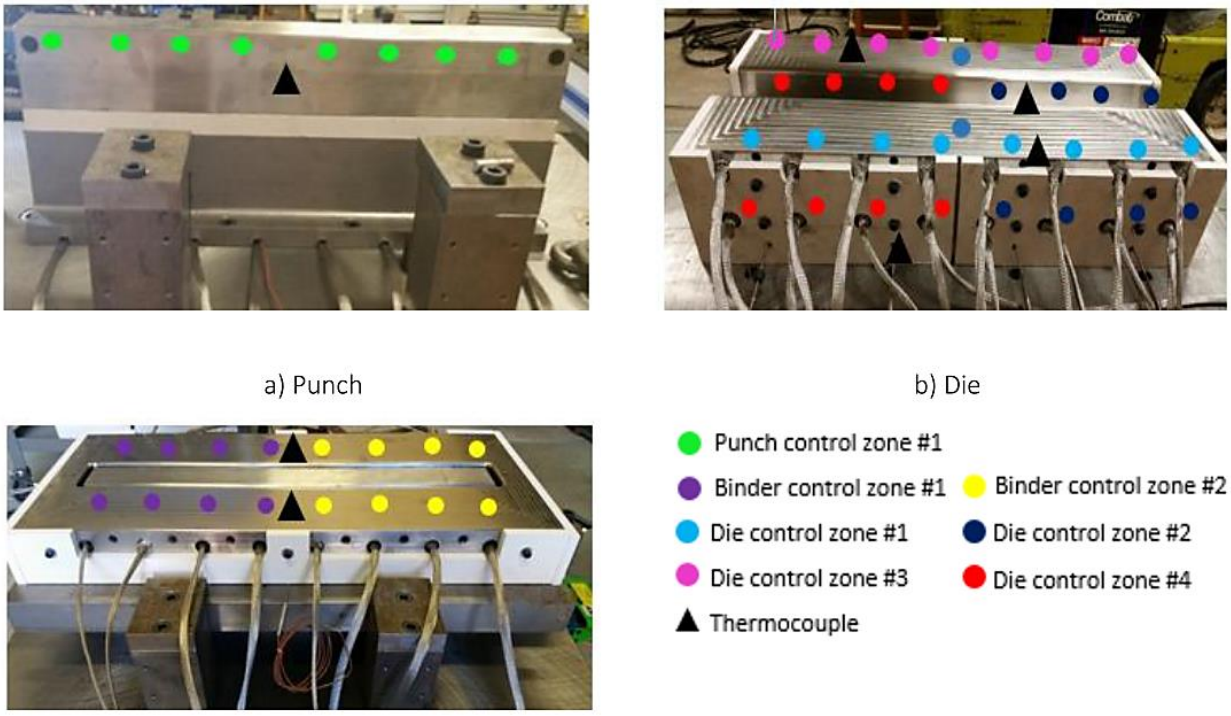

Figure 27: Heating cartridge, thermocouple and heating zone locations [127]

To maximize tool life and forming consistency, all components are made with Dievar® steel and were hardened to 55 HRC through heat treatments.

The warm forming experiments were performed using two thermal configurations: isothermal and non-isothermal. In isothermal forming, the tooling is heated to the same temperature as the blank. In non-isothermal forming, the temperature of the tooling is not the same as the temperature of the blank, in this case, the tooling was at room temperature. Both process are as follows:

1. The blank was placed in an oven at the desired warm forming temperature for 180 – 300 seconds depending on forming temperature
    a. For isothermal forming, the tooling is heated to the same temperature as the blank

b. For non-isothermal forming, the tooling is not heated and left at room temperature

2. The blank was then transferred into the tooling using the pneumatic transfer system, and aligned using the locating pins on the tooling
3. The blank is then formed and held for 3 seconds at a force of 60 tons
4. The formed beam is manually transferred out of the tooling and cooled at room temperature

2.3.1 Warm Forming Parameters

2.3.1.1 Warm Forming of As-Received T6 and T76 Tempers

Studies have been done by Noder [127] on warm forming using the same material, blank geometry, and tooling being used in this thesis. Noder used two forming routes, isothermal and non-isothermal warm forming routes. The study investigated the forming of the material at three blank temperatures, 177°C, 204°C, 233°C. The lowest temperature, 177°C was chosen because it is the temperature for most automotive paint bake cycles. The highest forming temperature, 233°C was chosen because it is the upper limit of the critical over-aging temperature for the developmental AA7xxx alloy, at which point precipitates start to coarsen, resulting in lower strength and ductility. The median temperature, 204°C was chosen because it is an intermediate between the upper and lower forming temperature in this study. The warm forming temperature parameters in this thesis replicate those of Noder [127].

2.3.1.2 Under-aged Warm Forming

Under-aged (UA) blanks were also warm formed following a process designed to reach a peak aged condition after the warm forming operation and paint bake thermal cycle. For this process, only AA6013 and AA7xxx were used.

Prior to forming, the blanks were required to be at an under-aged temper. To achieve this condition, the undeformed blanks were first solutionized and heat treated to the specified under-aged temper. The blanks were solutionized at the temperatures mentioned in Section 2.2.1 and then quenched in a set of flat dies under 60 tons clamping force. The temperature *versus* time history of the blank during the quenching process is shown in Figure 28.

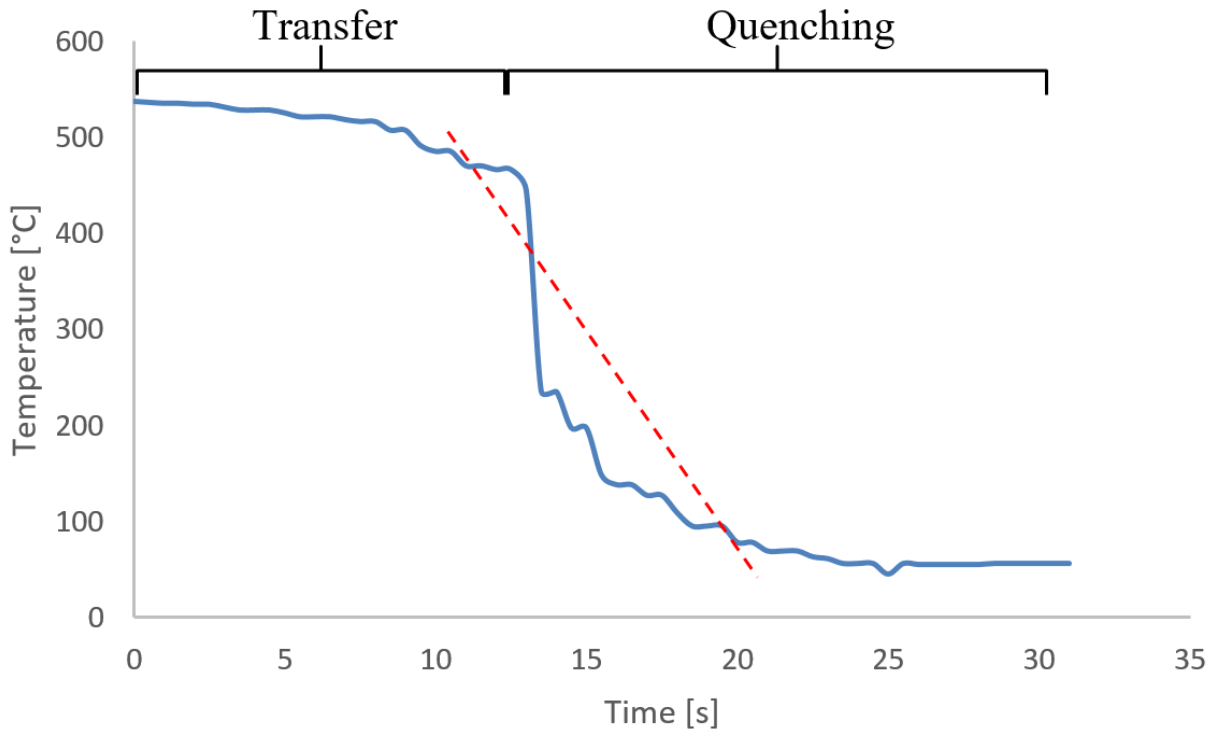

Figure 28: Measured temperature *versus* time history for AA7xxx quenched at 60 ton normal force

The quench rate of the material is estimated by the dashed red line in Figure 28. This very conservative estimation of the quench rate is 44.3°C/s which is more than 4°C/s higher than the minimum required quench rate of 40°C/s reported by Omer *et al.* [124]. The hardness of the as-solutionized and quenched blanks is 89 HV and 137 HV for AA6013 and AA7xxx, respectively, which is equivalent to the hardness reported in the literature for W temper AA6013 [31] and AA7xxx [124].

Both materials were then tempered using the schedule outlined in Table 8 to reach the desired under-aged temper.

Table 8: Under-aged heat treatment schedule for AA6013 and AA7xxx [126], [128]

Step	AA6013	AA7xxx
1	Solutionize at 560°C for 10 min	Solutionize at 470°C for 10 min
2	Quench	Quench
3	Heat treat at 100°C for 4 hours	Naturally age at room temperature for 48 hours
4	N/A	Heat treat at 100°C for 4 hours
5	N/A	Naturally age at room temperature for 2 weeks
6	Paint Bake at 177°C for 30 minutes	Paint Bake at 177°C for 30 minutes

Once heat treated to the under-aged condition, the blanks were heated to their respective warm forming temperature in the same furnace described in Section 2.3.1.1 and then isothermally formed. The channels achieve peak aged

condition after being subjected to the paint bake thermal cycle, 177 °C for 30 minutes. The forming parameters for both alloys are shown in Table 9.

Table 9: Under-aged warm forming parameters for AA6013 and AA7xxx [126], [128]

	AA6013-UA		AA7xxx-UA	
	Temperature [°C]	Time	Temperature [°C]	Time
Oven	225	5 minute soak time	177	4 minute soak time
Tooling	225	3 second dwell time	177	3 second dwell time

2.3.2 Warm Forming Lubricant

Noder [127] compared the efficacy of various warm forming lubricants. The lubricant study compared Fuchs, OKS, and PTFE spray. The study showed that the most effective lubricant in warm forming was the Fuchs lubricant which was adopted in the current warm forming experiments.

2.4 Test Matrix

The test matrix for the forming and structural testing experiments is given in Table 10. Note that quasi-static testing was performed on both warm formed and die quenched rails, whereas only the die quenching route was assessed in dynamic testing.

Table 10: Test matrix for forming and structural testing

			Quasi-static Testing	Dynamic Testing
Die Quenching	AA7075	T6	3	3
		T6IPB	3	3
	AA7xxx	T76	3	3
		T76IPB	3	3
Warm Forming	AA6013	232°C Isothermal	3	-
		204°C Isothermal	3	-
		232°C Non-isothermal	3	-
		232°C Under-aged Isothermal with paint bake cycle	3	-
		232°C Under-aged Isothermal without paint bake cycle	3	-
	AA7075	232°C Isothermal	3	-
		204°C Isothermal	3	-
		232°C Non-isothermal	3	-
	AA7xxx	232°C Isothermal	3	-
		204°C Isothermal	3	-
		232°C Non-isothermal	3	-
		232°C Under-aged Isothermal with paint bake cycle	3	-
		232°C Under-aged Isothermal without paint bake cycle	3	-

3 STRUCTURAL THREE-POINT BEND EXPERIMENTAL METHODOLOGY

The structural performance of the warm formed and die quenched rails was evaluated using quasi-static and dynamic three-point bend experiments. The peak load and absorbed energy were measured and any observable material failures (cracking or fractures) were documented. This data was also used to assess the material model through numerical simulations.

3.1 Three-Point Bend Test Specimen Preparation

After forming and thermal treatment (aging and paint bake), the channel cross-sections were “closed in” to form structural beams by integrating a backing plate which serves to improve structural rigidity during testing. The backing plate seen in Figure 15 and Figure 29, was made of the same material as the top hat section in their respective as-received tempers. The backing plate had a 25 mm gap in the middle to focus deformation within the central region of the beam and to force the channel section to transmit the entire bending load in the region of fracture. This approach serves to eliminate the influence the backplate on the onset of failure in the as-processed hat sections.

The backing plate was attached to the top hat with 5 kN Spaenaur 310-041 steel break stem rivets with a pitch of 25mm as shown in Figure 29. Detailed characterization of the rivet mechanical properties was characterized as part of this research; the full results of the mechanical testing are reported in Appendix A of this thesis. The summary of the rivet tests is shown in Table 11.

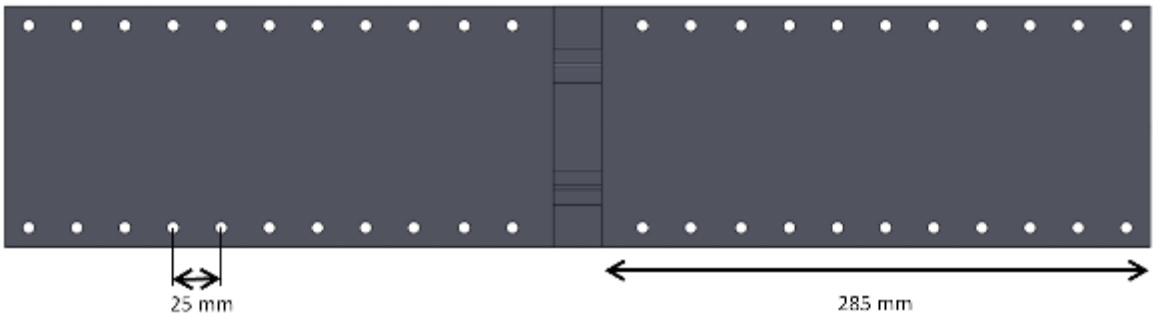

Figure 29: Backing plate dimensions and rivet pitch

Table 11: 5 kN Rivet measurements

Body Diameter	6.35 mm
Body Length	12.4 mm
Head Diameter	12.7 mm
Ultimate Shear Strength	5.5 kN
Ultimate Tensile Strength	6.7 kN

3.2 Quasi-Static Test Setup

The quasi-static three-point bend experiments were performed using an in-house hydraulic test frame, shown in Figure 30. The hydraulic actuator can exert a peak force of 496 kN and has a 480 kN load cell attached. The actuator is operated under closed-loop positional servo-control through a MTS FlexTest servo controller. A custom LabVIEW program provides the program signals via a PC-based Digital-to-Analog data acquisition (DAQ) card. Force and displacement data during testing was captured using the same DAQ card with a sample frequency of 4 Hz. The experiment was also recorded using a Nikon D3200 digital camera mounted onto a tripod.

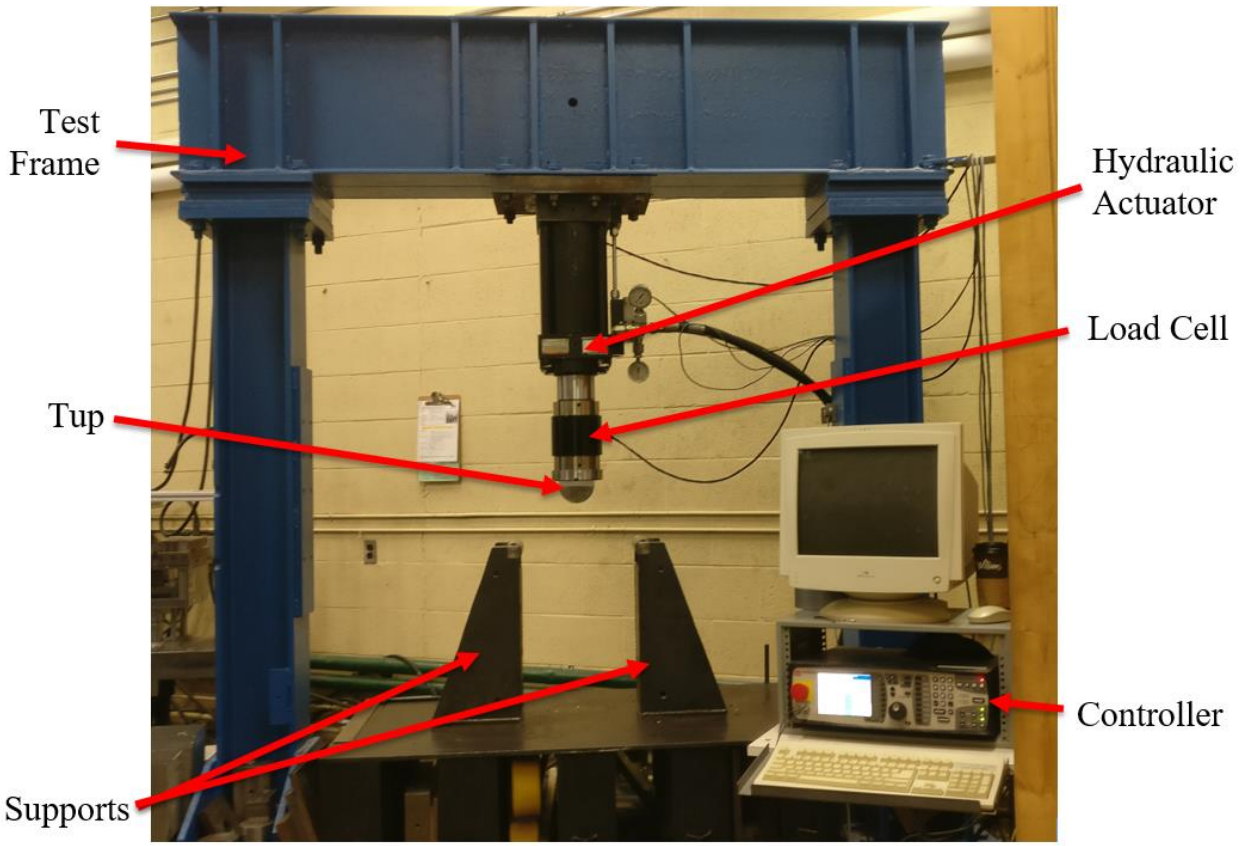

Figure 30: Quasi-static Test Frame

The quasi-static setup can be seen in Figure 31. The impact beam is supported by two removable cylindrical supports that are 50 mm in diameter and are spaced at a span of 365 mm (centre-to-centre). Each cylindrical support is 177.8 mm in diameter upon which the base of the impact beam is supported. The cylinders are mounted to two base supports with a height of 500 mm which accommodate the deformation of the impact beam.

The loading tup has a diameter of 100 mm and is carburized to prevent surface damage and limit wear. The tup is mounted onto the load cell with an adaptor plate which is attached to the hydraulic actuator. The testing rate was constant at 0.508 mm/s.

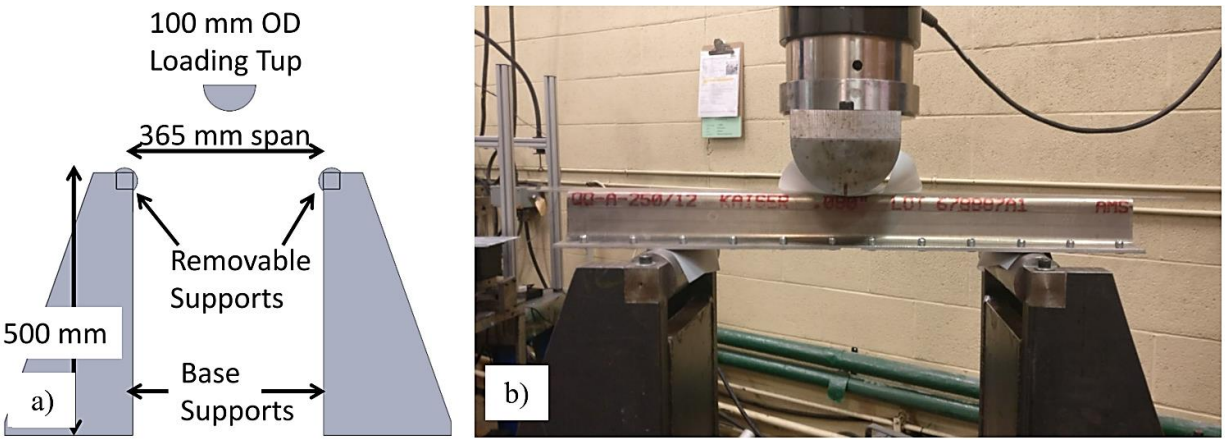

Figure 31: a) Schematic of the quasi-static three-point bend setup [129] and b)test article placement

To ensure consistent deformation between repeats, friction was minimized between the three-point bend supports and tup contacting the beam using 0.13 mm Teflon film. It has been shown that the effect of friction has a significant influence on the deformation pattern of a top hat beam undergoing three-point bending [129].

3.3 Dynamic Test Setup

The setup of the equipment for the dynamic three-point bend experiments can be seen in Figure 32 and Figure 33. The dynamic tests were performed using the University of Waterloo crash sled with the same support and tup fixtures that were used in the quasi-static experiments. The supports were mounted horizontally on the barrier wall while the tup was mounted onto the sled wall.

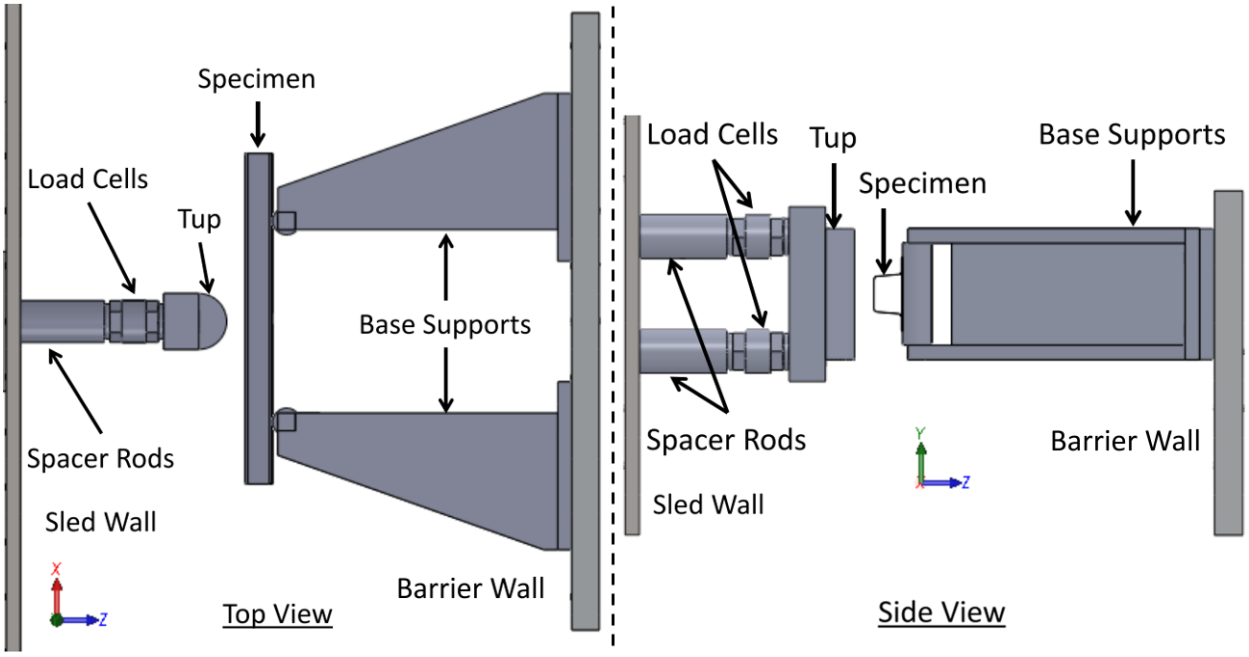

Figure 32: CAD drawing of the dynamic three-point test setup [129]

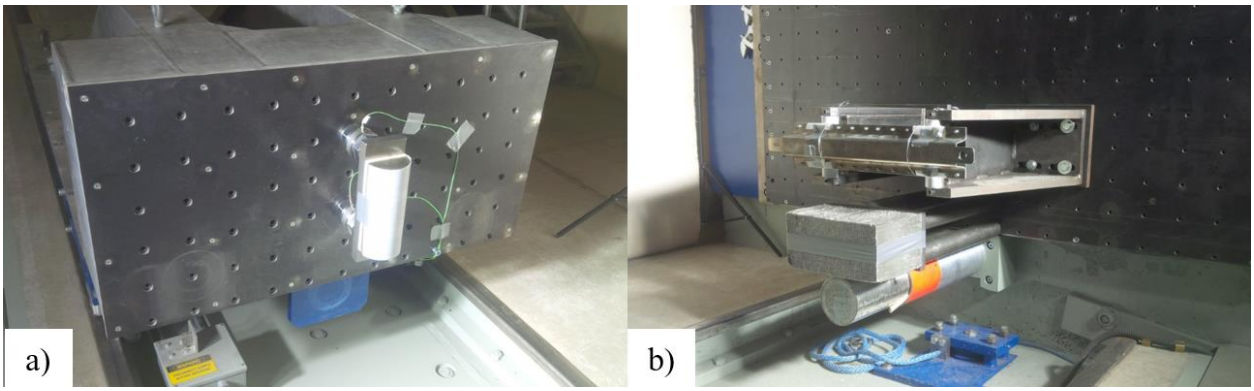

Figure 33: a) Photographs of sled and b) barrier wall assemblies

The sled wall assembly can be seen in Figure 33 a) and consisted of load cells, an adapter plate, a 0.5" plywood layer and the impacting tup. The plywood was placed between the load cells and tup to reduce the amount of high frequency ringing reaching the load cells. Two 120 kN Kistler 9731B piezoelectric load cells were placed 200 mm apart vertically and were used to measure the force exerted onto the sled by the test article.

The crash sled incorporates two accelerometers mounted on each side. The accelerometers are used to record the deceleration of the sled during impact at a sampling rate of 10,000 Hz. The accelerometer data was used to calculate displacement of the sled by double integrating the deceleration. It was also used as a secondary method to calculate impact force using Newton's second law.

The dynamic sled experiments were recorded using two high-speed Photron SA4/5 digital cameras, with a frame rate of 7500 frames per second. The cameras were mounted above and beside the test article and stills from both cameras can be seen in Figure 34.

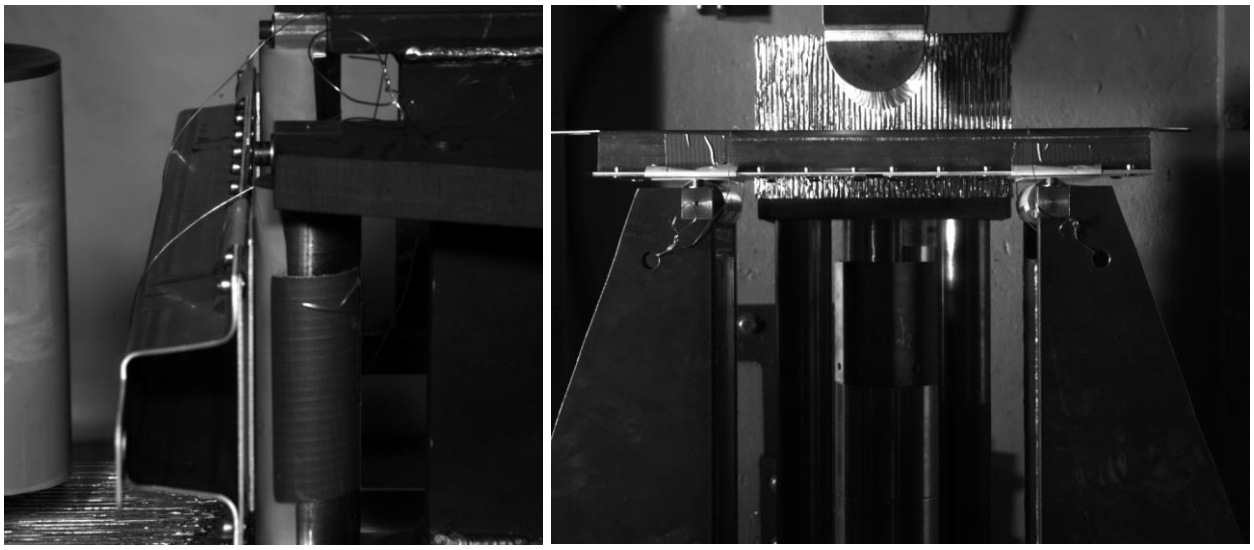

Figure 34: View from both cameras at the point of sled impact

All data acquisition system including the load cell, accelerometer, and cameras, were activated by a laser trigger that was located between the rails of the crash sled and 1880 mm from the barrier wall, seen in Figure 35. During the test, the sled trips the laser trigger and all of the imaging and data acquisition systems record for 2 seconds. The load and acceleration data was recorded using DTS Slice Micro data acquisition (DAQ) systems with a sampling rate of 10,000 Hz.

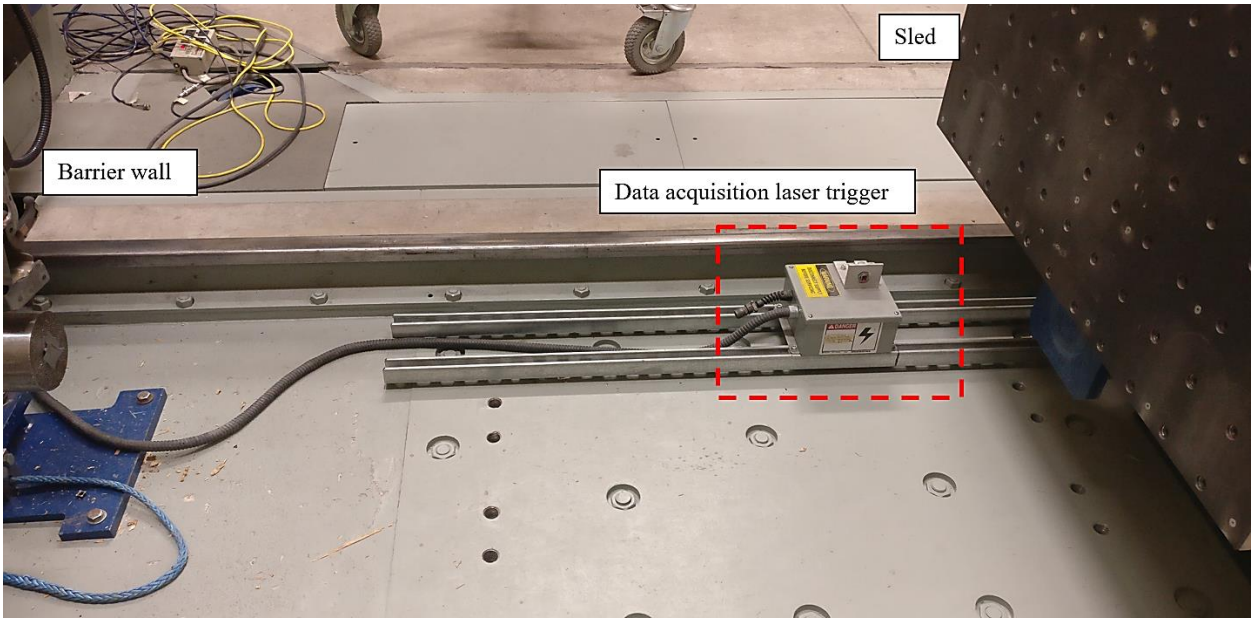

Figure 35: The data acquisition laser trigger

The surfaces on the tup and cylindrical supports are wrapped with 0.13 mm Teflon sheets to minimize friction when contacting the beam. Mounted on the barrier wall (Figure 33 b)) are Plascore 5052 aluminum honeycomb blocks located 500 mm below the centre of the test article. The honeycomb has a crush strength of 3.69 MPa [130] and was used to arrest the sled after it reached the prescribed free crush distance. The crush area of each individual honeycomb pieces measured 152 mm by 152 mm and in 200 mm length.

4 NUMERICAL MODEL OF DIE QUENCHING AND SUBSEQUENT THREE-POINT BEND RESPONSE

Numerical models of the die quenching process and three-point bending experiments were developed using the LS-DYNA commercial finite element software package. Meshing of all of the numerical models was done using Altair Hypermesh. This chapter presents the forming and three-point bending models, while the results of the simulations are presented in Section 5.4. Note that the simulation effort did not include models of the warm forming process which was undertaken in a separate Master's thesis by Noder [127].

4.1 Die Quenching Model

4.1.1 Modeling Strategy

In die quenching of aluminum, the forming process does not directly dictate the final properties of the material, assuming the quenching process was done correctly. The final properties of the material are dictated by the subsequent applied heat treatment (aging process). Currently, LS-DYNA does not offer a built-in material model that can predict mechanical property evolution during artificial aging. Therefore, in this work, the final strength of the part will not be determined from the forming model. Instead the purpose of the forming model is to assess the heat transfer between the blank and the tooling based on the predicted cooling rate and to predict the thinning of the blank during forming.

The die quench model was done in one simulation stage. Springback was not assessed since the material models that were implemented did not have a

temperature dependent elastic modulus. Furthermore, the actual degree of springback in the experiments was rather small due to the high forming temperatures and low operative material strength during forming.

A coupled thermo-mechanical solver was used to model the die quench operation. The mechanical solver calculates the stress, strain and deformation of the blank using a dynamic explicit time integration scheme, while the thermal solver calculates temperature and heat flow using an implicit time integration scheme [131]. For each time step, heat transfer between the blank and tooling was calculated and the temperature distribution determined for the next time step. The temperature-dependent mechanical properties were then assigned to model the next mechanical time step of the simulation.

4.1.2 Finite Element Mesh

Figure 36 shows the finite element mesh used to simulate the die quenching process. The blank was meshed using 2 mm fully integrated shell elements with seven through-thickness integration points used for both the mechanical and thermal solvers. The model used a quarter-symmetry assumption with appropriate symmetry boundary conditions to reduce computational cost.

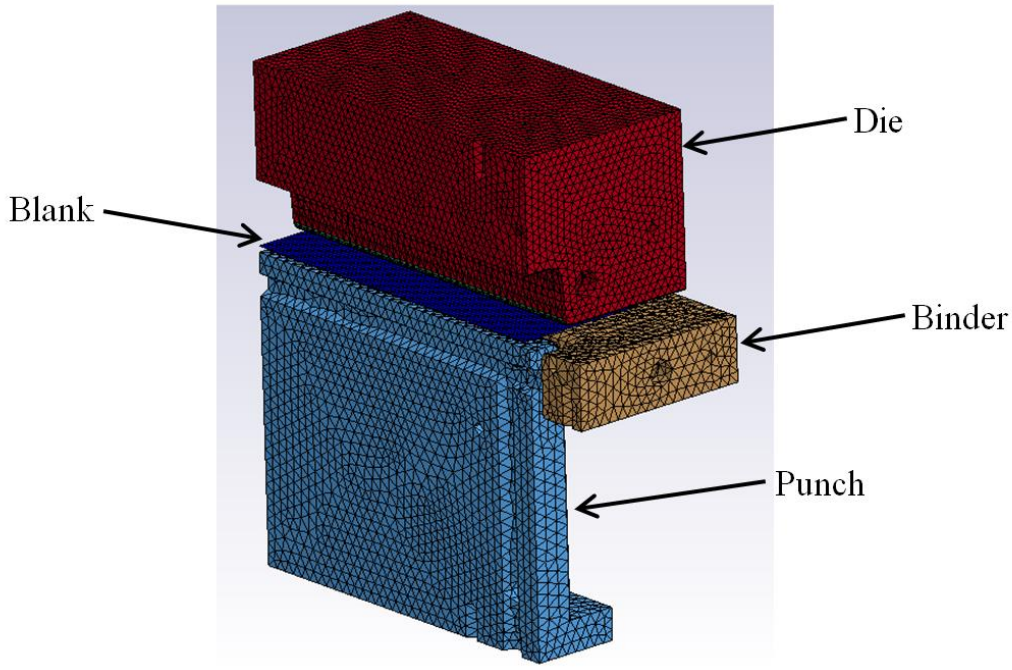

Figure 36: Tooling discretization and orientation in numerical model

The tooling was meshed using a combination of tetrahedral solid element and quadrilateral shell elements. The main volume of the tooling was discretized using 10 mm tetrahedral elements. Due to the large size of the tetrahedral elements, they were too coarse to accurately discretize the 7.95 mm radius of the tooling. Thus, 3 mm rigid shell interface elements were used to mesh the tooling surfaces that contacted the blank and capture the finer tooling features. In the mechanical simulation, the surface shell elements were treated as rigid and a penalty function-based contact treatment was prescribed to enforce the intermittent contact condition between the tooling and blank defined by the keyword *CONTACT_SURFACE_TO_SURFACE_THERMAL.

In the thermal simulation, heat transfer between the blank and tooling surface elements was modelled using a thermal interface boundary condition in which a pressure-sensitive heat transfer coefficient is specified by the user

(described in Section 4.1.5.2). This approach enables simulation of the quenching heat transfer between the blank and tooling. The thermal conductivity between the surface shell elements and interior tetrahedral elements is set to be very high to model transfer of heat from the tooling surface into the interior of the tooling. This approach allowed for the thermal mass of the tooling to be accounted for (by the tetrahedral elements) in a computationally inexpensive manner while more accurately discretizing the geometry of the tooling surfaces.

4.1.3 Material Properties for the Tooling

The adopted thermal properties for the tooling are given in Table 12. The elastic material properties corresponding to the tool steel, also listed in Table 12, are used in the contact algorithm.

Table 12: Elastic and thermal properties of tool steel [132], [133]

Property	Value
Density	7890 kg/m^3
Young's Modulus	200 GPa
Poisson's Ratio	0.3
Specific Heat	0.519 kJ/kg·K
Thermal Conductivity	37.7 W/m-k

4.1.4 Material Model for Blank

In the thermal model, the blank was modelled using an isotropic thermal material assumption with the property data shown in Table 13.

Table 13: Thermal properties of the blank [134]

Property	Value
Density	2760 kg/m^3
Specific Heat	0.84 kJ/kg·K
Thermal Conductivity	159.5 W/m-k

In the mechanical portion of the model, the blank was modelled using a Barlat-89 yield function with temperature and strain-rate dependent hardening curves[135]. Young's modulus and Poisson's ratio were taken as 71.7GPa and 0.3, respectively. The adopted hardening curves were those published by Omer [110] and are shown in Figure 37 and Figure 38. In that work, the tensile specimens were first solutionized at 470°C and then quenched to the desired temperature to replicate the effect of die quenching. The experimental curves were fit with a generalized Voce model at each temperature of the form:

$$\sigma = A + (B + C\varepsilon)(1 - e^{-D\varepsilon}) \qquad 22$$

where A, B, C and D are phenomenological parameters.

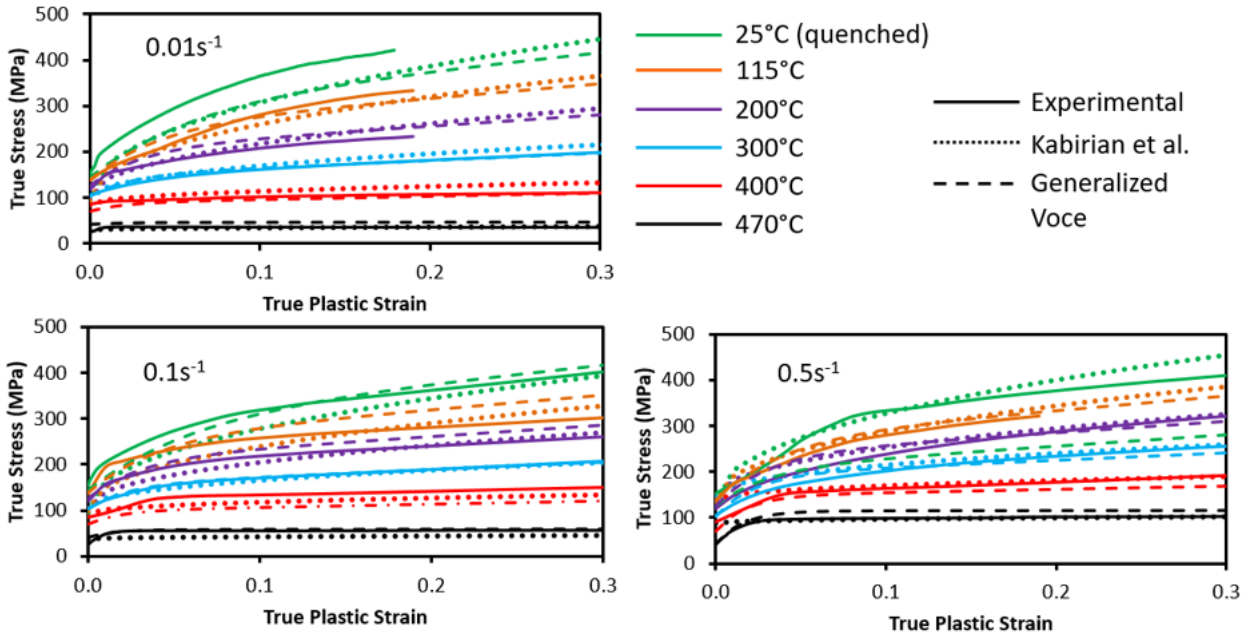

Figure 37: Temperature and strain rate-dependent hardening curves for AA7075 [110]

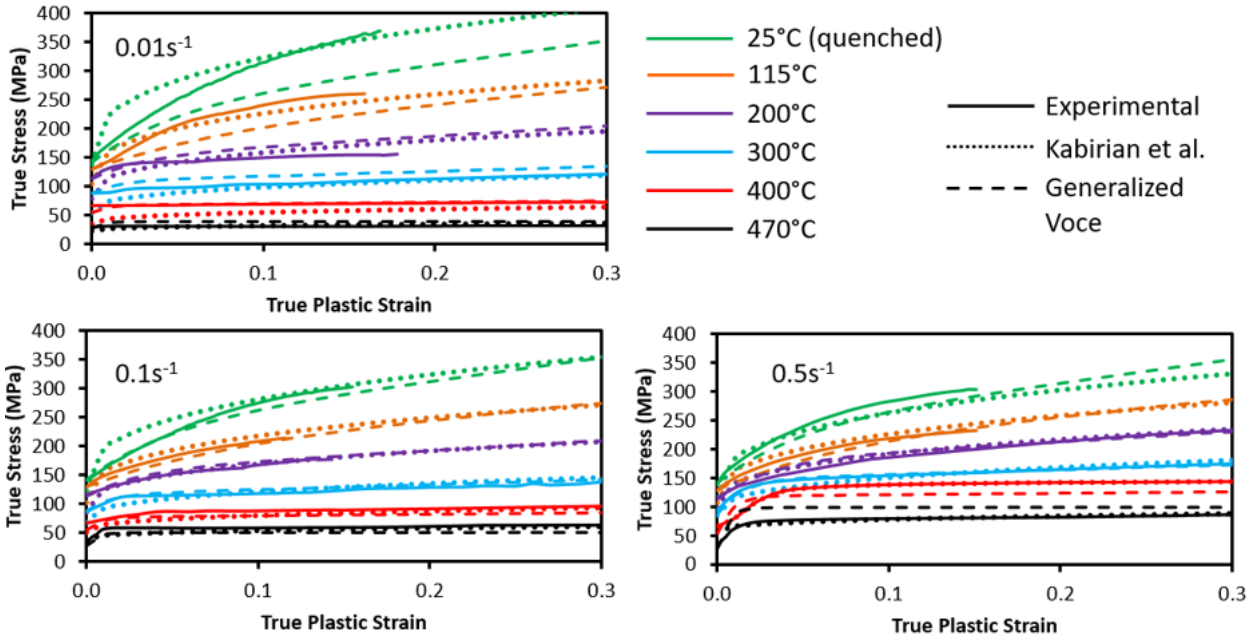

Figure 38: Temperature and strain rate-dependent hardening curves for AA7xxx [124]

The Barlat-89 yield surface [136] is defined as:

$$\phi = a|K_1 + K_2|^M + a|K_1 - K_2|^M + c|2K_2|^M = 2\sigma_y^M \quad 23$$

$$K_1 = \left(\frac{\sigma_{xx}+h\sigma_{yy}}{2}\right) \quad 24$$

$$K_2 = \left(\frac{\sigma_{xx}-h\sigma_{yy}}{2}\right)^2 + p^2\sigma_{xy}^2 \quad 25$$

where σ_y is the yield stress, M is the yield exponent and a, c, h and p are obtained from the r-values in the 0°, 45°, and 90° orientation. The parameters for the yield surface are shown in Table 14.

Table 14: r-values to define the Barlat-89 yield surface in LS-DYNA for AA7075 and the developmental AA7xxx series alloy [119]

	Temperature	RD	DD	TD
AA7075	25°C	0.67	0.93	1.07
	470°C	0.71	0.90	1.15
AA7xxx	25°C	0.55	1.21	1.83
	470°C	0.49	1.30	1.75
Yield Exponent			8	

4.1.5 Model Parameters

The forming process was 16 seconds in duration which included the blank transfer from the furnace, the blank resting on the tooling, the forming of the blank, and it being held in the tooling for 10 seconds.

4.1.5.1 Mechanical Formulation

The mechanical formulation used a dynamic explicit solver. The timestep for the explicit solver was determined by LS-DYNA using the Courant stability criterion. It states that the maximum allowable timestep can be no greater than the time it takes for a sound wave to travel the distance of the smallest element length in the model. This results in extremely small timesteps.

To increase the time step size, the density of the materials in the model are artificially increased by 100 times using so-called mass scaling. Care was taken to ensure that inertial forces did not become excessive and negatively affect the simulation accuracy. This was done by ensuring that the inertial component of total energy in the simulation remained small. The die motion was prescribed by a sinusoidal velocity curve shown in Figure 39 with an upper velocity limit of 100 mm/s. The sinusoidal curve was used to gradually accelerate and then decelerate the blank during forming to limit the inertial effects

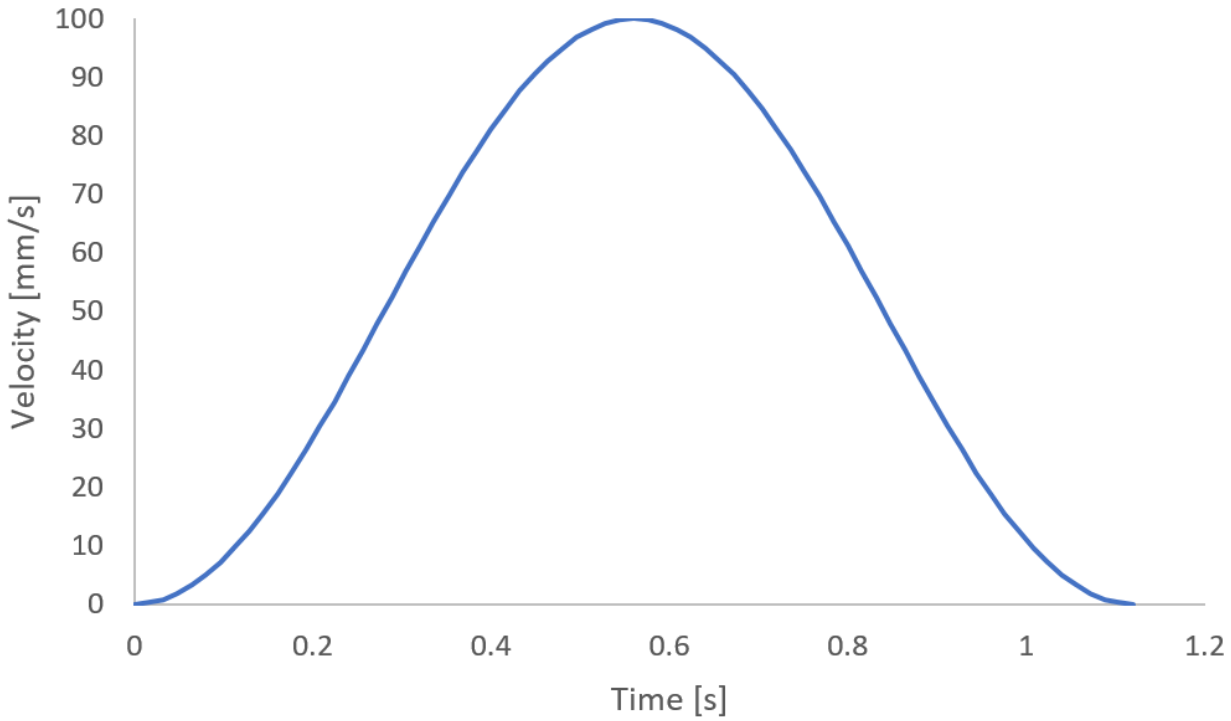

Figure 39: Sinusoidal velocity profile of the die tooling

The punch was constrained in all directions and the binder had a displacement limit of 72 mm. Since the model employs a quarter-symmetry assumption, boundary conditions on the blank were imposed on the nodes lying on the symmetry axes. Nodal translation was constrained in the direction normal to the symmetry plane and nodal rotation was constrained in the axes lying within the symmetry plane.

During forming, the heat transfer from the blank to the tooling caused an increase in the tooling temperature. To mitigate the temperature increase, the cooling passages were assigned a boundary condition temperature of 12°C to maintain the temperature of the tooling. The location of the nodes on the cooling channel surfaces can be seen in Figure 40.

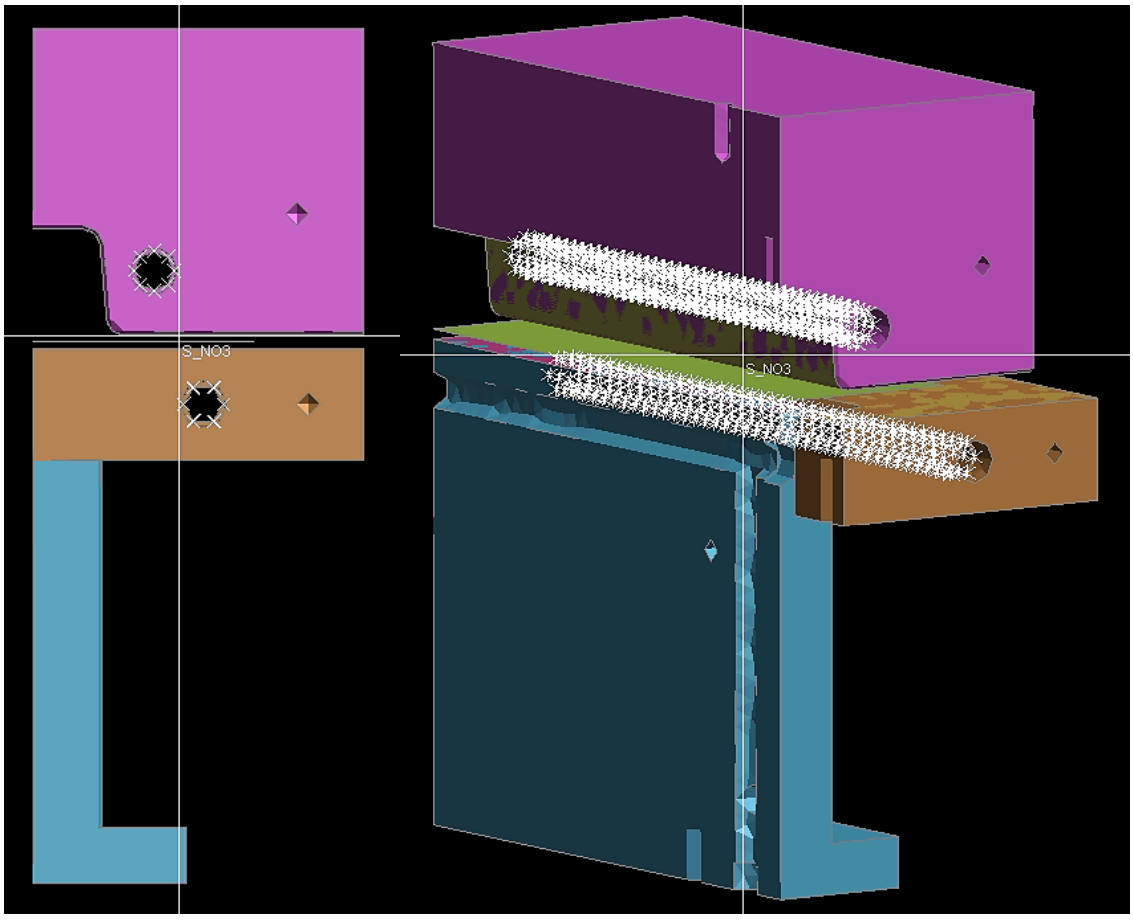

Figure 40: Cooling channel node locations

A penalty function-based surface-to-surface contact algorithm [135] was used to enforce contact between the tooling shell elements and blank. The coefficient of friction adopted in the contact treatment was 0.06 from twist compression experiments with the equivalent forming pressure.

4.1.5.2 Thermal Formulation

The thermal formulation used a symmetric direct solver with an upper limit on the time step of 0.02 seconds.

Tabulated values for the convection and radiation heat transfer coefficients were calculated for the blank at various temperatures. These coefficients were

combined to create an “effective” convective heat transfer coefficient. This approach was adopted to linearize the radiative heat transfer portion of the thermal calculation and decrease the computational time [137].

The coefficients were found using the following equations [138]:

$$h_{conv\,top} = [0.14(Gr * Pr)^{0.33}]\frac{k}{L} \quad (26)$$

$$h_{conv\,bot} = [0.27(Gr * Pr)^{0.25}]\frac{k}{L} \quad (27)$$

$$h_{rad} = \frac{\sigma\varepsilon\left(T_1^4 - T_2^4\right)}{(T_1 - T_2)} \quad (28)$$

The resulting calculated heat transfer coefficients are tabulated in Table 15. These convective and radiative boundary conditions were applied to the blank to simulate cooling after exiting the furnace prior to forming.

Table 15: Convection, radiation, and effective heat transfer coefficients

Temp [°C]	$h_{conv\ top}$ [W/m²°K]	$h_{conv\ bottom}$ [W/m²°K]	h_{rad} [W/m²°K]	h_{eff} [W/m²°K]
50	12.6	12.3	6.2	31.0
75	15.9	14.6	7.0	37.4
100	18.1	16.1	7.8	42.1
125	19.9	17.3	8.8	46.1
150	21.5	18.3	9.9	49.7
175	22.8	19.2	11.1	53.0
200	24.0	19.9	12.4	56.3
225	25.1	20.6	13.8	59.4
250	26.0	21.2	15.3	62.5
275	27.0	21.8	16.9	65.6
300	27.8	22.3	18.6	68.8
325	28.6	22.8	20.5	72.0
350	29.4	23.3	22.5	75.2
375	30.1	23.7	24.7	78.5
400	30.8	24.1	27.0	81.9
425	31.5	24.5	29.4	85.4
450	32.1	24.9	32.0	89.0
470	32.6	25.2	34.2	92.0

The blank was prescribed an initial temperature of 470°C and the tooling had an initial temperature of 12°C which corresponds to the temperature of the chilled water used to cool the tooling. The contact heat transfer coefficients between the blank and tooling were measured by Omer [119] and given in Table 16.

Table 16: Contact heat transfer coefficient *vs* applied pressure [124]

Pressure (MPa)	HTC (W/m^2K)
2	355
5	501
12.5	620
25	750
40	1010
60	2800
0 – *Convection in Air*	20.5

4.2 Three-Point Bend Simulations

Numerical models of the quasi-static and dynamic three-point bend experiments were developed and executed using the explicit dynamic finite element code LS-DYNA. The three-point bend models used the deformed mesh from the die quenching simulations to which the backer plate and rivet elements were added to mimic the experiments in Section 3.1. The following sections detail the three-point bend models.

4.2.1 Material Constitutive Model and Failure Criteria

The material model used for the beam was the Barlat YLD2000 [87] constitutive model which requires eight coefficients and used strain rate-dependent hardening curves. Room temperature material properties due to Rahmaan [139] corresponding to the as-received temper conditions of the sheet materials were assigned to the beam and backer plate. The hardening curves were

defined at eleven different strain rates, 0.001 s^{-1}, 0.01 s^{-1}, 0.1 s^{-1}, 1 s^{-1}, 10 s^{-1}, 100 s^{-1}, 1,000 s^{-1}, 5,000 s^{-1}, and 10,000 s^{-1}. The hardening curves for the as-received AA7075-T6, AA7xxx-T76 and AA6013-T6 sheet, shown in Figure 41, Figure 42 and Figure 43, respectively, were developed by Rahmaan [139]. .

Note that the properties of the AA7075-T6IPB and AA7xxx-T76IPB temper conditions were not characterized, however, the corresponding T6 and T76 properties were assumed instead. In a similar manner, the as-received AA6013-T6 properties were assigned to the three-point bending models of the as-warm formed 6013 rails. This approximation was judged reasonable and will be assessed through comparison between the predicted and measured response of the rails (Chapter 5).

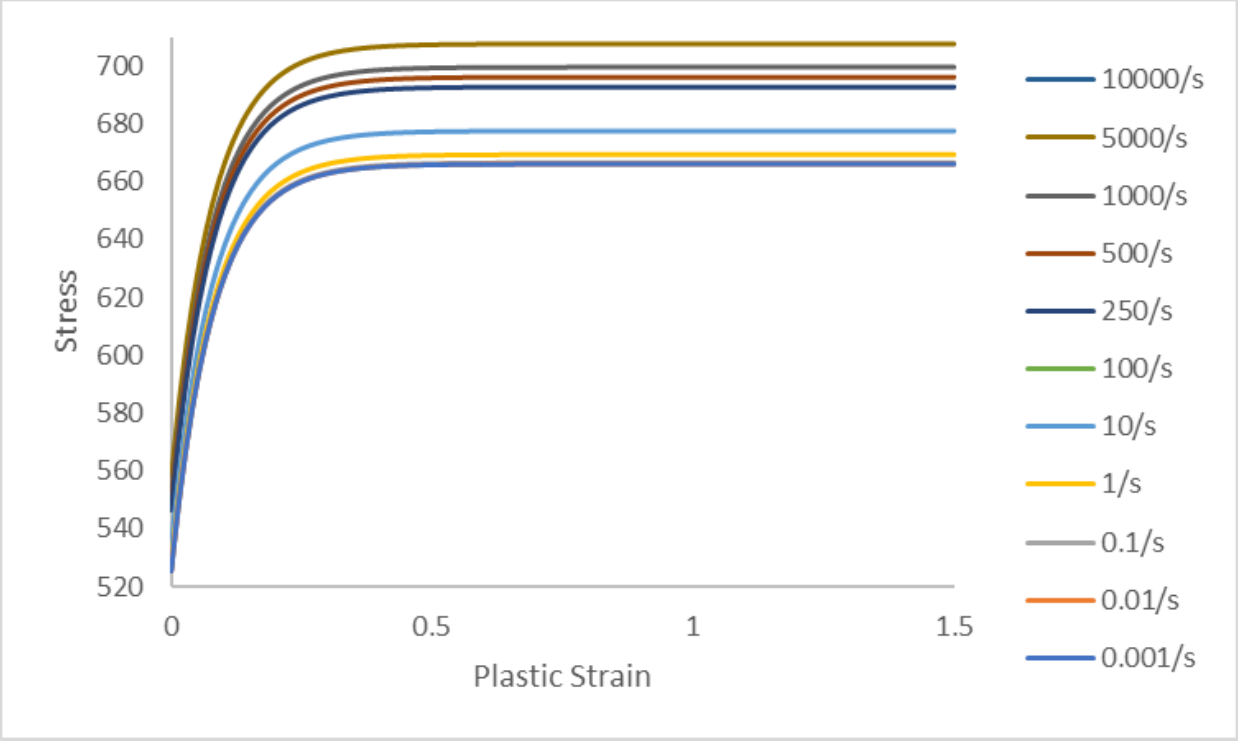

Figure 41: Hardening curves for AA7075-T6 [119]

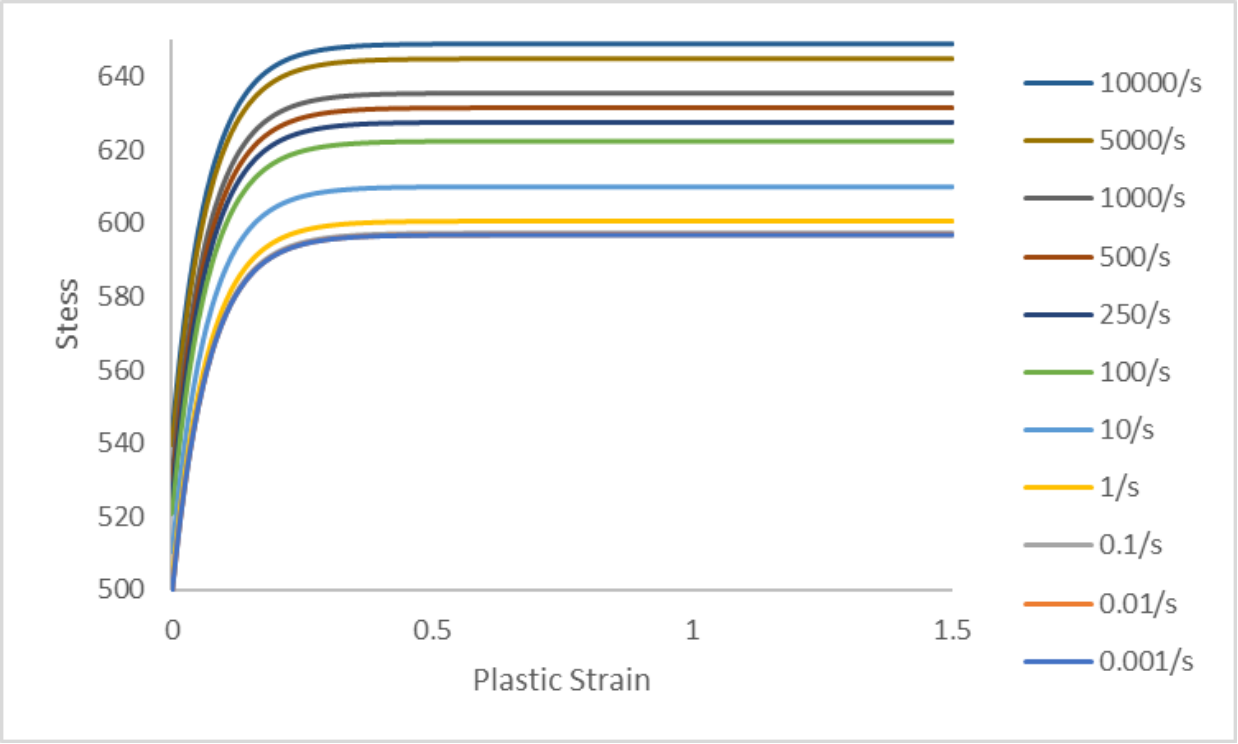

Figure 42: Hardening curves for AA7xxx-T76 [119]

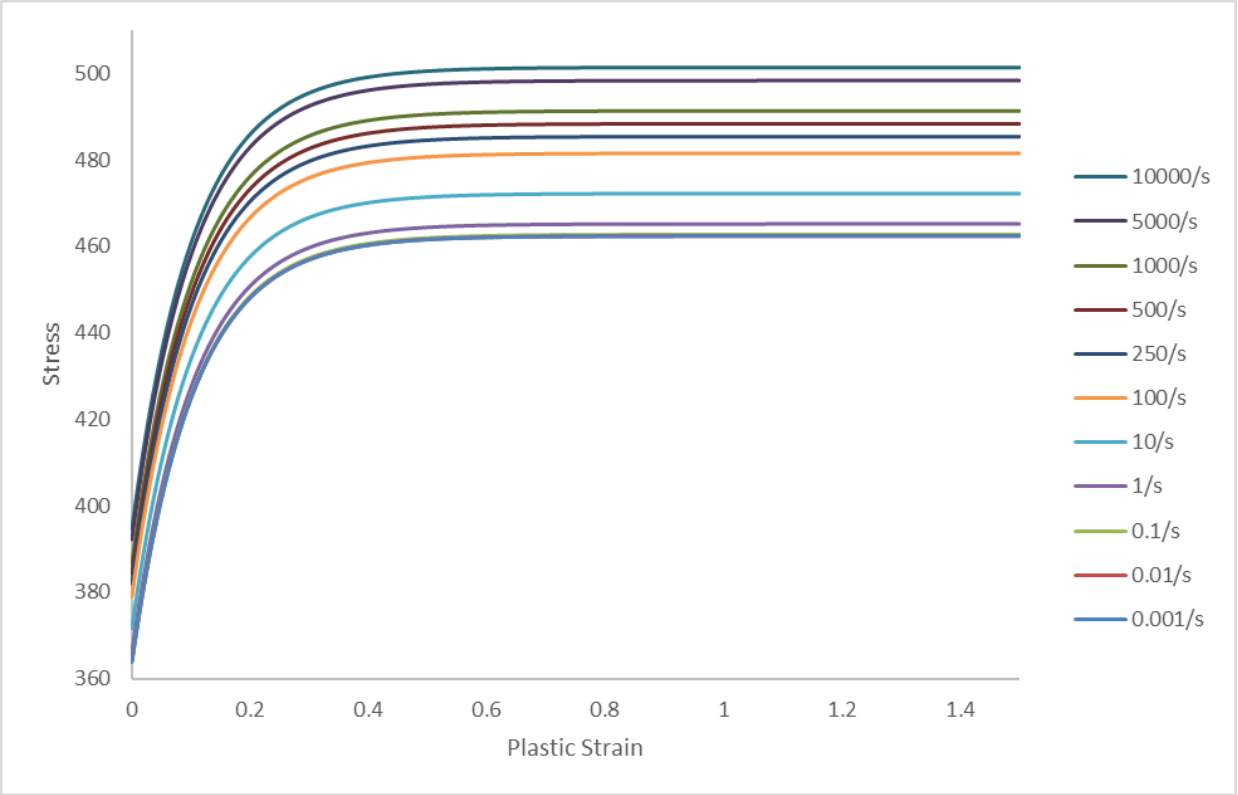

Figure 43: Hardening curves for AA6013-T6 [119]

Eight coefficients are required for the yield function parameters shown in Equation 10. The coefficients for all three materials are shown in Table 17.

Table 17: Barlat YLD2000 coefficients for all three materials [139]

Parameter	AA7075-T6	AA7xxx-T76	AA6013-T6
α_1	0.941	0.931	0.973
α_2	0.997	1.079	0.985
α_3	0.979	1.021	0.900
α_4	0.963	0.952	0.974
α_5	0.995	1.006	0.991
α_6	0.835	0.914	0.893
α_7	0.994	1.036	0.973
α_8	1.063	1.013	1.089

All three Barlat YLD2000 material models for the beam were coupled with a Generalized Incremental Stress-Strain Model (GISSMO) failure criterion [135] to predict the onset of failure during loading. The GISSMO model is defined using a *locus* of effective plastic strain at failure *versus* stress triaxiality. Failure strains were measured experimentally and fit to a Bai-Wierzbicki [103] failure criterion for all three materials subjected to various stress triaxialities by Rahmaan [139], as shown in Figure 44.

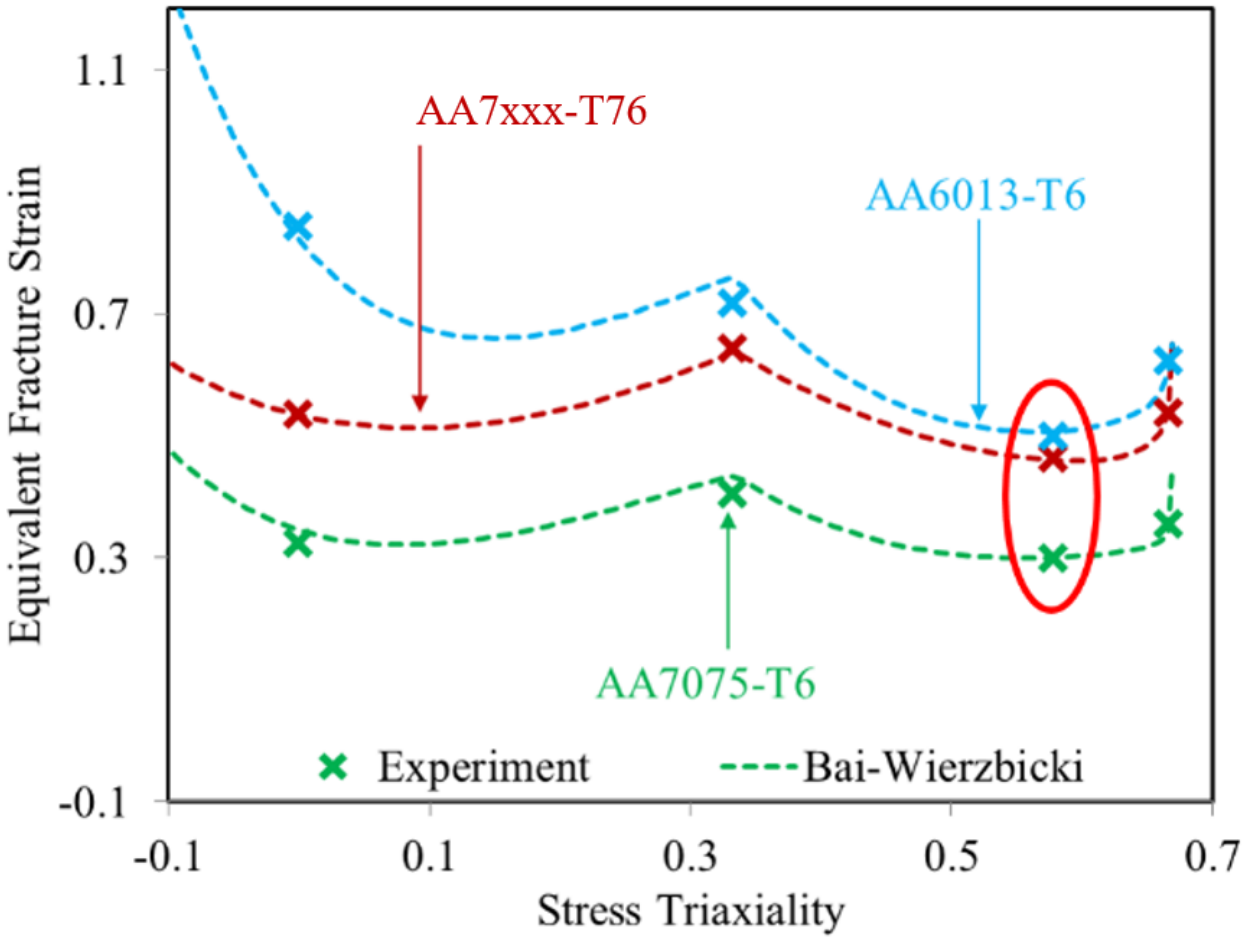

Figure 44: Loci of failure strain *versus* stress triaxiality due to Rahmaan [139]. In this case, v-bend specimens were used to acquire the failure strains in the plane strain regime (triaxiality = 0.577).

In order to account for mesh size dependency of the failure strain, a so-called regularization curves were developed by Rahmaan [139]. Since a larger element accumulates less strain compared to a smaller element for a given strain gradient, the failure strain needs to be scaled to account for this size effect. The regularization curve was applied in conjunction with the GISMMO model which scales the effective failure strain depending on the element size. This approach is further explained by ten Kortenaar [99]. Two regularization curves, denoted EB and PS, were fit for all three materials and are shown in Figure 45 to Figure 47. The EB curve is based on a regularization correction developed using equi-biaxial

Nakazima specimens, while the PS curve provides a correction developed using plane strain Nakazima specimens. Further explanation and reasoning for the two regularization curve is explain by Rahamaan [140].

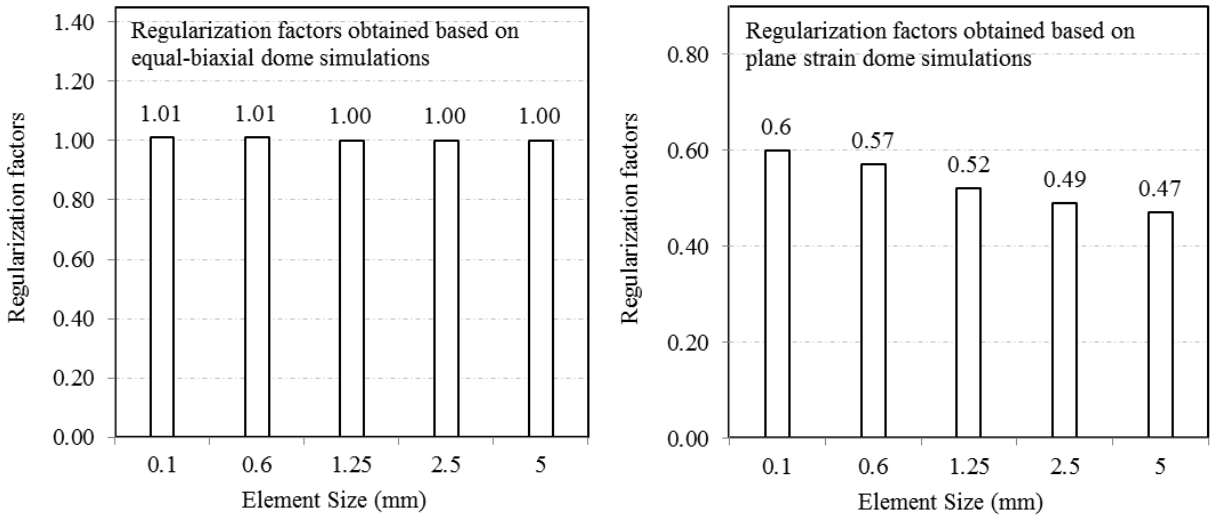

Figure 45: Regularization curves for AA7075-T6 [139]

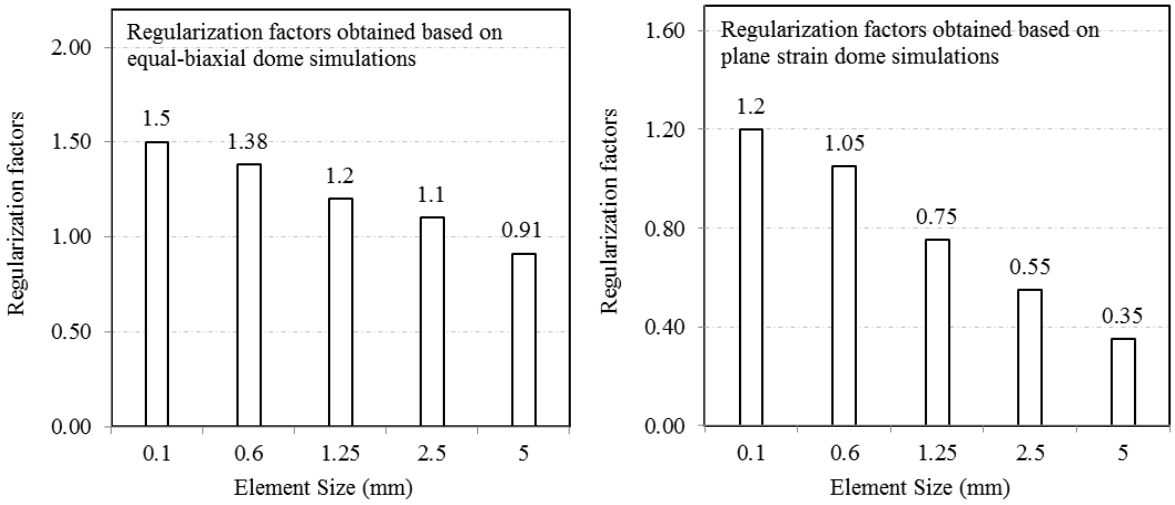

Figure 46: Regularization curves for AA6013-T6 [139]

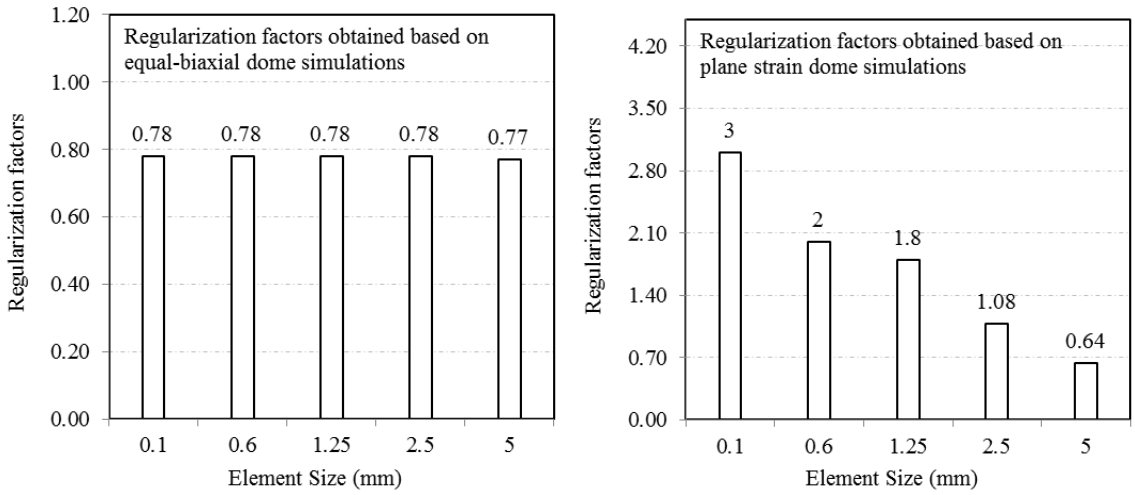

Figure 47: Regularization curves for AA7xxx-T76 [139]

4.2.2 Three-Point Bend Meshes

The beam and backing plate were modeled using 2.5 mm x 2.5 mm shell elements, shown in Figure 48. Fully integrated "Type 16" shell elements [131] were utilized with seven integration points through the thickness. The structural model did not adopt symmetry conditions because the run time for the full model was relatively short. Note that the thinning predicted in the forming simulation was quite low (less than 1 %). As a result, the bending models used the initial sheet thickness of 2.0 mm.

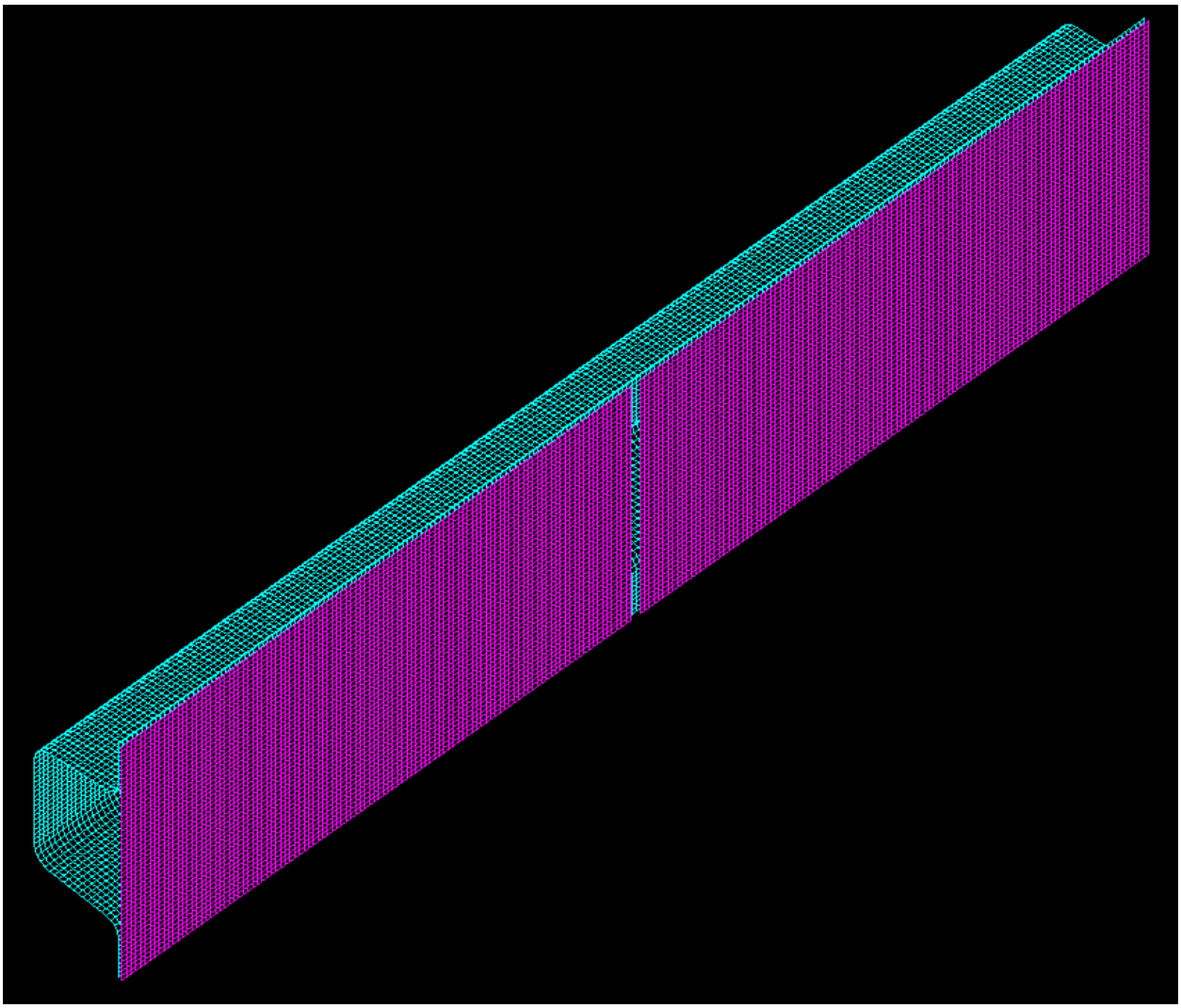

Figure 48: Backing plate mesh and location with respect to the channel

4.2.3 Rivet Model

The rivets joining the top hat section and baseplate were initially modeled using a *CONSTRAINED_SPOTWELD element, which uses rigid beam elements connecting a node on the top hat to the corresponding node on the baseplate, as can be seen in Figure 49. The beam elements were assigned a normal and shear failure stress at which the beam element would delete and the nodes have the possibility to separate. The peak force from the cross tension and lap shear

experiments performed on the rivets (described in Appendix A on Figure 99) were used to define the beam element strength data and are summarized in Table 18.

Table 18: 5 kN Rivet measurements

Ultimate Shear Strength	5.5 kN
Ultimate Tensile Strength	6.7 kN

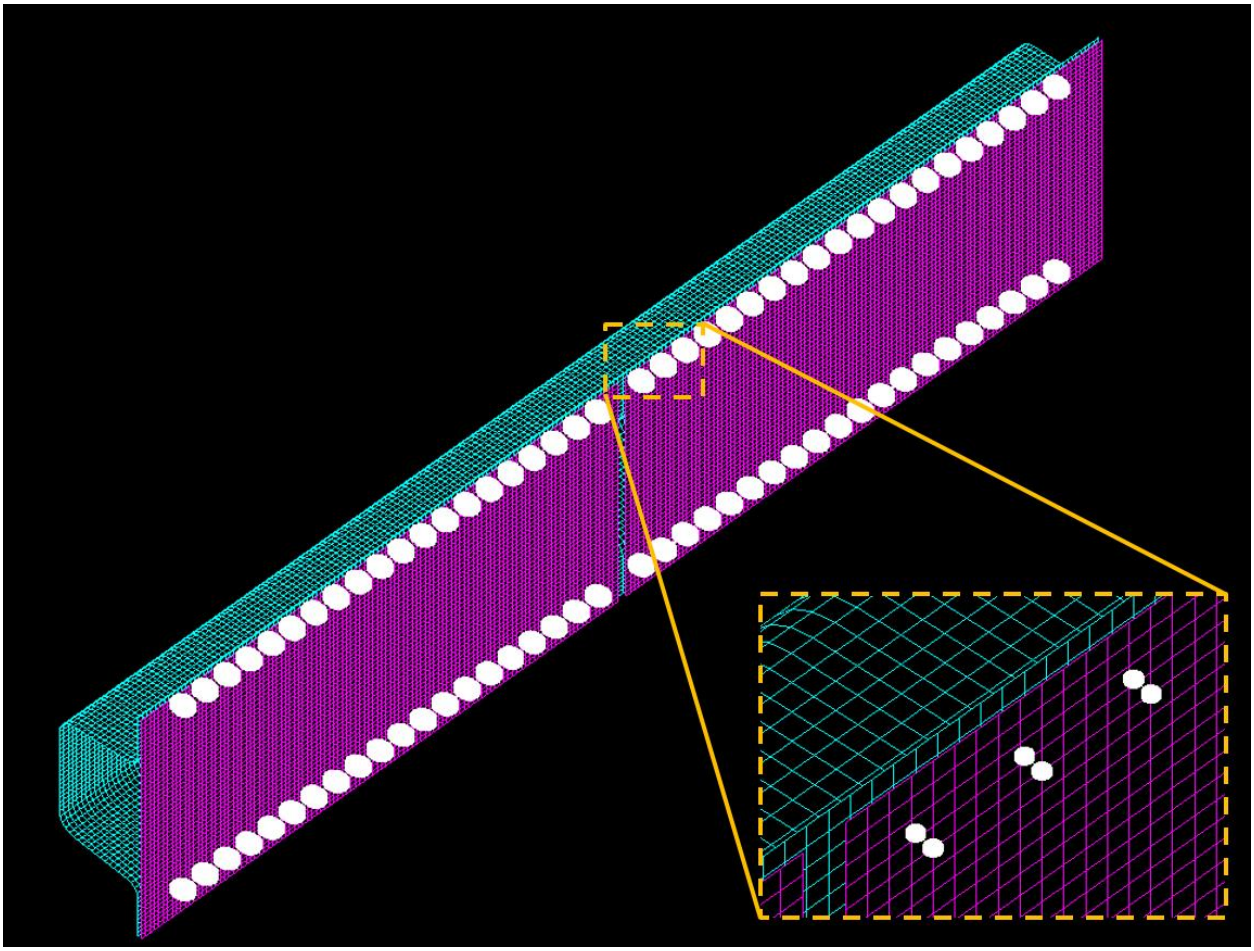

Figure 49: Rivet location and beam element nodes

Although the beam elements were initially used to account for the rivets, preliminary dynamic and quasi-static numerical simulations showed that the rivets did not fail under the three-point bend test loading. Since there was no failure, the beam elements were replaced with a *CONSTRAINED_RIVET constraint, which

simply tied the two nodes together without failure. This simplification allowed for somewhat shorter computational times and was further justified during experimental testing in which the material around the rivets and the rivets themselves did not fail.

4.2.4 Boundary Conditions – Quasi-static Model

The tup and supports were discretized using shell elements with a size of 5 mm x 5 mm, as seen in Figure 50. Only the surfaces of the tup and supports were discretized and were assigned a rigid non-deformable material model. For the impactor, only the lower half of the tup was modeled since it was not necessary to model the full tup. Similarly, only the upper half of the supports were discretized.

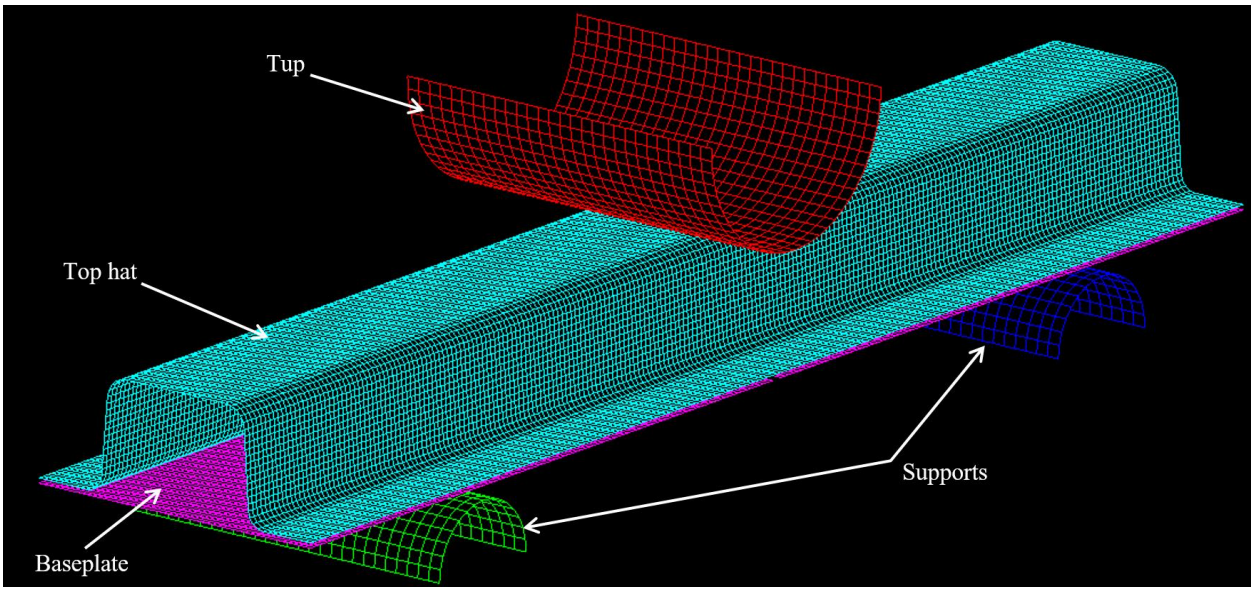

Figure 50: Setup of the quasi-static three-point bend test model

The supports were fixed in space and the impact beam was able to rest on them during the initial stages of the simulation. A penalty function-based contact algorithm was implemented between the beam and the tup and between the beam and the supports(*CONTACT_SURFACE_TO_SURFACE). The coefficient of friction

between the all contacting surfaces was set to 0.05 [119] to emulate the Teflon film placed between the test article and the fixtures.

The tup was given a prescribed downward motion of 0.508 mm/s towards the beam and the simulation was terminated when the tup extended 200 mm downwards. No mass scaling was used in the quasi-static simulation.

4.2.5 Boundary Conditions – Dynamic

The dynamic simulations used the identical boundary conditions and mesh as in the quasi-static model but with two changes. The mass of the tup was set to 960 kg, equivalent to the mass of the sled assembly. The second change was that instead of the tup having a constant velocity of 0.508 mm/s, it was given an initial velocity of 7 m/s, corresponding to the dynamic experiments. No mass scaling was considered because the impact test is already a dynamic event and mass-scaling would introduce non-physical inertial effects.

5 EXPERIMENTAL RESULTS AND MODEL PREDICTIONS

This chapter serves to present the experimental results from the die quenching and warm forming experiments, as well as the subsequent three-point bending experiments. In addition, the model predictions for the die quenched components are also presented and compared to experiment.

5.1 Die Quenching Results

5.1.1 Effective Plastic Strain and Temperature History during Quenching

Contours of effective plastic strain at different points in the forming and quenching operation (t=0.6, t=1 and t= 5 s) are plotted in Figure 51. These predictions provide insight into the amount of pre-strain the channel experiences before being subjected to the three-point bend test.

It can be seen in Figure 51 that majority of the strain is induced by the bending of the sheet around the radius with a maximum plastic strain of 16% in the outer surface of the channel. Low strains were observed in the sidewall region of the channel due to the fact that the deformation largely comprises bending at the punch nose and bending/unbending as the material traverses the die entry radius with very little membrane straining. This limited stretching in the sidewall is in line with the low amount of material thinning seen in the model (Figure 52).

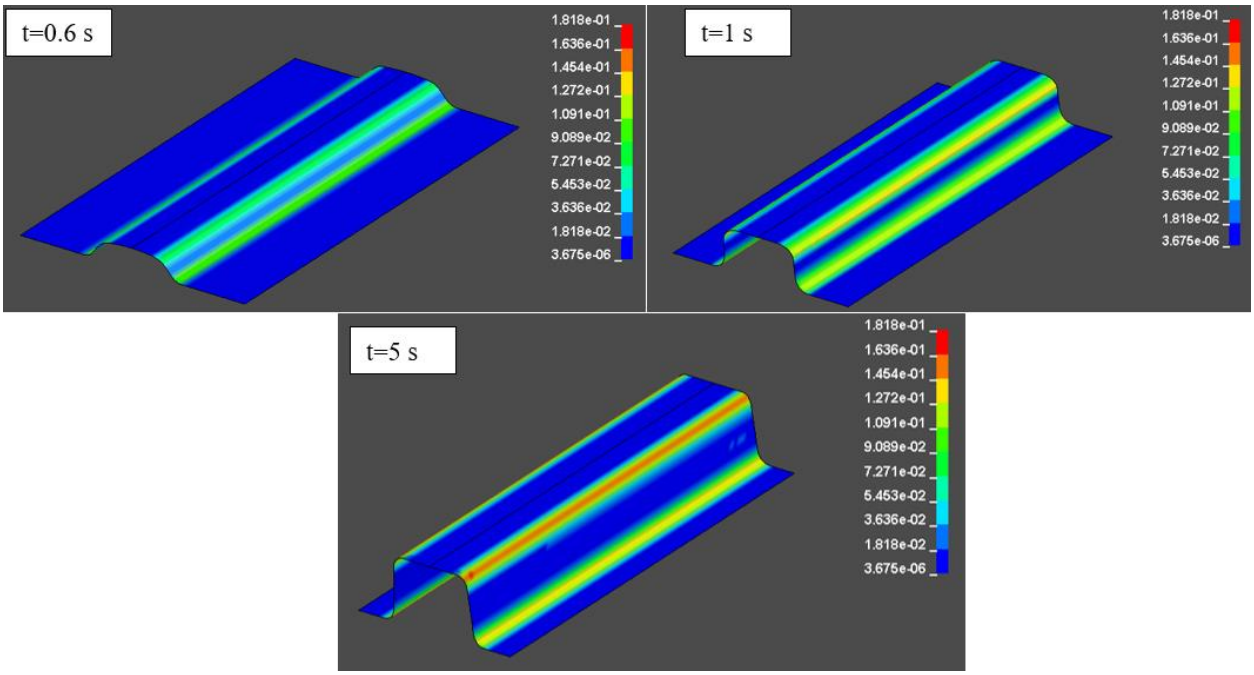

Figure 51: Contours of effective plastic strain on top surface of the AA7075 channel during the die quenching simulation

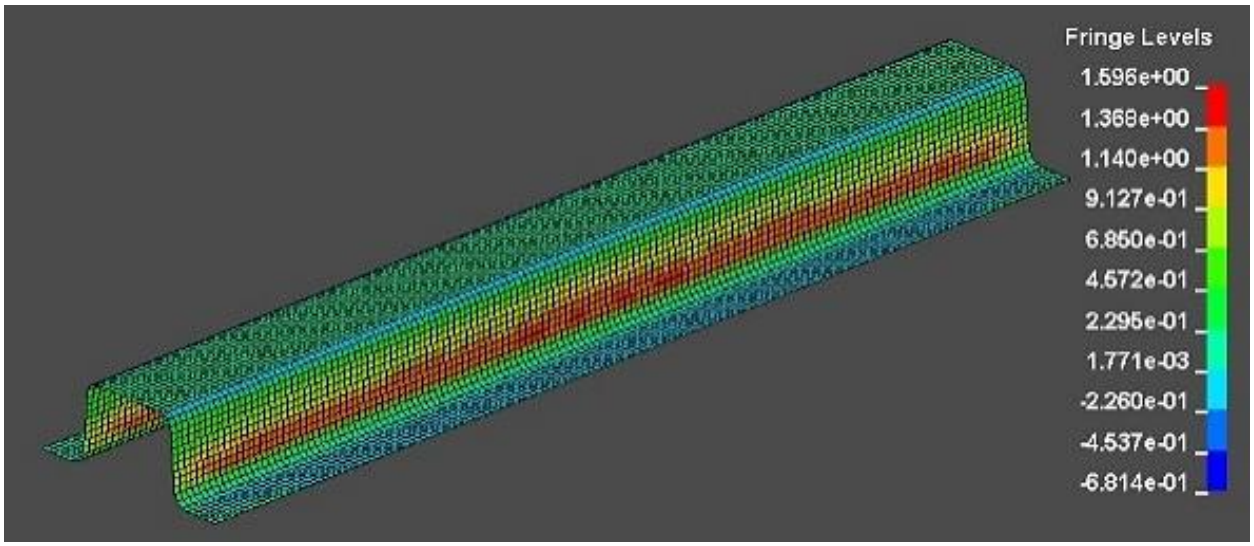

Figure 52: Contour plot of predicted percent thickness reduction for die quenched AA7075 channel.

Contours of temperature within the sheet at t=0.6, t=1 and t=5 s are plotted in Figure 53 and demonstrate the rapid temperature drop during the die quenching operation. The predicted temperature history of a node at the apex of the radius

which connects the channel's top section and sidewall is plotted in Figure 54. This corresponds to a nominal quench rate of 160°C/s which is sufficient to ensure that the material enters a SSSS [123].

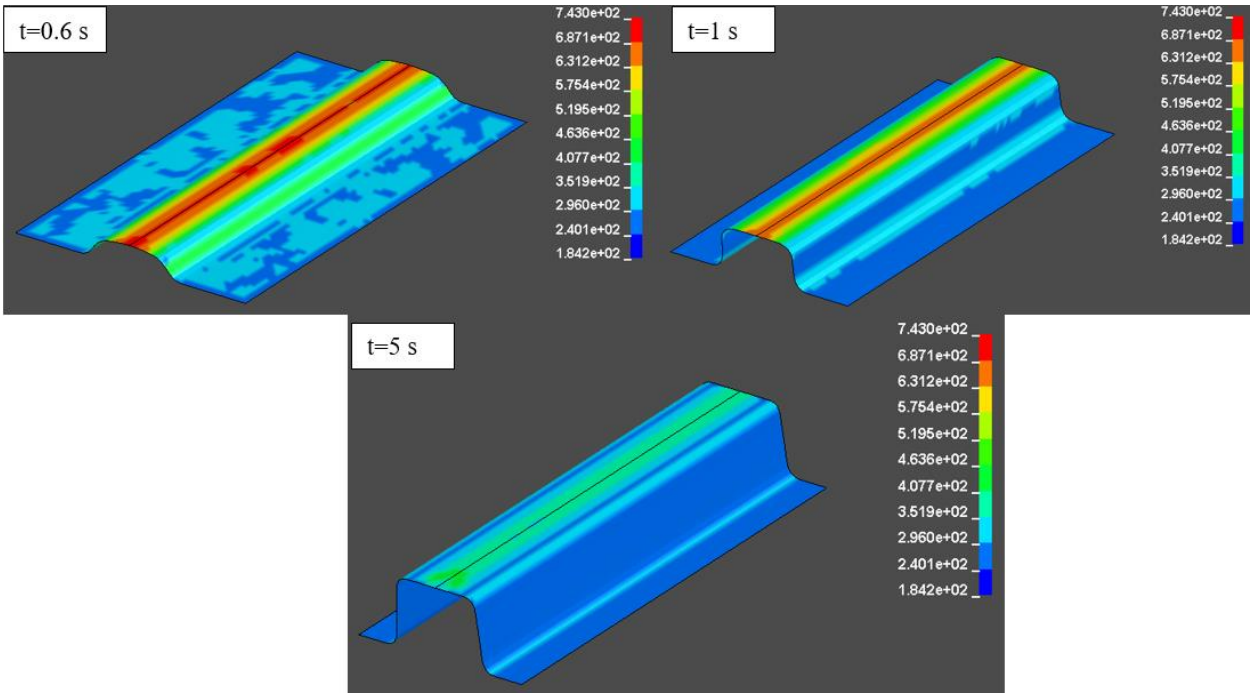

Figure 53: Contours of temperature during the die quenching simulation of AA7075 in degrees Kelvin

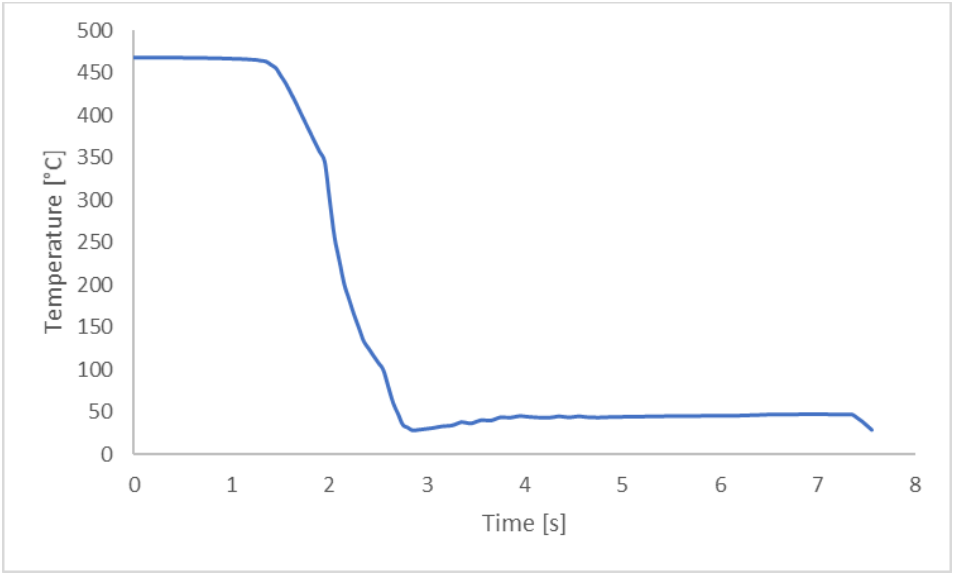

Figure 54: Simulated temperature drop of the blank during the die quenching process

5.1.2 Thinning during Die Quenching

Thickness measurements were taken from specimens cut from two locations along the channel, in the middle and 50 mm from the end of the channel, shown in Figure 55. The test specimen was cut into strips and polished to 2400 grit sandpaper to create a flat cross-section. The strips were then scanned and thickness was measured using a MATLAB code. The thickness data from the experiments were compared to the finite element simulation using the percent thickness reduction data shown in Table 19. This data is shown in Table 19, from which it can be observed that both the experiments and finite element predictions reveal very little thickness change.

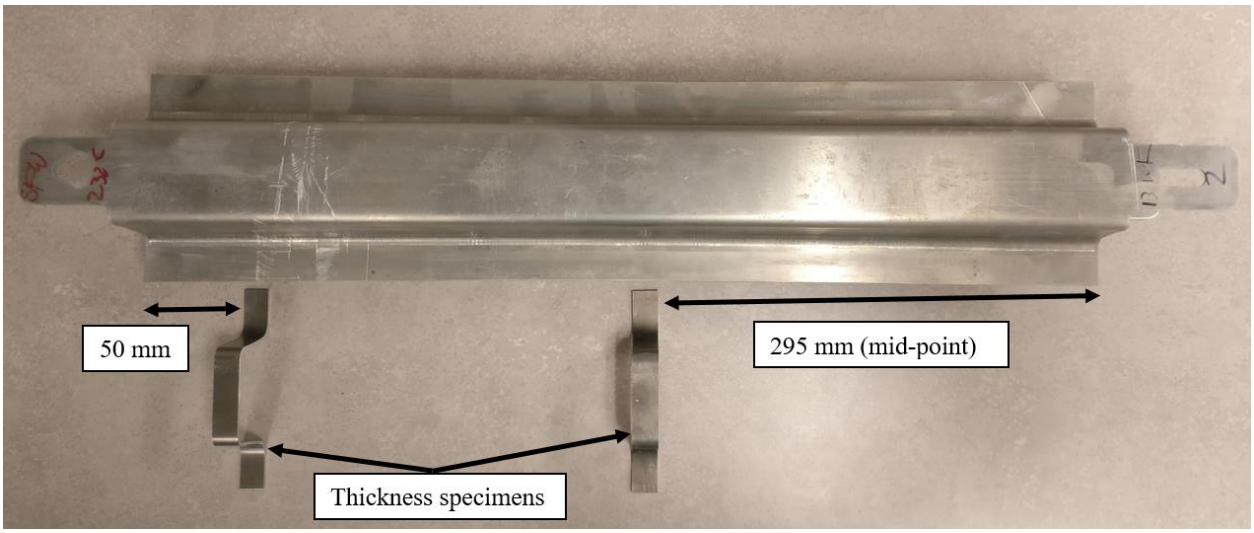

Figure 55: Thickness specimen locations with respect to the channel length

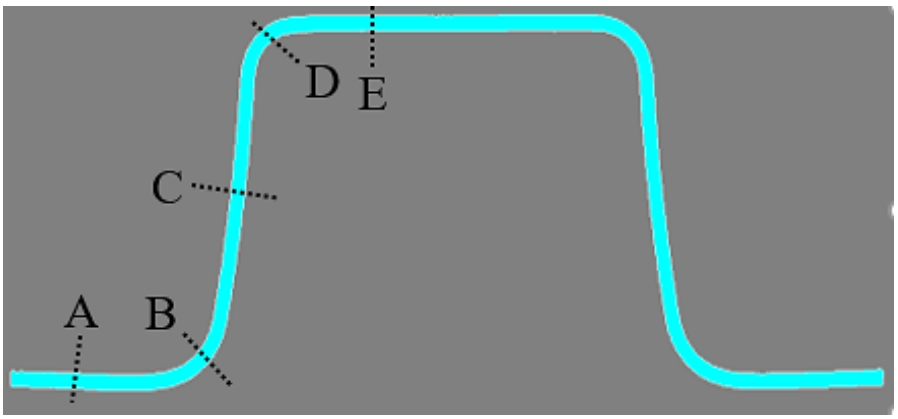

Figure 56: Formed channel thickness measurement locations

Table 19: Measured and predicted percent thickness reductions

Measurement Location	End Beam Location		Mid Beam Location	
	Experiment	Simulation	Experiment	Simulation
A	0	0	0	0
B	0.03%	0.04%	0.02%	0.03%
C	0.03%	0.70%	0.03%	0.91%
D	0.03%	0.10%	0.03%	0.09%
E	0.12%	0.10%	0.03%	0.09%

The material in the experiment experienced a maximum of 0.12% material thinning at location **E** which is very small and lies within the measurement precision. In general, the model predictions are consistent with the measured data insofar as thinning is almost non-existent.

5.1.3 Measured Micro Hardness in Die Quenched Parts

Micro hardness measurements were conducted to verify that the material has been heat treated to the correct temper. Micro hardness samples were taken from the middle of the channel.

Three micro hardness measurements were taken through the thickness of the material, each equidistant from one another and the edge of the material. The measured hardness values for the die quenched and aged rails are shown in Table 20.

Table 20: Hardness measurements of die quenched beams at various locations in HV

Material and Heat Treatments	Vickers Microhardness			
	Top	**Sidewall**	**Flange**	**Average**
As received AA7075-T6	182			
DQ AA7075-T6	182	177	179	179
AA7075-6IPB	181	177	178	179
As received AA7xxx-T76	168			
DQ AA7xxx-T76	169	162	167	166
AA7xxx-76IPB	169	161	166	165

The Vickers hardness measurements showed that for both 7000-series alloys, the IPB and the regular T6 or T76 heat treatment schedules resulted in similar final hardness levels. Comparing the conventional and IPB heat treated micro hardness measurements with measurements from the as-received sheet, demonstrates that the die quenched material has reached the desired temper of the as-received material.

5.2 Quasi-Static Three-point Bend Experiments

Quasi-static three-point bend experiments were conducted on all three materials in the various forming conditions. All three materials were subjected to the warm forming process route starting with the as-received T6 or T76 temper, while the under-aged (UA) warm forming process route was only considered for the AA6013 and AA7xxx alloys. The die quenching process was only considered for the AA7075 and developmental 7xxx alloy. For all of the experiments, none of the materials failed around the rivets, nor did the rivets fail.

All of the specimens which underwent quasi-static testing folded at the centre of the beam without wrapping around the impactor. The beams, in both the simulations and experiments, folded directly under the impactor, as seen in Figure 57.

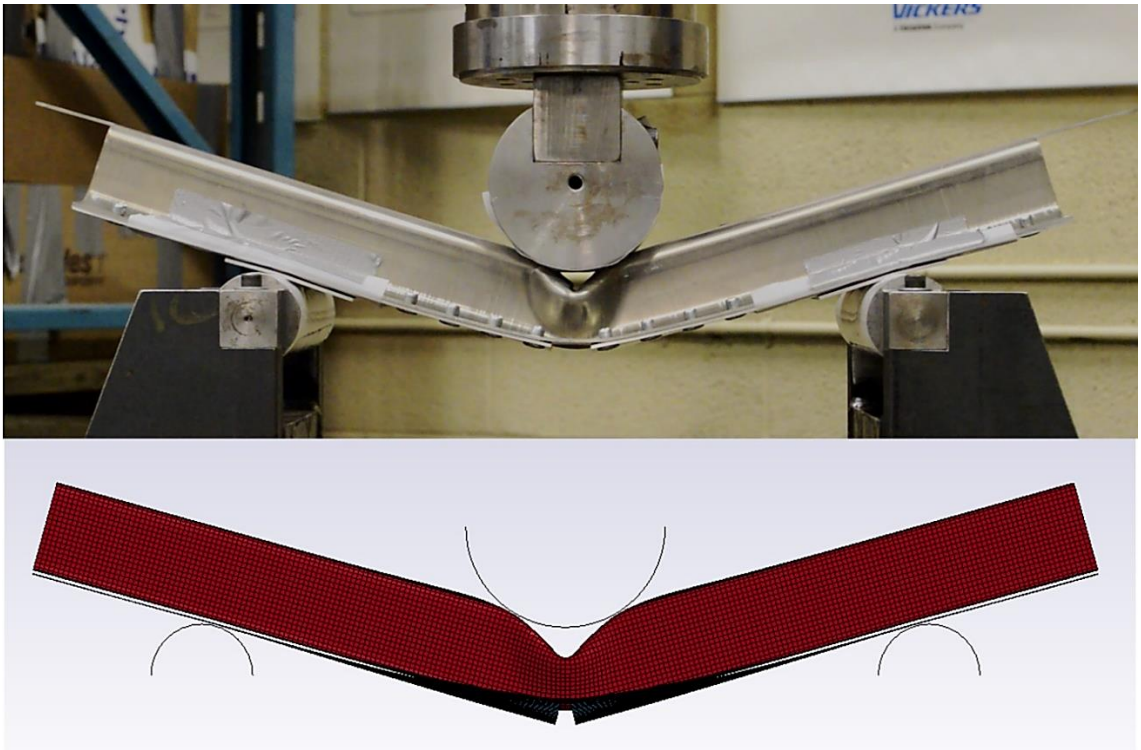

Figure 57: Folding during quasi-static three-point bend loading in experiments (top) and simulation (bottom)

The following sections present the force and absorbed energy versus displacement response for each material condition. All energy absorption curves were determined using a forward integration of the respective force-displacement curves. In this chapter, only a “median curve” is presented for each condition, however, the three repeat experiments for each condition are plotted in Appendix B of this thesis from which the scatter is seen to be quite low for most cases.

5.2.1 Warm Formed Beams

Figure 58 shows the force-displacement and absorbed energy results for the quasi-static tests done with AA6013. None of the warm formed AA6013 beams exhibited visible cracking, as seen in Figure 59. Examination of Figure 58 shows that the beams formed under non-isothermal conditions (cold tools) exhibited the highest peak load of 15.4 kN at a punch displacement of 21.5 mm. The beams formed under isothermal conditions (heated tools) at temperatures of 200°C and 232°C had similar peak loads and absorbed energy. The 200°C isothermally formed material had a peak load of 14.6 kN at an impactor displacement of 18.7 mm, while the 232°C isothermally formed material had a peak load of 14.4 kN at an impactor displacement of 17.8 mm. The under-aged material after paint bake exhibited similar strength to the 232°C isothermally formed beam. The near equivalent strength indicates that the UA warm forming process and the subsequent paint bake cycle was sufficient to bring the material to a strength comparable to conventional warm forming processes starting with peak aged sheet. The peak load for the under-aged material is 13.9 kN at an impactor displacement of 19.7 mm. The under-aged material that did not undergo the paint bake cycle exhibited considerably lower strength, but did not fracture. The lower strength indicates that

the warm forming process alone was not sufficient to bring the material to peak age after forming. The peak load for the under-aged material is 9.9 kN at an impactor displacement of 26.2 mm.

The total energy absorbed for the 232°C non-isothermally formed material is 0.83 kJ. The 200°C and 232°C isothermally formed material had energy absorption values of 0.80 kJ and 0.79 kJ, respectively. The under-aged material had an energy absorption value of 0.80 kJ. The under-aged material without the paint bake cycle had an energy absorption value of 0.66 kJ. The total energy absorption values are determined at a punch displacement of 86.5 mm.

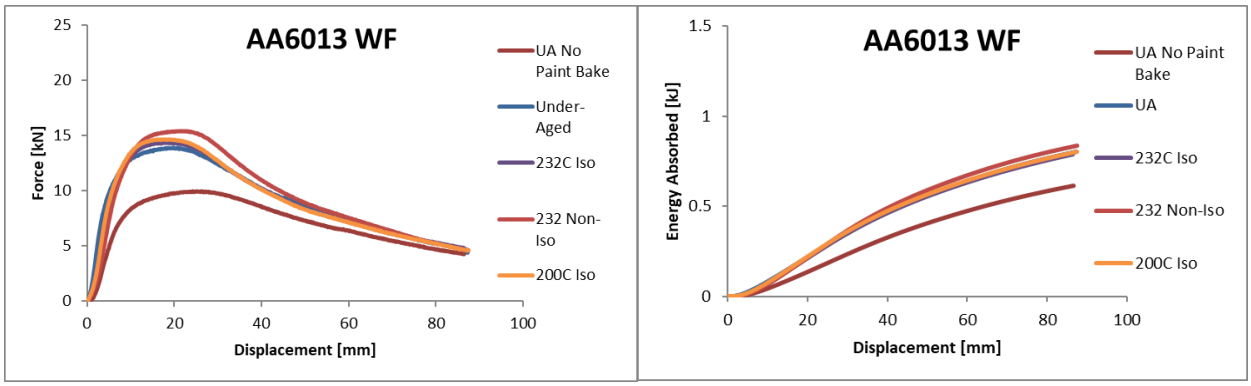

Figure 58: Experimental quasi-static force-displacement (left) and absorbed energy (right) comparison for warm formed AA6013 beams

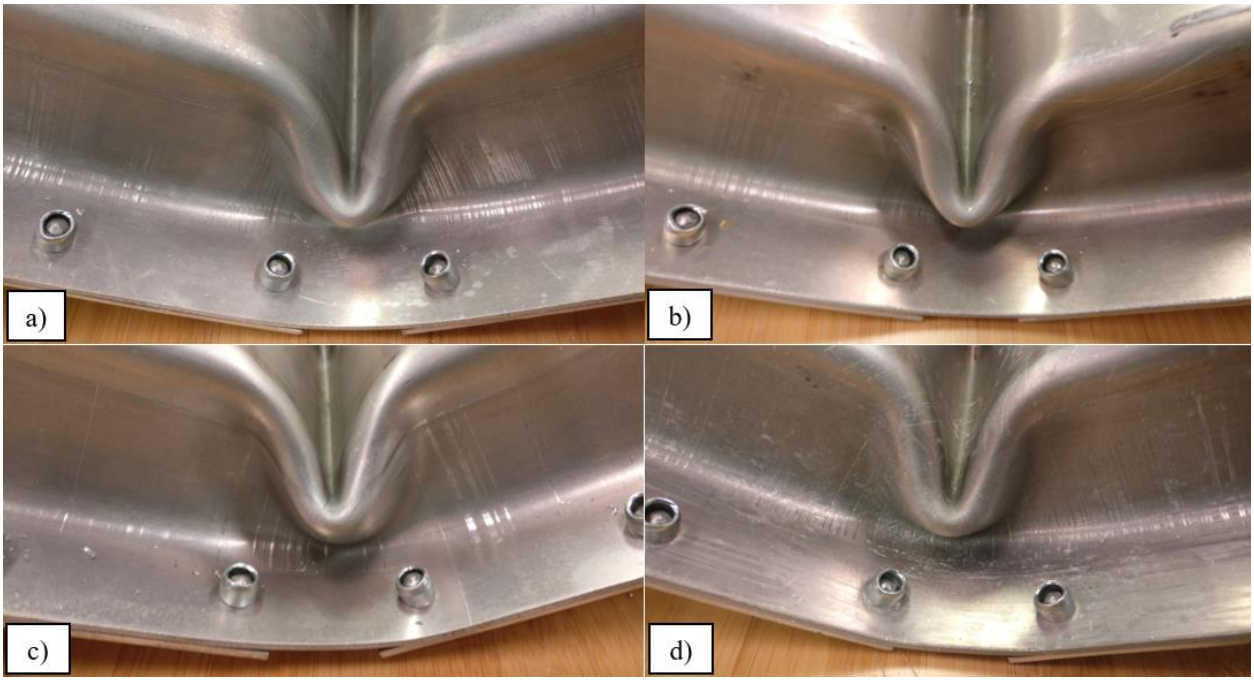

Figure 59: AA6013 folded region of a) 200°C isothermally formed b) 232°C isothermally formed c) 232°C non-isothermally formed d) under-aged beams

Figure 60 shows the force-displacement and absorbed energy results for the quasi-static tests done with the warm formed AA7075 beams. The figure shows that the non-isothermal forming samples have the highest peak load of 21.97 kN at a punch displacement of 22.57 mm. The 200°C isothermally formed material had a peak load of 19.86 kN at an impactor displacement of 19.98 mm, while the 232°C isothermally formed material had a peak load of 18.35 kN at an impactor displacement of 18.49 mm.

The total energy absorbed for the 232°C non-isothermally formed material is 0.77 kJ. The 200°C and 232°C isothermally formed material had energy absorption values of 0.96 kJ and 0.94 kJ respectively.

Although the non-isothermally formed material had a higher peak load, the total energy absorbed was still less than its isothermally formed counterpart. This is a result of the onset of fracture at an earlier punch displacement in the less

ductile non-isothermal material shown in Figure 61. The fracture initiated at the vertex of the fold indicated by the red arrows in Figure 61. The resulting propagation of fracture caused the serrations in the load curve and a pronounced load drop-off after the peak load, resulting in the lower total absorbed energy. The total energy absorption values are determined at a punch displacement of 86.5 mm.

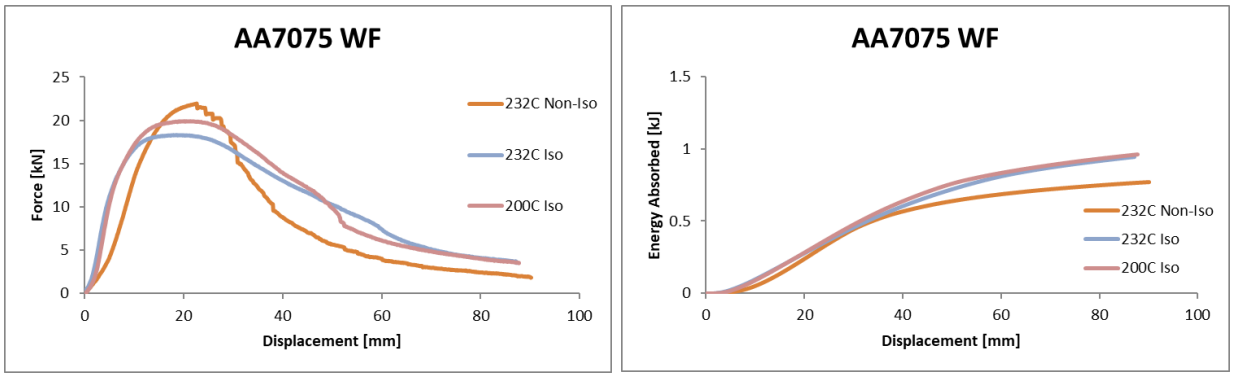

Figure 60: Experimental quasi-static force-displacement (left) and absorbed energy (right) comparison for warm formed AA7075

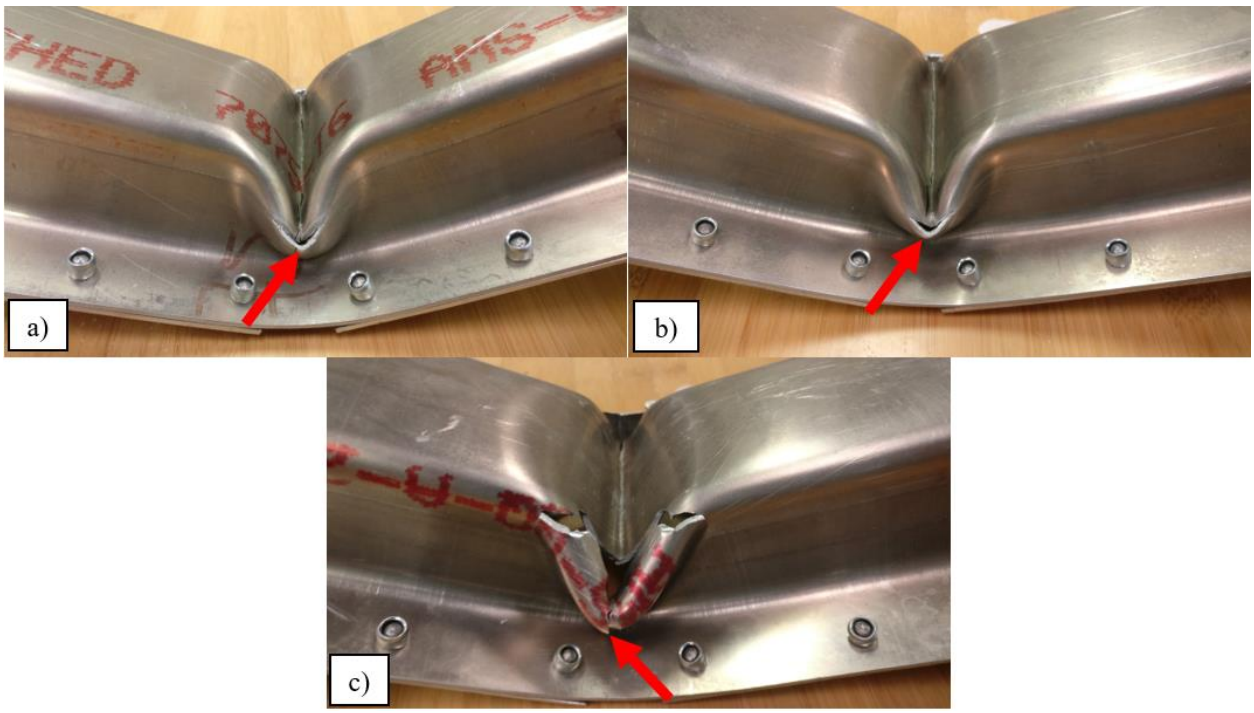

Figure 61: AA7075 folded region of a) 200°C isothermally formed b) 232°C isothermally formed c) 232°C non-isothermally formed

Figure 62 shows the force-displacement and energy absorption results for the quasi-static tests done with the developmental AA7xxx alloy. The figure shows that non-isothermal forming resulted in the highest peak load of 20.0 kN at a punch displacement of 21.5 mm. The 200°C isothermally formed material had a peak load of 17.7 kN at an impactor displacement of 19.5 mm, while the 232°C isothermally formed material had a peak load of 16.1 kN at an impactor displacement of 17.8 mm. The under-aged material performed similarly to the 200°C isothermally formed beams, but did experience minor cracking shown in Figure 63 d). The peak load for the under-aged material is 17.5 kN at an impactor displacement of 20.8 mm. The under-aged material without the paint bake cycle exhibited a significantly lower peak force of 13.8 kN at an impactor displacement of 26.1 mm.

The total energy absorbed for the 232°C non-isothermally formed material is 1.05 kJ. The 200°C and 232°C isothermally formed material had energy absorption values of 0.98 kJ and 0.90 kJ respectively. The under-aged material had an energy absorption value of 0.96 kJ. The under-aged material without the paint bake cycle had a total absorbed energy of 0.74 kJ. The total energy absorption values are determined at a punch displacement of 86.5 mm.

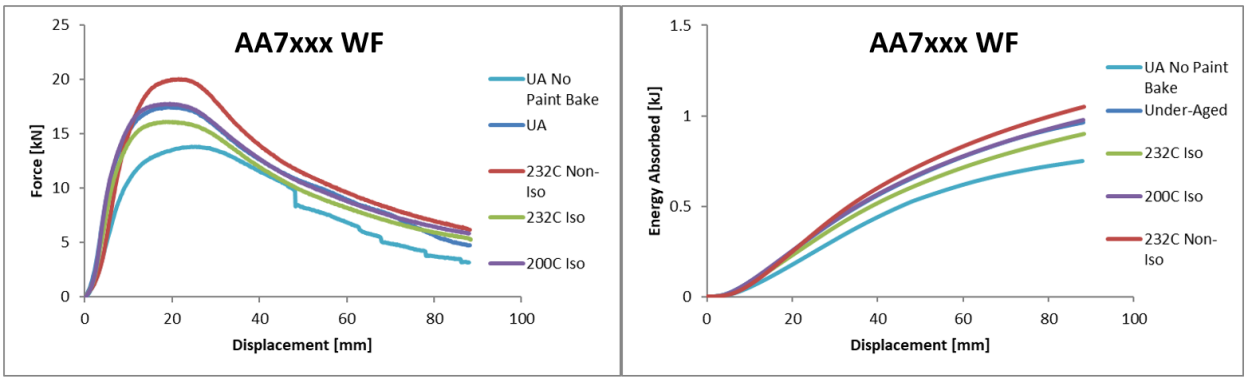

Figure 62: Experimental quasi-static force-displacement (left) and energy absorbed (right) comparison for warm formed AA7xxx

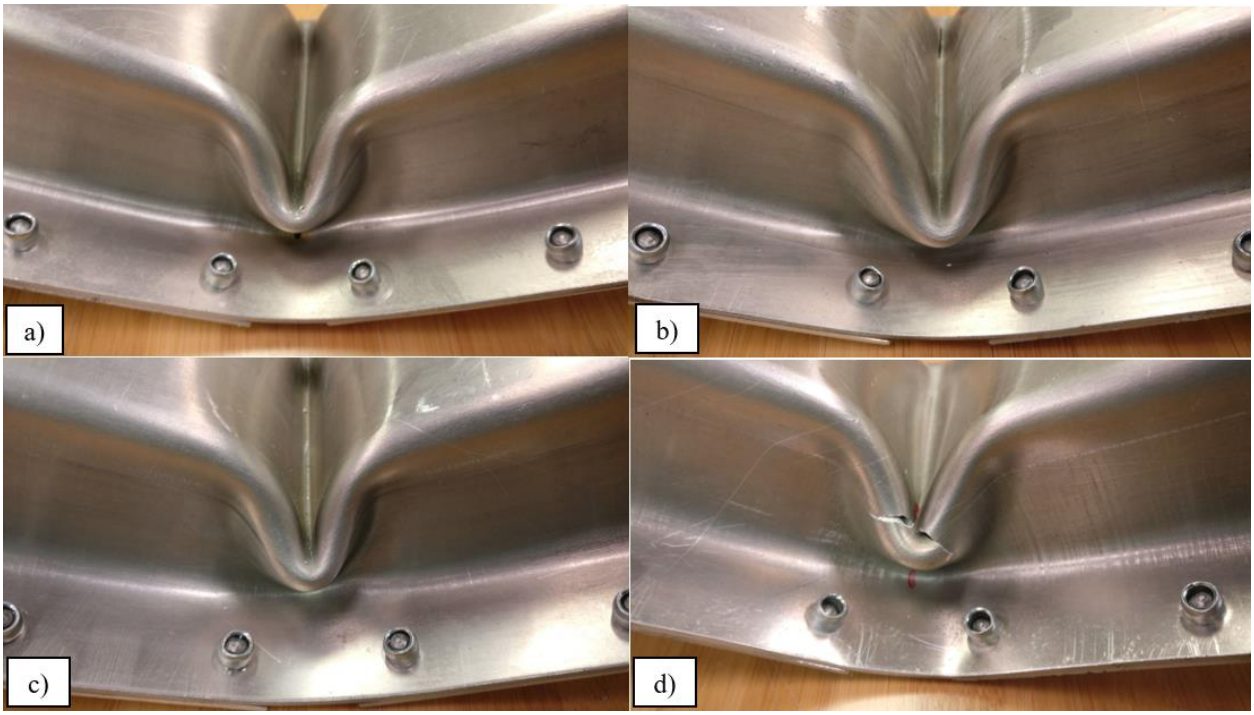

Figure 63: AA7xxx folded region of a) 200°C isothermally formed b) 232°C isothermally formed c) 232°C non-isothermally formed d) under-aged beams

5.2.2 Die Quenched Beams

The quasi-static die quenched three-point bend response of AA7075 and AA7xxx are shown in Figure 64 and Figure 65, respectively. Both the T6 and T6IPB tempers of the AA7075 beams exhibit the same peak force of 19.6 kN at an impactor displacement of 23.1 mm. The total energy absorbed at an indentor displacement of 77.8 mm is 1.02 kJ for both AA7075 tempers.

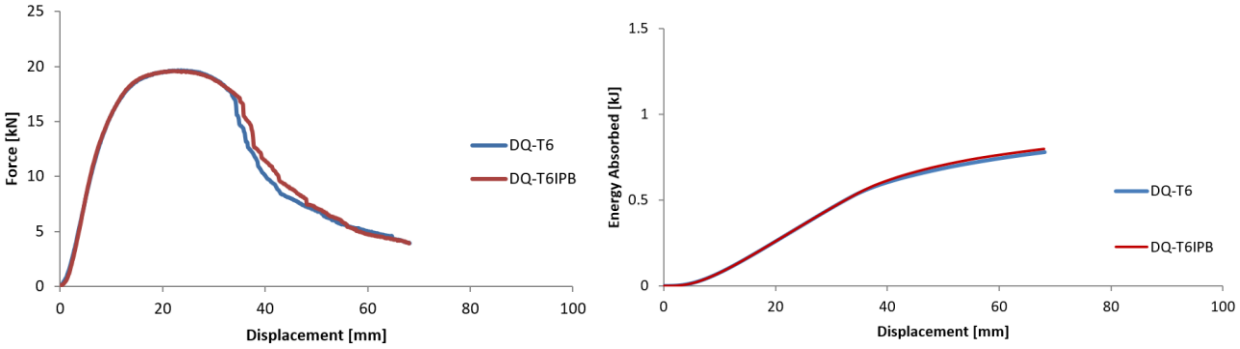

Figure 64: Experimental quasi-static force-displacement (left) and energy absorbed (right) comparison for die quenched AA7075

The peak load for the T76 material was 17.9 kN at an impactor displacement of 20.5 mm while the T76IPB material had a peak load of 16.8 kN at an impactor displacement of 20.5 mm. The energy absorbed by the T76 and T76 IPB were 0.82 kJ and 0.80 kJ respectively at an indentor displacement of 64.1 mm.

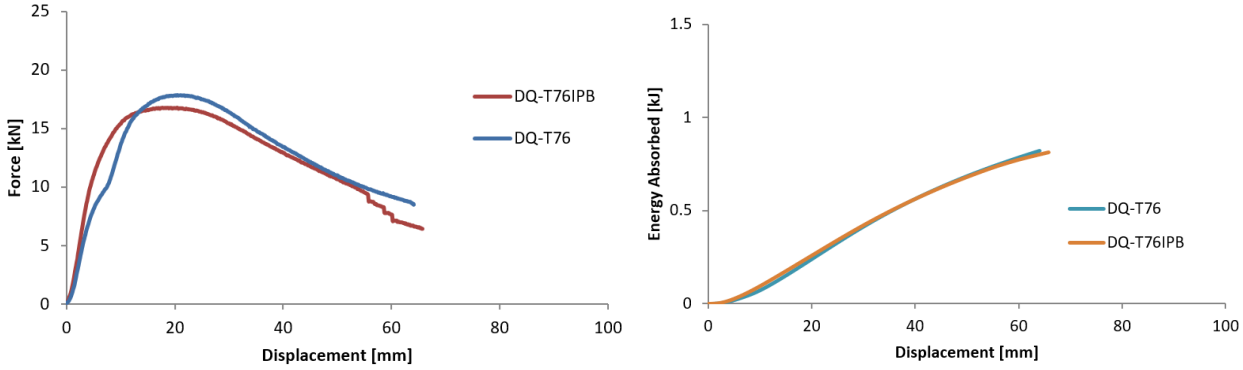

Figure 65: Experimental quasi-static force-displacement (left) and energy absorbed (right) comparison for die quenched AA7xxx

The extent of cracking the die quenched beams can be seen in Figure 66.The 7075 has a higher peak load but lower ductility and thus has a more pronounced load drop-off after the peak load compared to the AA7xxx. This drop is due to the fact that after the peak load, the beam begins to have a greater fold angle and the material begins to fracture, causing the load drop. The AA7xxx material does not

facture with the increasing fold angle and thus has a more gradual decrease in load compared to AA7075.

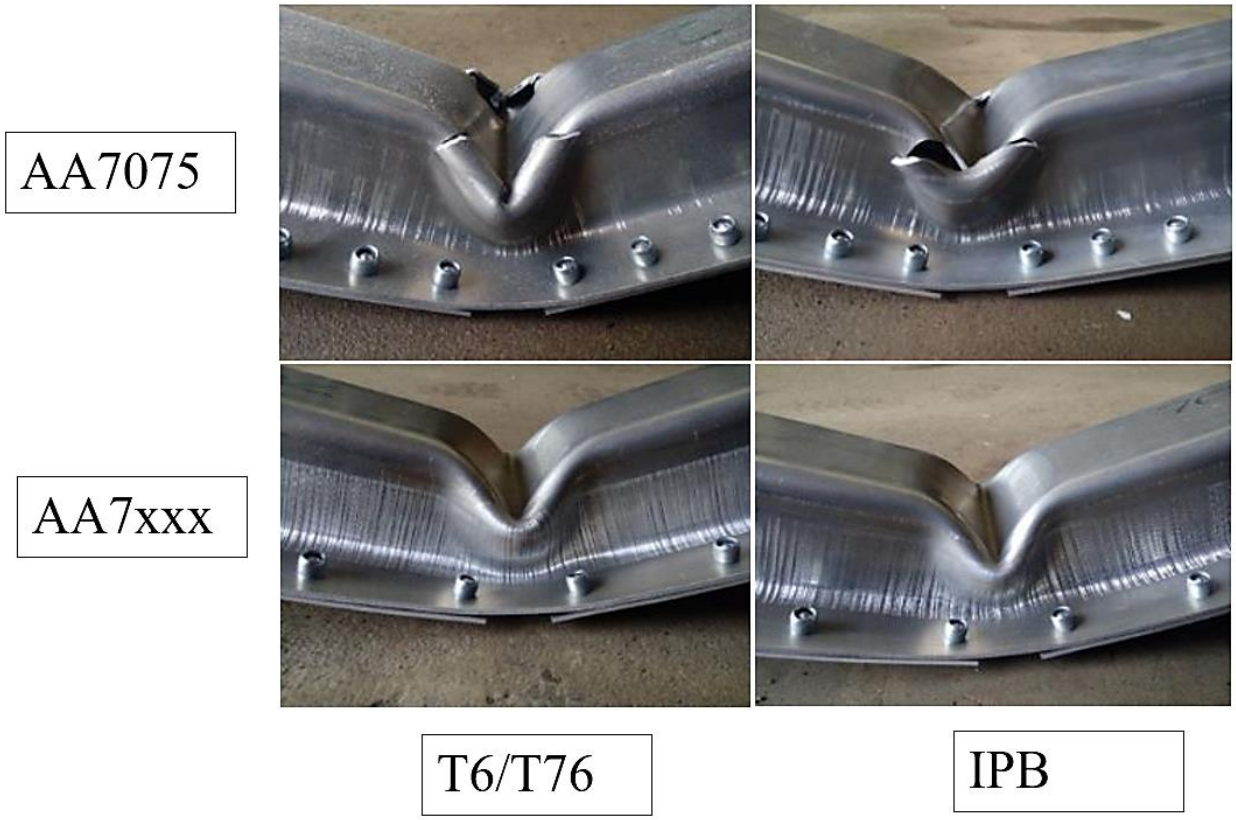

Figure 66: Deformed AA7075-T6/T6IPB and AA7xxx-T76/T76IPB beams

5.3 Dynamic Three-point Bend Test

Dynamic three-point bend experiments were conducted on the 7000-series beams fabricated using the die quenching process. For all of the experiments, none of the materials failed around the rivets, nor did the rivets fail.

The crash sled facility used honeycomb crush blocks to arrest the sled near the end of the impact event. The honeycomb was positioned so as to contact the sled after 60 mm of “free crush” of the beam. For reference, the honeycomb contact point is indicated in the figures in this section. The AA7075 dynamic three-point bend test data is shown in Figure 67. The data shows that the T6IPB material

has a steeper hardening response during the dynamic test compared to the T6 counterpart. The reason for this steeper response is not known. The IPB material sustained a high load level for a longer duration and consequently absorbed a higher amount of energy.

The peak average peak load for the AA7075-T6 and T6IPB materials are 21.71 kN and 24.35 kN, respectively. The energy absorbed at 60 mm for the T6 and T6IPB are 1.48 kJ and 1.66 kJ respectively.

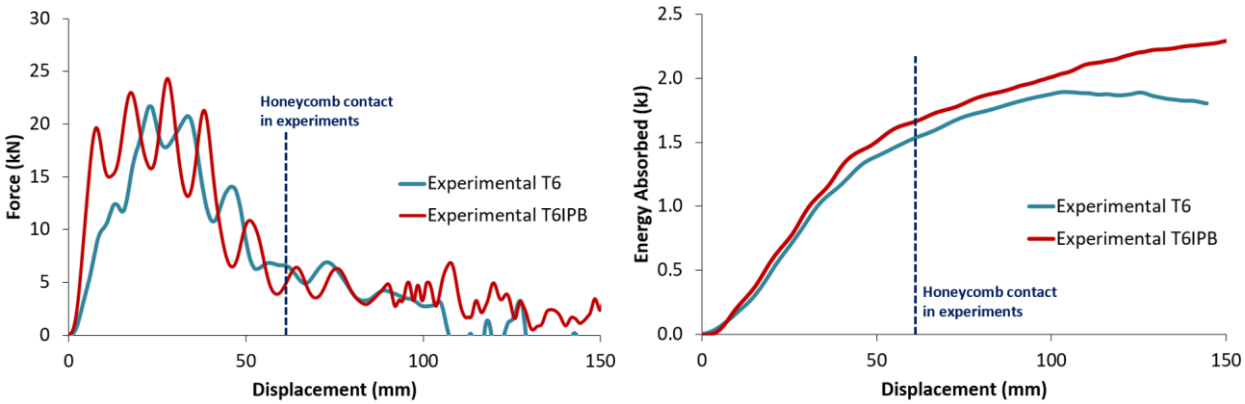

Figure 67: Experimental dynamic force-displacement (left) and energy absorbed (right) comparison for die quenched AA7075

The AA7xxx dynamic three-point bend test data is shown in Figure 68. The data shows that the T76 and the T76IPB material have very similar dynamic responses. The T76 material exhibited more oscillations in the force-displacement data, but that was attributed to the metallic ringing throughout the test equipment and test article.

The peak load for the T76 and T76IPB materials are 24.9 kN and 21.4 kN respectively. The energy absorbed at 60 mm for the T76 and T76IPB are 1.49 kJ and 1.52 kJ, respectively.

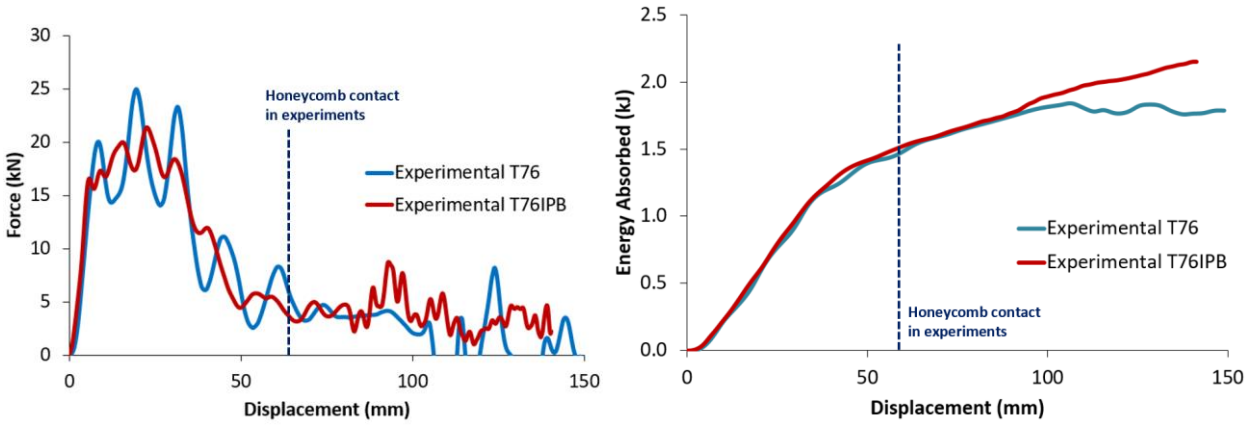

Figure 68: Experimental dynamic force-displacement (left) and energy absorbed (right) comparison for die quenched AA7xxx

5.4 Numerical Predictions

This section presents the results from the numerical simulations of the quasi-static and dynamic experiments. First, the predictions of fracture are presented using the different regularization approaches. This is followed by the static and dynamic predictions.

5.4.1 Calibration of Failure Criteria – Regularization Approach

The experimental results suggest that accurate prediction of the onset of fracture is important to accurately predict the force-displacement and absorbed energy curves. The approach used to predict fracture during the three-point bending experiments utilizes the GISSMO failure criterion [135] which incorporates a mesh regularization treatment to control mesh sensitivity. As described in Section 4.2.1, mesh regularization curves were developed (calibrated) for the materials considered in this study by Rahmaan [139] based on comparison of predictions to either equi-biaxial (EB) or plane strain (PS) dome experiments.

In order to assess the most appropriate regularization curves to use in the current simulations, the predicted and measured force-displacement response for the AA7075-T6 quasi-static and dynamic three-point bend experiments are plotted in Figure 69 and Figure 70. Comparison of the predictions with the measured response demonstrates that the predictions using the PS regularization resulted in premature predictions of failure, whereas the predictions using the EB regularization curve agreed well with experiment and the model without any regularization curve.

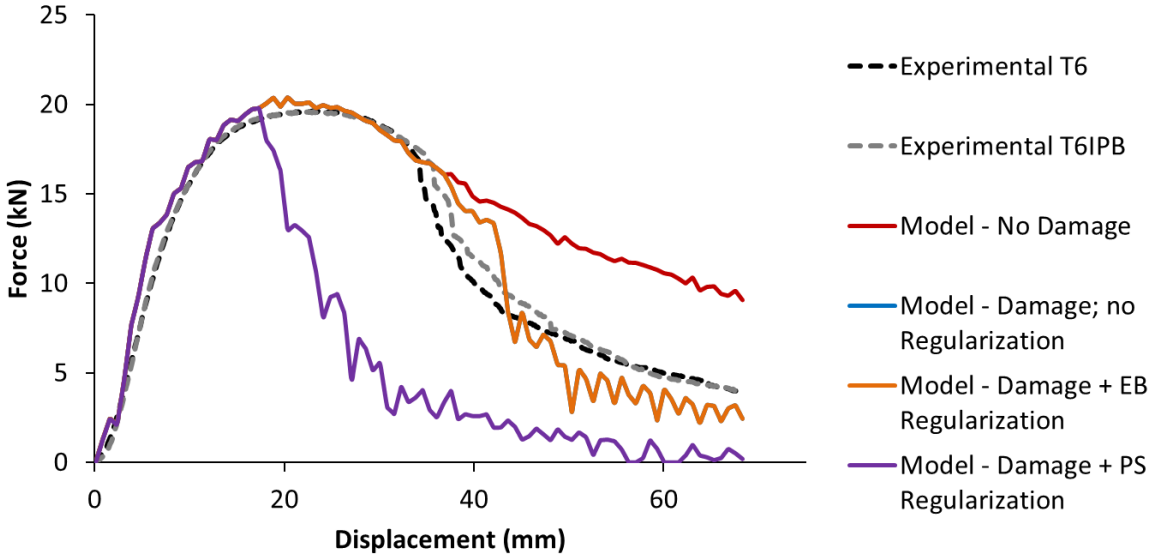

Figure 69: Quasi-static regularization curve comparison for AA7075-T6

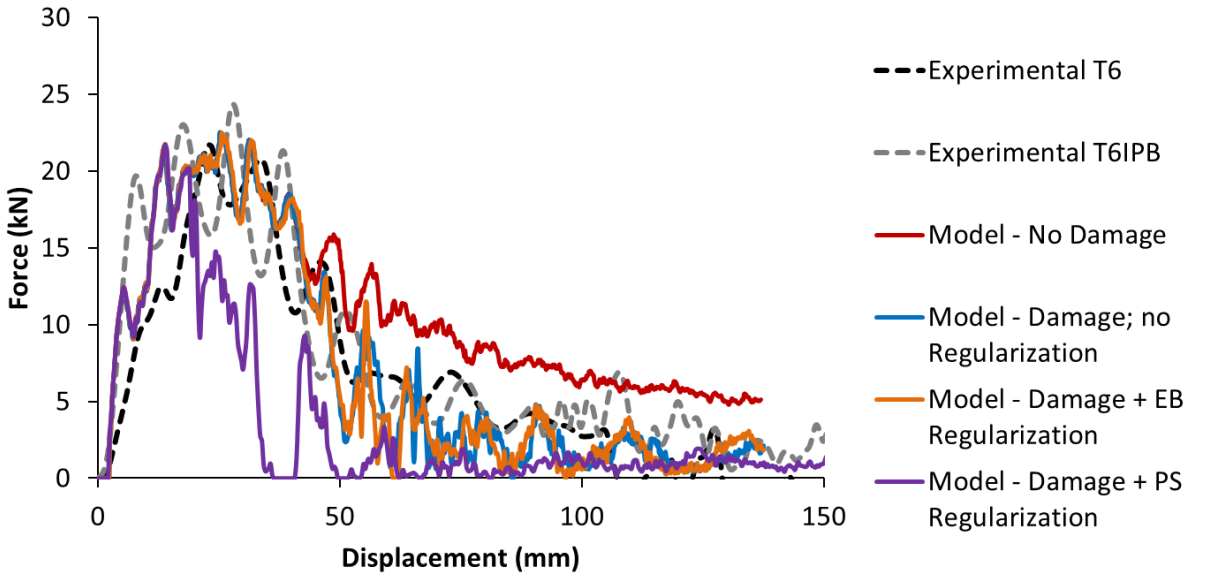

Figure 70: Dynamic regularization curve comparison for AA7075-T6

The numerical model not using the regularization curve and the model using the EB regularization curve fit the experimental data the most accurately. Since the regularization factor for EB is 1.01 it is very similar to the model without the regularization curve. This, in conjunction with the fact that there are oscillations in the force-displacement data, it is not possible to distinguish which model is more accurate.

In the quasi-static PS model, the material began to fail at a punch displacement of 20.25 mm. This was 18.75 mm earlier than the onset of failure in the model using the EB-based regularization curve and the model without any regularization curve which both predicted material failure at a punch displacement of 39 mm. In the dynamic model, the PS material failed at an impactor displacement of 19.2 mm while the EB model and model without regularization failed at 40.6 mm and 40.7 mm, respectively.

The EB model and the model without regularization are the same due to the fact that the regularization curve has a scale factor of 1.0 when the element size is between 1.25 mm and 5 mm.

The progression of the material failure at set impactor displacement can be seen in Figure 71 for the quasi-static loading cases and in Figure 72 for the dynamic cases. It can be seen that the failure in the PS model has progressed much further than the EB and no regularization models at each specified time. This outcome is explained by the fact that the plane strain state exhibits the lowest fracture strain for most materials, and resulted in earlier fracture predictions.

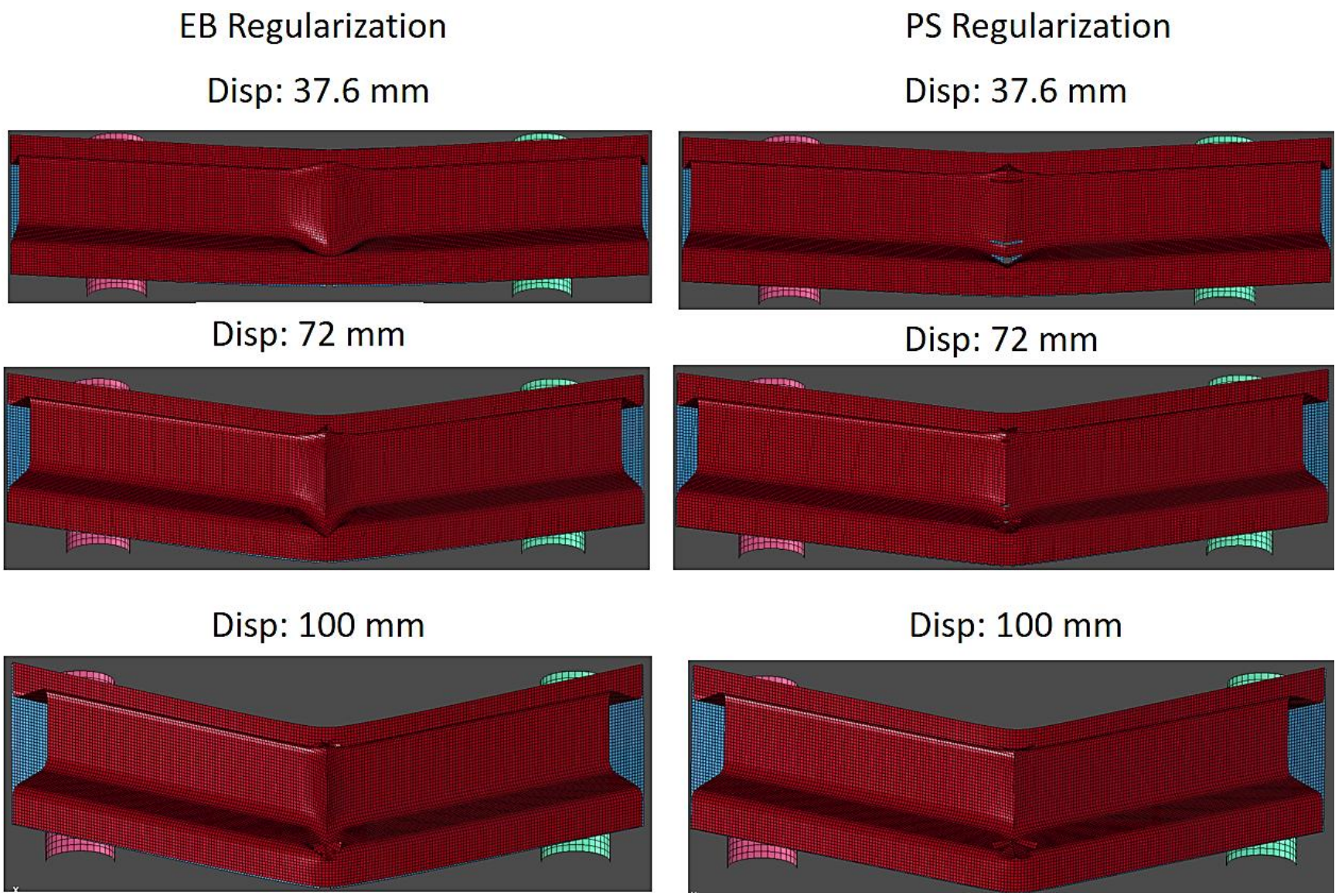

Figure 71: Quasi-static material failure for models using different regularization curves at set impactor displacement for AA7075-T6

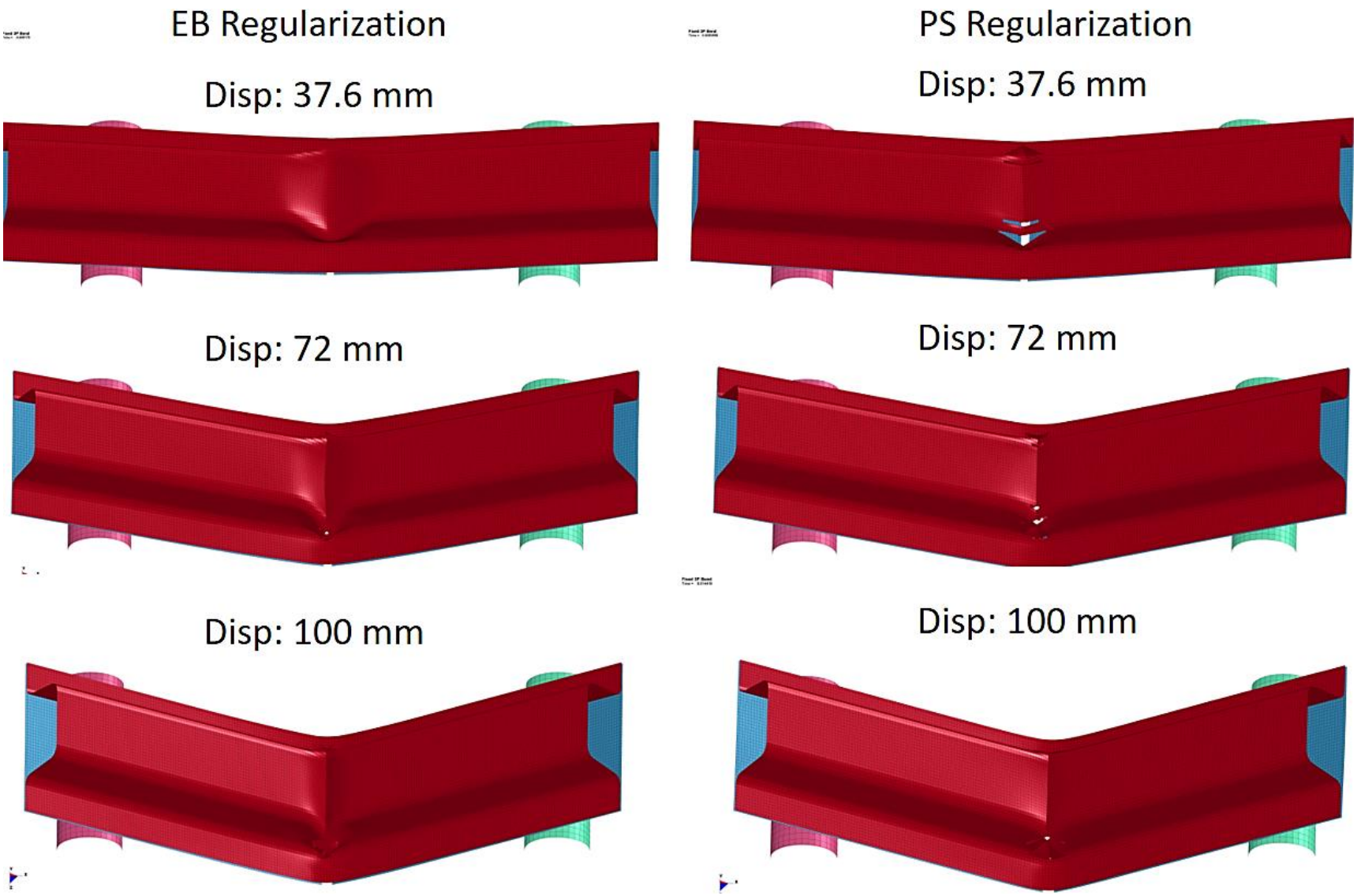

Figure 72: Dynamic material failure for models using different regularization curves at set impactor displacement for AA7075-T6

Based on the good agreement between the models and predictions using the EB regularization model, the balance of the models for the other materials were run using the EB scheme.

5.4.2 Quasi-Static Numerical Model – Comparison with Experiment

Figure 73 and Figure 75 show the predicted and measured force-displacement and absorbed energy curves for the AA7075 channels. The GISSMO failure model with the EB regularization curve was used and the same material parameters were adopted for the T6IPB channels. The peak forces for the numerical model was 20.4 kN which is comparable to the experimental value of 19.7 kN and 19.6 kN for T6 and T6IPB, respectively.

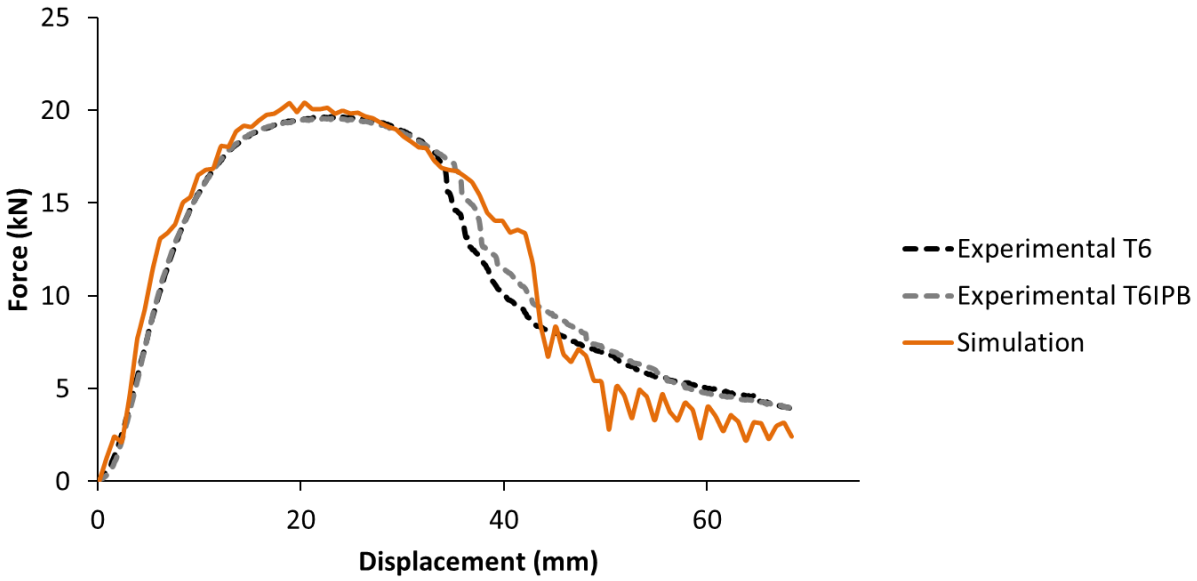

Figure 73: Quasi-static die quenched AA7075-T6 and -T6IPB force-displacement comparison

Figure 74 shows the extent of fracture in both the numerical model and experiments. The mesh plot shows the initiation of fracture at a indentor displacement of 23.6 mm, whereas the test specimen is shown after testing. The

element that first fractured was under a plane strain stress state and thus had the lowest fracture strain according to the GISSMO curve.

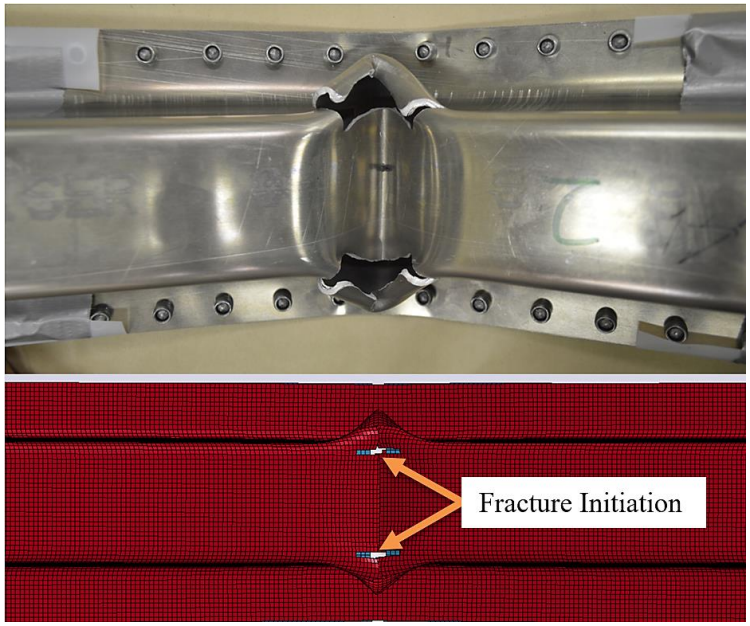

Figure 74: Visual comparison of the predicted and measured region of fracture for AA7075-T6

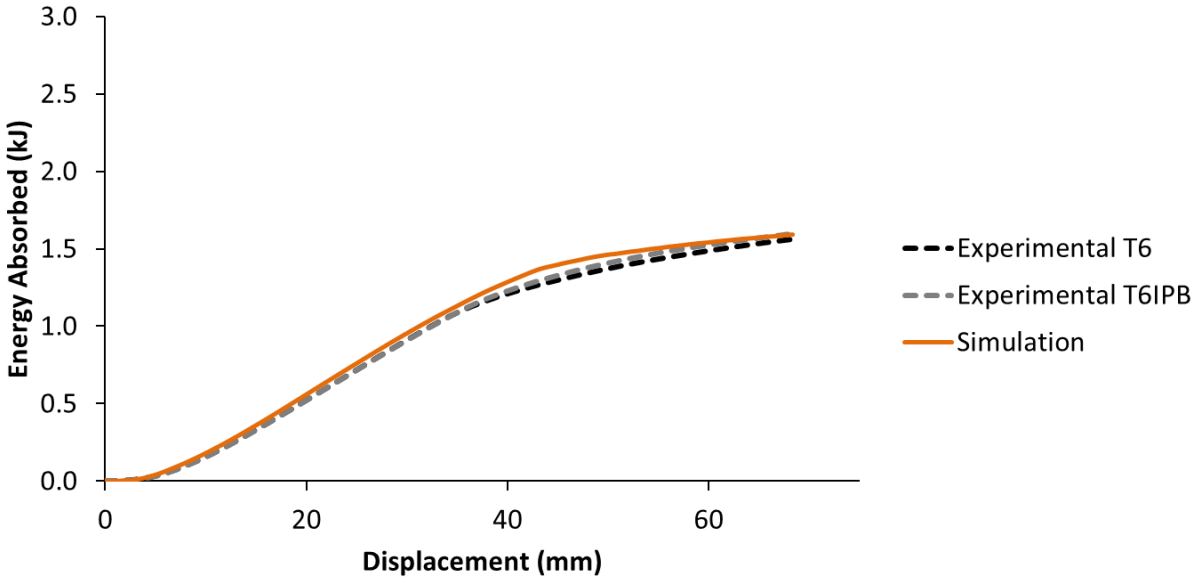

Figure 75: Quasi-static die quenched AA7075-T6 energy absorbed comparison

The AA7xxx material did not experience fracture during the experiment, but the simulation predicted the onset of failure. As a result, the simulation under predicted the force response and absorbed energy of the beam as shown in Figure 76 and Figure 77, respectively. The material model did over-estimate the strength of AA7xxx by predicting a peak force of 19.4 kN and the T76 and T6IPB had a peak force of 17.9 kN and 16.8 kN respectively.

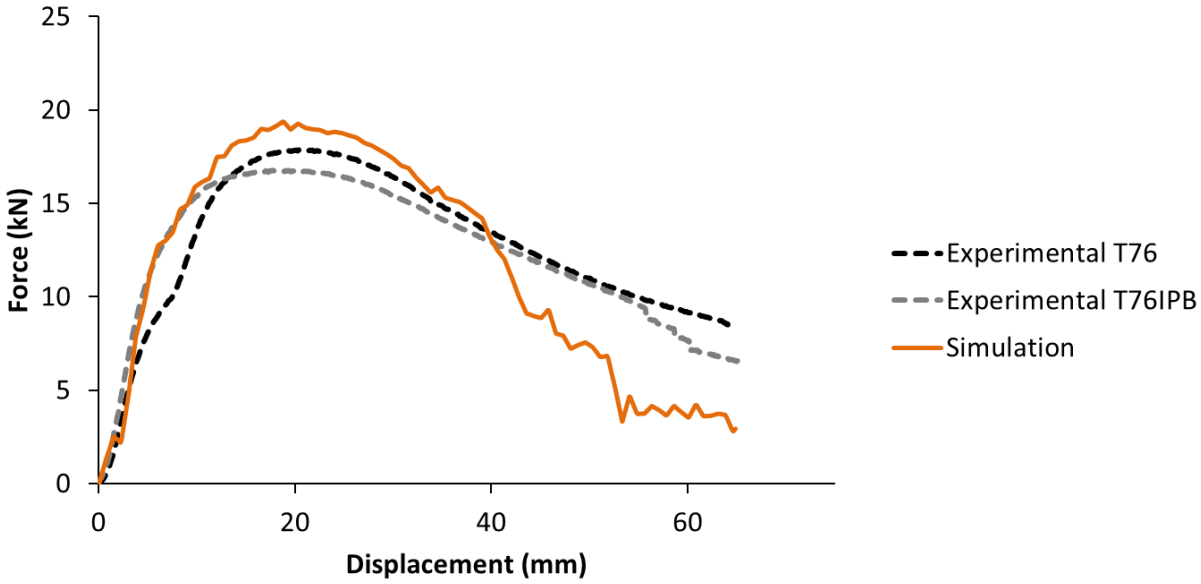

Figure 76: Quasi-static die quenched AA7xxx-T76 force displacement comparison

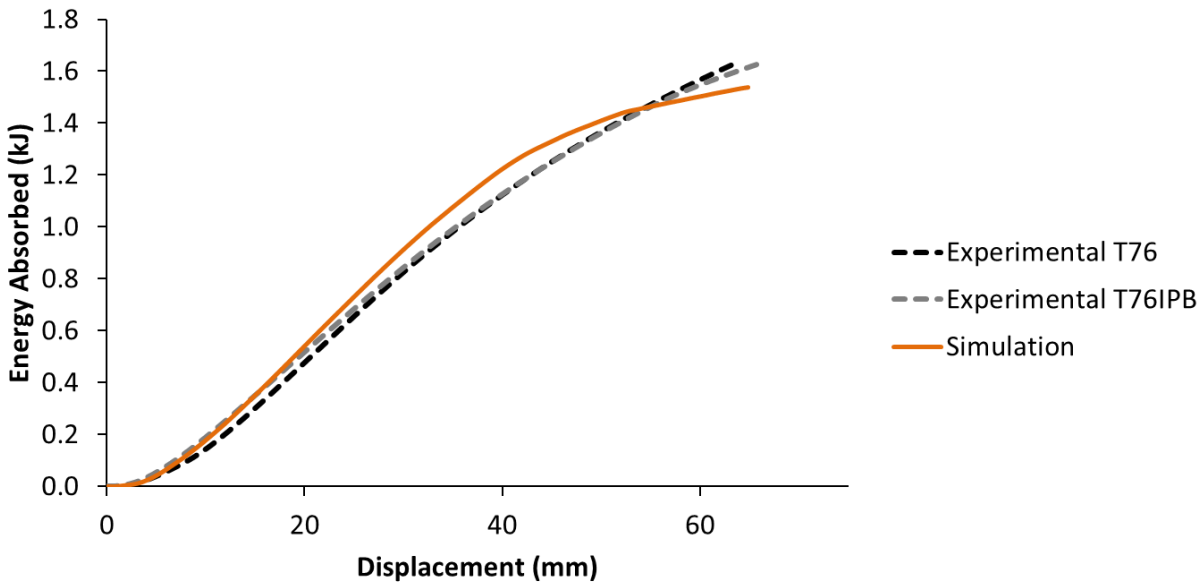

Figure 77 Quasi-static die quenched AA7xxx-T76 energy absorbed comparison

Figure 78 shows the extent of fracture in both the numerical model and experiments. The mesh plot shows the initiation of fracture at a indentor displacement of 40.2 mm, whereas the test specimen is shown after testing.

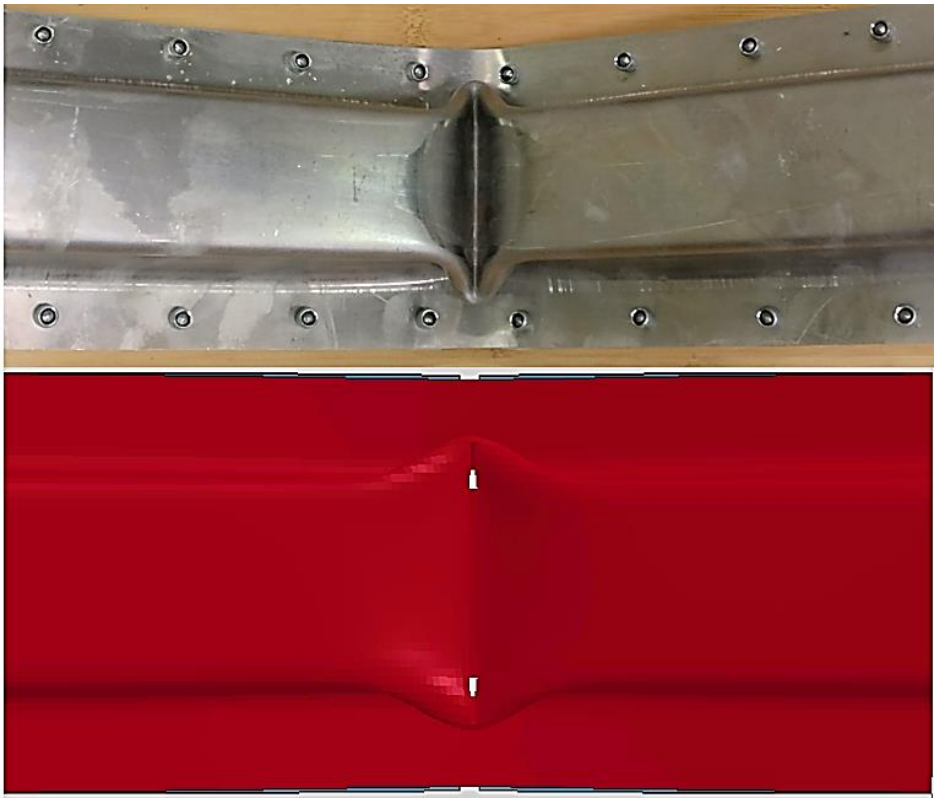

Figure 78: Visual comparison of the predicted and measured region of fracture for AA7xxx-T76

5.4.3 Dynamic Numerical Model Comparison

All dynamic comparisons between experiment and simulations used the GISSMO model with the EB regularization curve. Figure 79 shows that the AA7075 material model was able to capture the peak load response accurately for both T6 and T6IPB, while the absorbed energy results are shown in Figure 80.

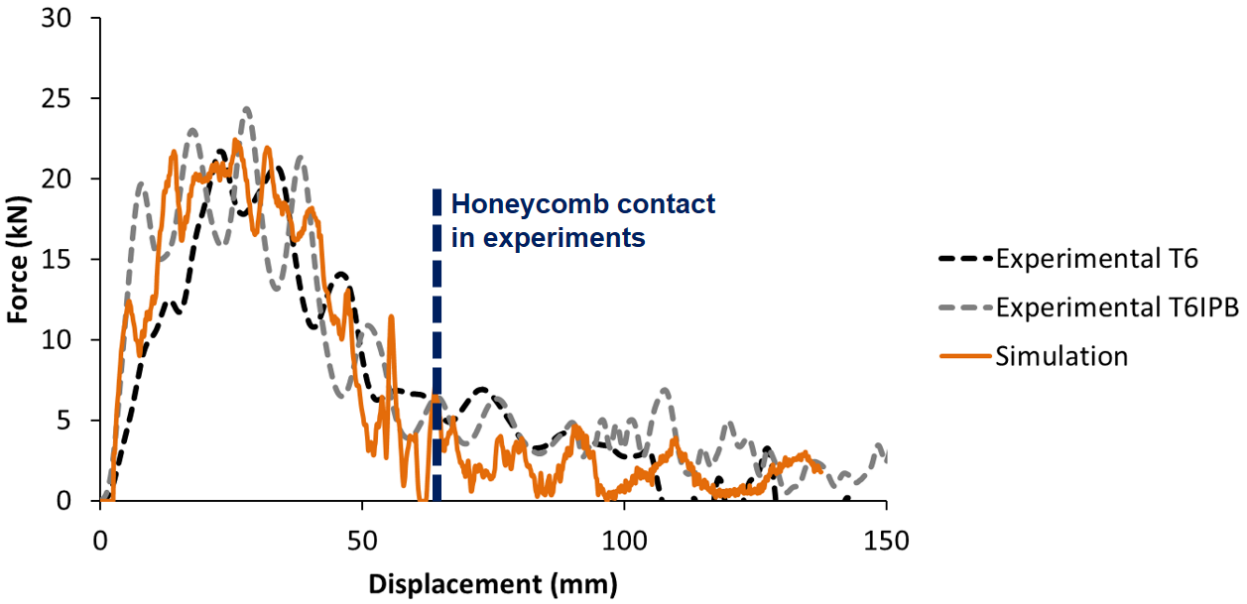

Figure 79: Dynamic die quenched AA7075-T6 force-displacement comparison

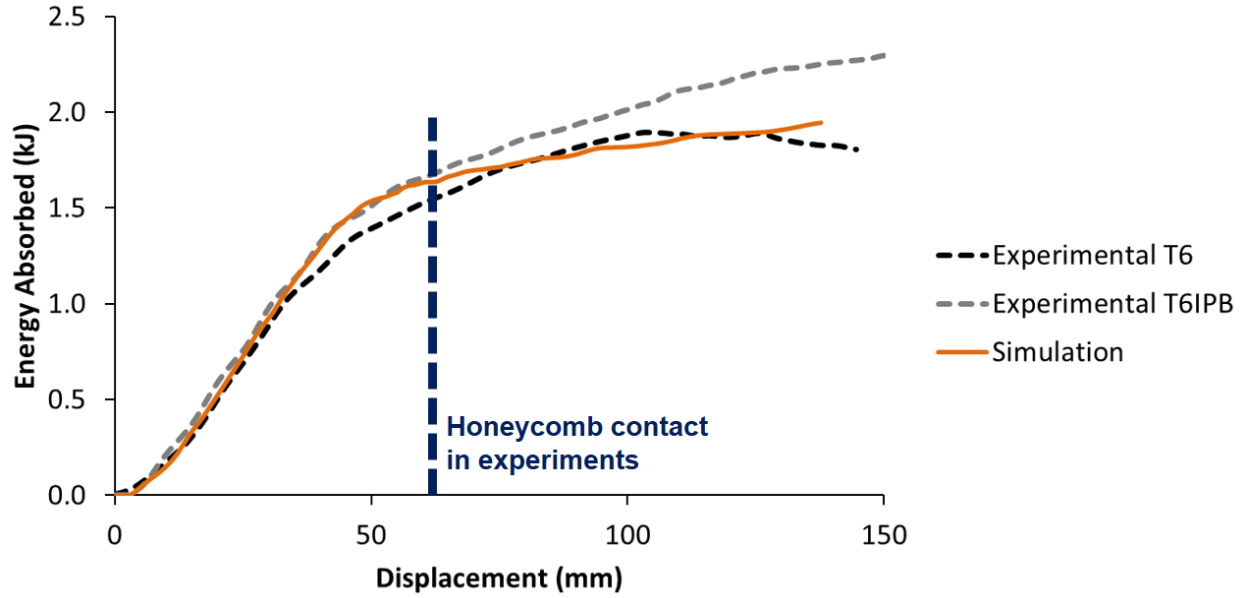

Figure 80: Dynamic die quenched AA7075-T6 energy absorbed comparison

Figure 81 shows that the AA7xxx material model was able to capture the dynamic peak load response accurately for both T76 and T76IPB. Figure 82 shows the absorbed energy curve for the corresponding experiments and numerical

models. The slope of the simulation curve is similar to both experimental results, further showing the degree of correlation.

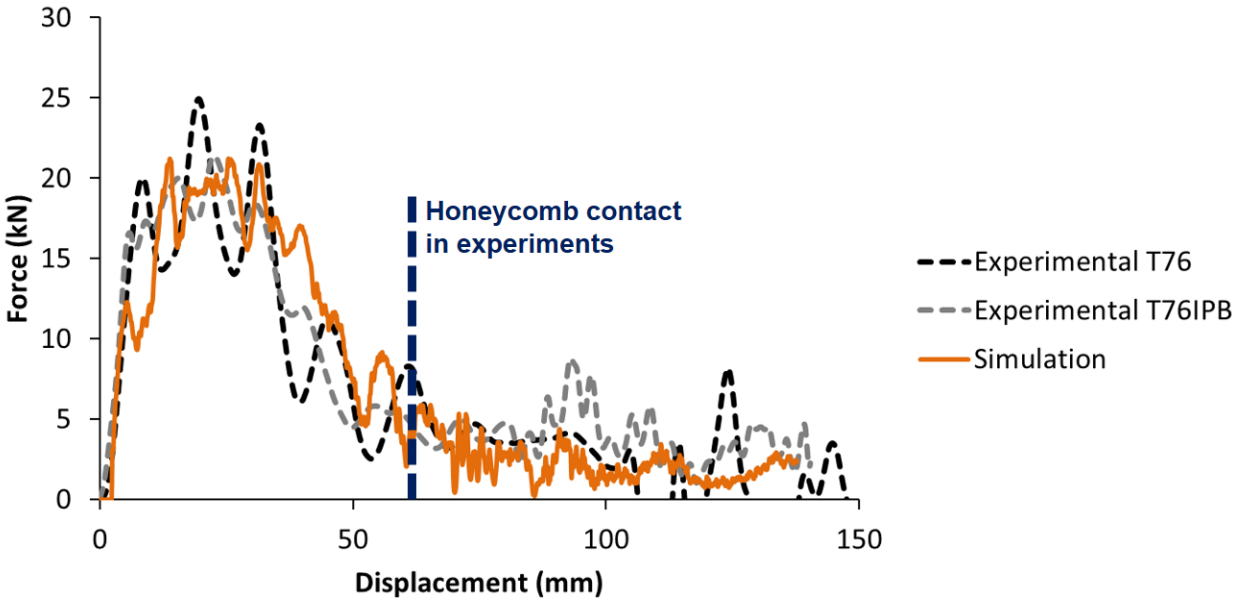

Figure 81: Dynamic die quenchedAA7xxx-T76 force-displacement comparison

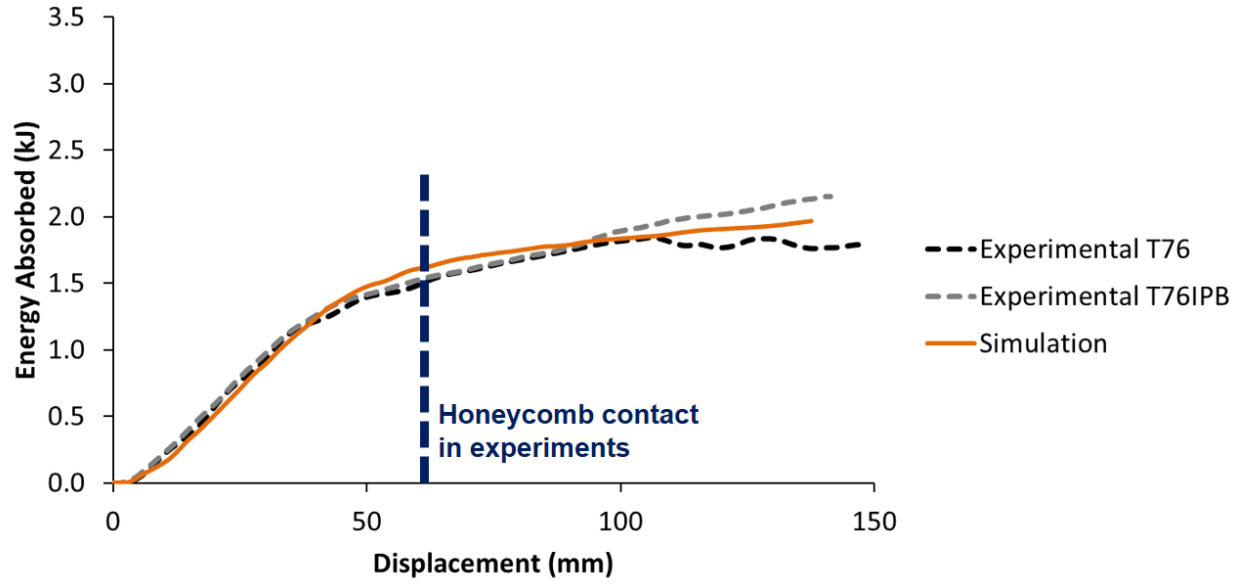

Figure 82: Dynamic die quenched AA7xxx-T6 energy absorption comparison

5.5 Discussion

A summary of the peak force and absorbed energy for all of the warm formed beams subjected to quasi-static, three-point bend testing is shown in Figure 83 and Figure 84, respectively. The ranking of peak loads follows the strength ranking between the alloys (Table 5), with AA7075 showing the highest peak loads and AA6013 the lowest. The absorbed energy trends were similar except in cases where significant cracking occurred, as in the non-isothermal AA7075 case which has a lower total energy absorption. In general, the warm forming processes with the lower thermal exposure resulted in the least loss in strength (*e.g.* the 232°C non-isothermal (cold tooling) case resulted in the highest final peak load). In addition, beams which were formed at a lower isothermal temperature exhibited higher peak loads and energy absorbed compared to the higher forming temperature.

The UA process resulted in a strength that was slightly lower than the other cases. It can be speculated that optimization of the starting temper could be done to balance the potential formability gain associated with a lower starting temper against a higher final strength (and corrosion resistance). It can be seen in UA data that the thermal exposure from paint bake cycle is crucial to strengthening the beam by advancing the aging process. From the comparison between the UA beams, UA beams that did not undergo the paint bake cycle were still under aged when tested.

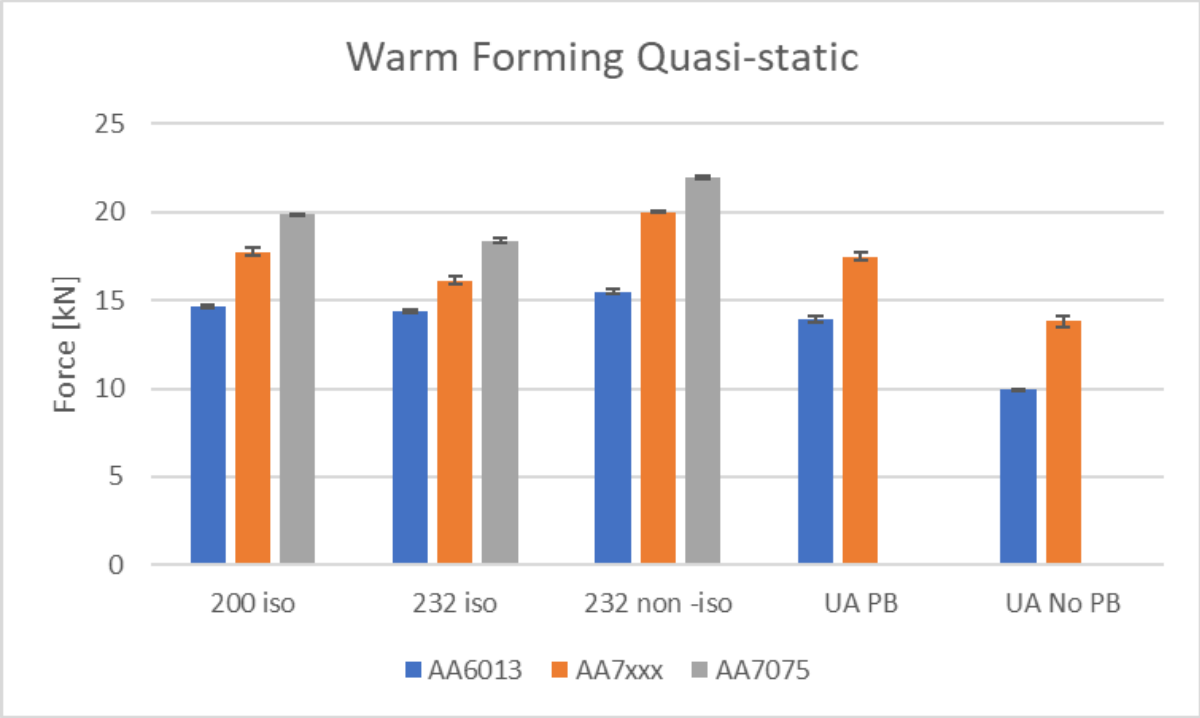

Figure 83: Measured peak force for all beams subjected to the warm forming processing route. Bars indicate average values, while scatter bars are indicated.

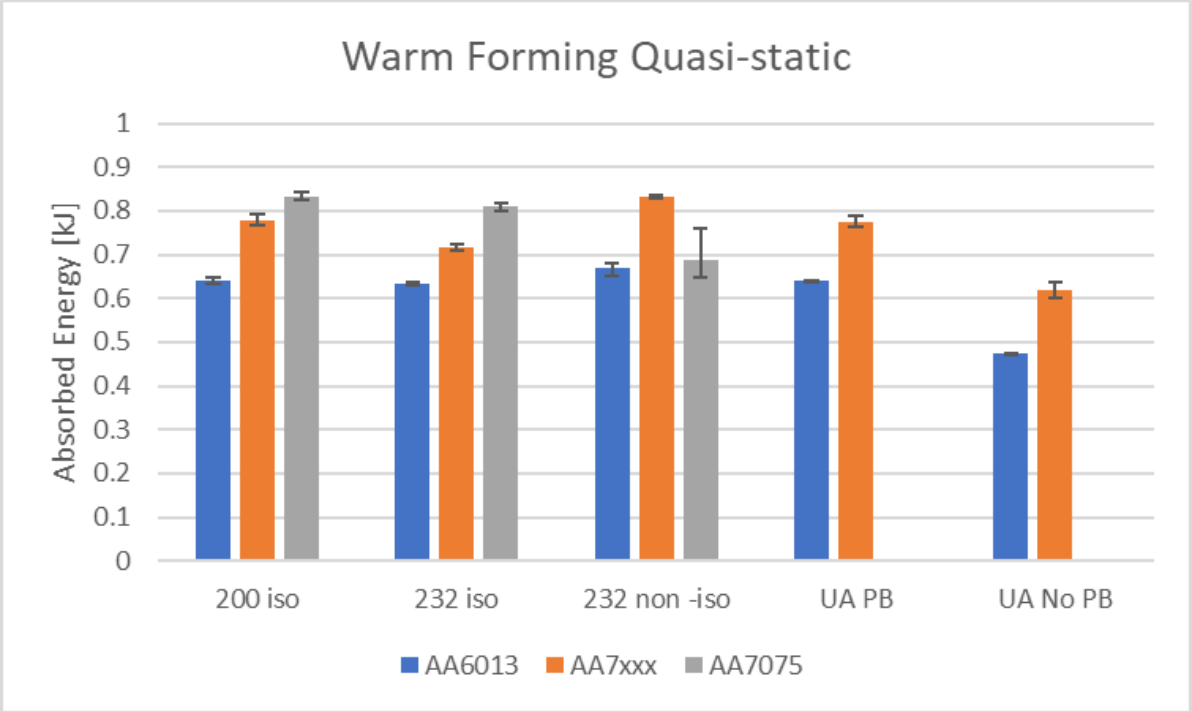

Figure 84: Measured absorbed energy for all beams subjected to the warm forming processing route at a punch displacement of 60 mm

A summary of the peak force and absorbed energy for all the die quenched conditions subjected to quasi-static three-point bend testing is shown in Figure 85 and Figure 86, respectively. In general, the AA7075 peak loads were slightly higher than the AA7xxx values, reflecting the slight difference in material strength (recall that the AA7xxx was tested in a T76 target temper for enhanced corrosion resistance). The IPB tempers, with their shorter aging requirements, exhibited similar performance to their T6 or T76 counterparts.

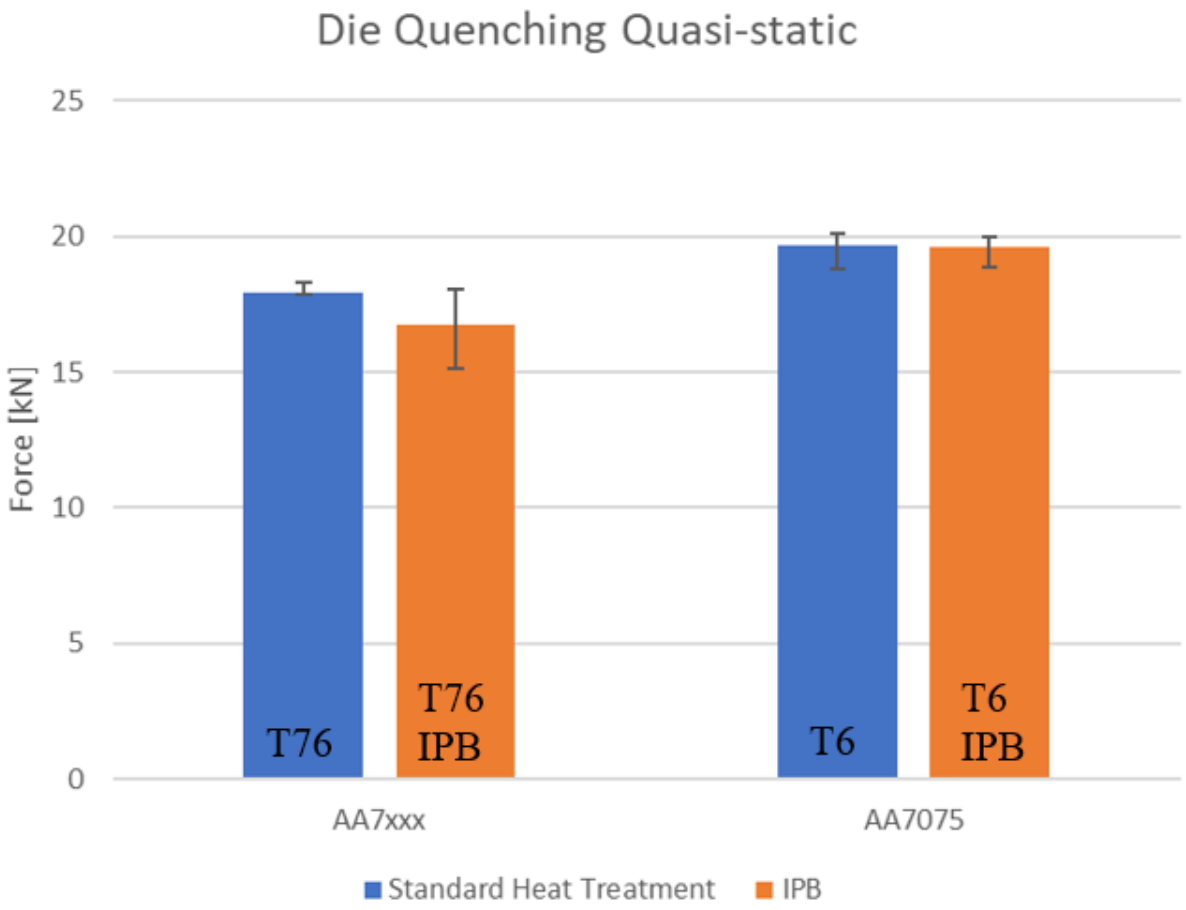

Figure 85: Peak force of all beams subjected to the die quench processing route

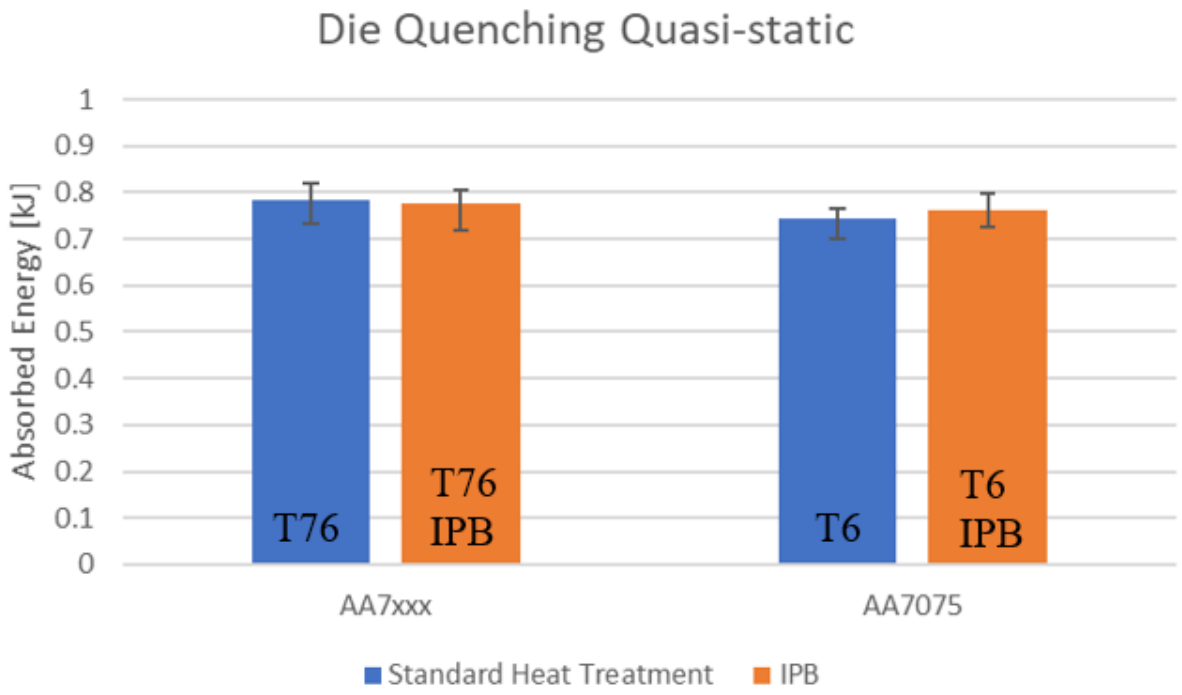

Figure 86: Absorbed energy for all beams subjected to the die quench processing route at a punch displacement of 60 mm

A summary of the peak force and absorbed energy for all the die quenched beams subjected to dynamic three-point bend test is shown in Figure 87 and Figure 88, respectively. The absorbed energies between the standard T6 [42] or T76 [68] heat treatments and the IPB heat treatments are very comparable and further supports that they are at similar levels of aging.

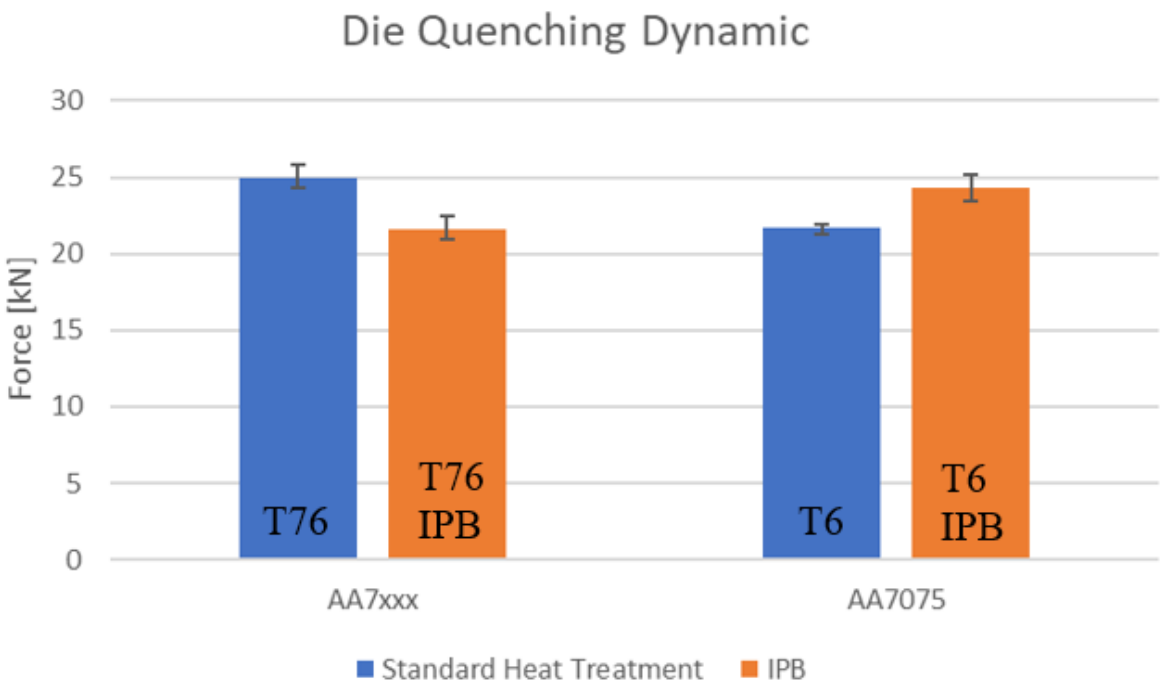

Figure 87: Peak force for the die quenched beams subjected to dynamic three-point bend loading

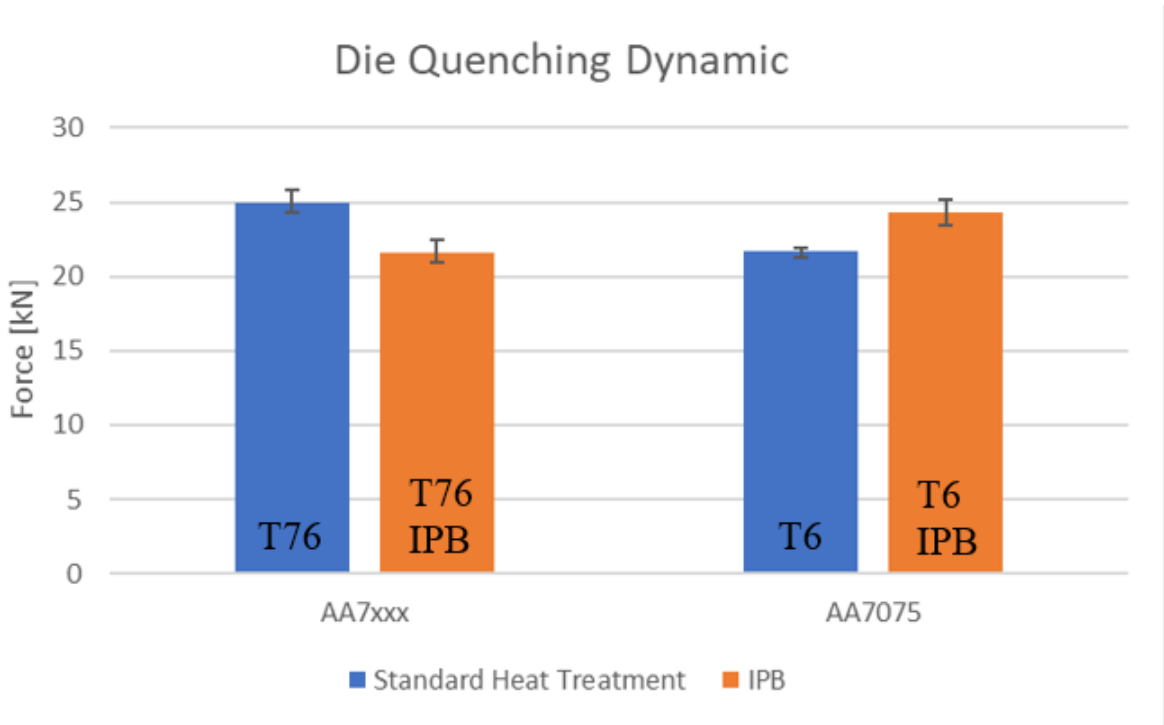

Figure 88: Absorbed energy for the die quenched beams subjected to dynamic three-point bend loading at a sled displacement of 60 mm

The peak loads and absorbed energy under quasi-static loading of all AA7xxx beams (warm formed and die quenched) are compared in Figure 89 and Figure 90, respectively, while corresponding comparisons are shown for the AA7075 beams in Figure 91and Figure 92. In general, all non-isothermally formed beams out-performed the die quenched beams in terms of peak force. In addition, the non-isothermally formed AA7xxx beam was also capable of absorbing the most energy compared to the same material subjected to any other processing route.

The plots show that the material degradation from the 200°C isothermal warm forming route was not significant and the overall strength and energy absorption are comparable to the die quenched beams for AA7xxx. The 200°C isothermal warm forming improved the energy absorption for the AA7075 beams, which was attributed to the increase in ductility that minimized the amount of cracking as seen in Figure 61.

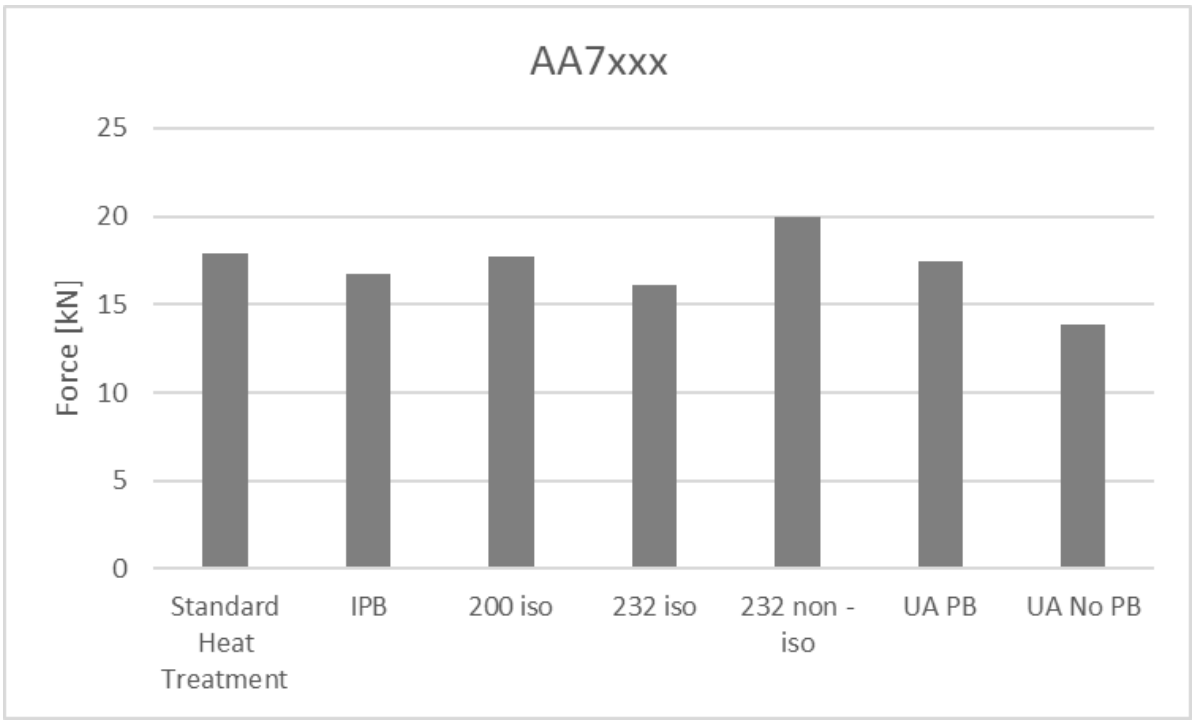

Figure 89: Peak force comparison between warm forming and die quenching for AA7xxx

Figure 90: Energy absorbed comparison between warm forming and die quenching for AA7xxx

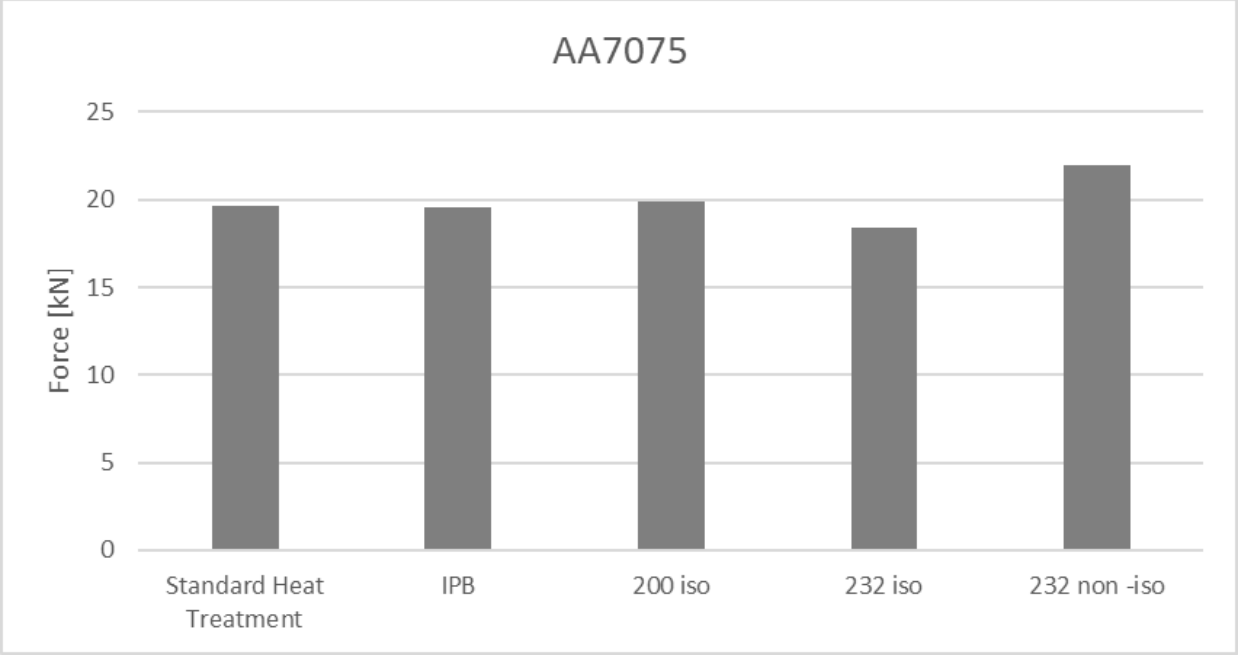

Figure 91: Peak force comparison between warm forming and die quenching for AA7075

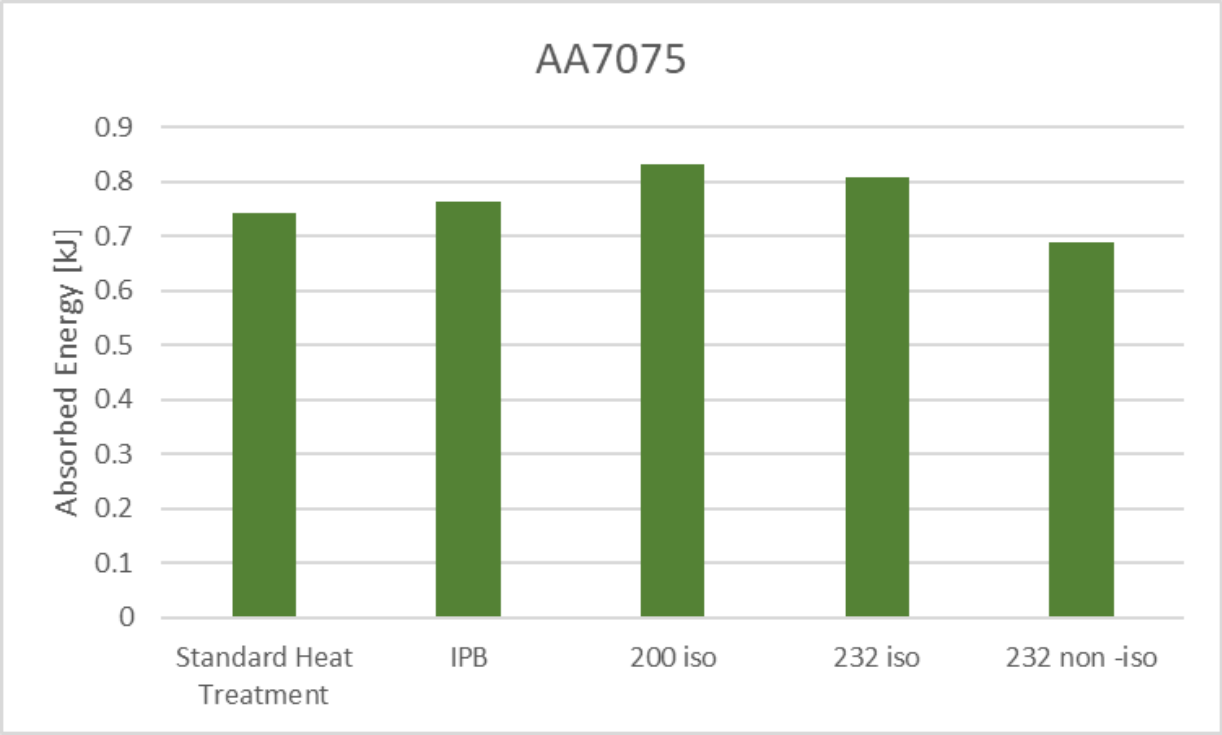

Figure 92: Energy absorbed comparison between warm forming and die quenching for AA7075

From this work, it has been demonstrated that die quenching and warm forming can increase the formability of precipitation hardened aluminum without severely compromising the overall strength. Experimental results show that the heat treatment schedule for a die quenched aluminum part to reach peak age can be reduced by 70-75% using the IPB aging schedules due to Omer [124]. Experiments also show that warm forming under-aged blanks and followed by aging during paint bake allowed the part to reach a near-peak temper. Leveraging the industrial automotive paint bake cycle to achieve higher strength can streamline an industrial process and reduce manufacturing time. These approaches to traditional elevated temperature forming processes reduce processing time while still maintaining the strength of the material.

6 CONCLUSIONS AND RECOMMENDATIONS

6.1 Conclusions

The following conclusions are drawn from this research:

1) conventional warm forming lubricants such as Fuchs are not suitable for direct application onto the blank for die quench forming because of its low flash point. Fuchs resulted in a significant amount of galling on the blanks and left residual material (pick-up) on the die. PTFE spray was the most suitable lubricant tested with no scoring/galling on the test article and left minimal pick-up on the tooling;
2) the under aged AA6013 and AA7xxx blanks subjected to warm forming followed by the paint bake cycle reached a final strength comparable to the conventional warm forming process. Channels formed using this process had similar peak force and absorbed energy compared to components formed with a T6 or T76 starting point;
3) all three materials that were non-isothermally warm formed at 232°C had higher peak loads in structural testing compared to beams that were isothermally warm formed at the same temperature. The AA6013 non-isothermally formed parts had 6.1% higher peak strength than the corresponding isothermally formed parts. This difference was 15.9% and 18.3% for the AA7075 and AA7xxx channels, respectively;
4) the interrupted paint bake (IPB) heat treatment to reach the T6 and T76 tempers for AA7075 and AA7xxx, respectively, had almost identical mechanical properties as the standard T6 and T76 conditions; and

5) the adopted GISSMO failure model with regularization improved the predictions of the structural models, capturing the onset of cracking in the higher strength beams.

6.2 Recommendations

In future work, the following recommendation should be considered to improve on the work that was described in this thesis:

1) incorporate a more complex geometry and structural tests for the lab-scaled component to more rigorously assess the formability and impact response of the materials;
2) investigate a lubricant for die quenching that is water soluble. This would allow the die quenching of aluminum to be more viable in a large-scale manufacturing process;
3) incorporate a material model that includes a temperature-dependent elastic modulus that can be used to assess the springback in the forming simulations;
4) utilize a Barlat YLD2000 material model for materials that underwent the warm forming process to allow the structural simulations to be executed with the warm formed material;
5) consider warm forming of alloys at a lower non-isothermal temperature to mitigate material aging during forming and possibly achieve higher final peak strength and absorbed energy;
6) consider optimizing the starting under-aged temper for warm forming to increase final strength while limiting loss of formability associated with lower initial tempers;

7) incorporate a stress-state dependent regularization curve to allow better prediction of material failure during structural numerical simulation.

7 Bibliography

[1] S. T. Anderson, I. W. H. Parry, J. M. Sallee, and C. Fischer, "Automobile fuel economy standards: Impacts, efficiency, and alternatives," *Rev. Environ. Econ. Policy*, vol. 5, no. 1, pp. 89–108, 2011.

[2] C. De Fur, A. Richardson, A. Roach, and G. Wiesent, "US and German Regulations of CO2 Emissions from Passenger Cars," in *Globalization and Public Policy: A European Perspective*, D. Audretsch, E. Lehmann, A. Richardson, and S. Vismara, Eds. Cham: Springer International Publishing, 2015, pp. 137–155.

[3] S. Pagerit, P. Sharer, and a. Rousseau, "Fuel economy sensitivity to vehicle mass for advanced vehicle powertrains," *Proc. SAE 2006 World Congr. Exhib.*, vol. 2006, no. 724, 2006.

[4] C. C. Chan, A. Bouscayrol, and K. Chen, "Electric, hybrid, and fuel-cell vehicles: Architectures and modeling," *IEEE Trans. Veh. Technol.*, vol. 59, no. 2, pp. 589–598, 2010.

[5] C. C. Chan, "The state of the art of electric, hybrid, and fuel cell vehicles," *Proc. IEEE*, vol. 95, no. 4, pp. 704–718, 2007.

[6] W. Hucho and G. Sovran, "Aerodynamics of Road Vehicles," *Annu. Rev. Fluid Mech.*, vol. 25, no. 1, pp. 485–537, 1993.

[7] T. P. Hutchinson and R. W. G. Anderson, "Vehicle mass as a determinant of fuel consumption and secondary safety performance: A comment," *Transp. Res. Part D Transp. Environ.*, vol. 15, no. 2, pp.

123–125, 2010.

[8] K. Fukuo, A. Fujimura, M. Saito, K. Tsunoda, and S. Takiguchi, “Development of the ultra-low-fuel-consumption hybrid car – INSIGHT,” *JSAE Rev.*, vol. 22, no. 1, pp. 95–103, 2001.

[9] R. Johri and Z. Filipi, “Low-Cost Pathway to Ultra Efficient City Car: Series Hydraulic Hybrid System with Optimized Supervisory Control,” *SAE Int. J. Engines*, vol. 2, no. 2, pp. 505–520, 2010.

[10] Y. Li, Z. Lin, A. Jiang, and G. Chen, “Use of high strength steel sheet for lightweight and crashworthy car body,” *Mater. Des.*, vol. 24, no. 3, pp. 177–182, 2003.

[11] H.-J. Kim, G. A. Keoleian, and S. J. Skerlos, “Economic Assessment of Greenhouse Gas Emissions Reduction by Vehicle Lightweighting Using Aluminum and High-Strength Steel,” *J. Ind. Ecol.*, vol. 15, no. 1, pp. 64–80, 2011.

[12] E. Ghassemieh, “Materials in Automotive Application , State of the Art and Prospects,” *New Trends Dev. Automot. Ind.*, pp. 365–394, 2011.

[13] G. S. Cole and A. M. Sherman, “Light weight materials for automotive applications,” *Mater. Charact.*, vol. 35, no. 1, pp. 3–9, 1995.

[14] K. J. Kim *et al.*, “Development of application technique of aluminum sandwich sheets for automotive hood,” *Int. J. Precis. Eng. Manuf.*, vol. 10, no. 4, pp. 71–75, 2009.

[15] C. Lungwitz, S. A. A, and L. Design, “Body development at Audi – innovation , quality and precision Automotive lightweight design –

triumph of an idea," pp. 1–14, 2017.

[16] S. Toros, F. Ozturk, and I. Kacar, "Review of warm forming of aluminum-magnesium alloys," *J. Mater. Process. Technol.*, vol. 207, no. 1–3, pp. 1–12, 2008.

[17] H. WANG, Y. LUO, P. FRIEDMAN, M. CHEN, and L. GAO, "Warm forming behavior of high strength aluminum alloy AA7075," *Trans. Nonferrous Met. Soc. China*, vol. 22, no. 1, pp. 1–7, 2012.

[18] N. Sotirov, M. Kumar, P. Simon, and C. Chimani, "Study of forming strategies for ultrahigh-strength aluminium panels in the semi-hot (warm) forming temperature range," no. September, 2012.

[19] S. Mahabunphachai and M. Ko, "Investigations on forming of aluminum 5052 and 6061 sheet alloys at warm temperatures," *Mater. Des.*, vol. 31, no. 5, pp. 2422–2434, 2010.

[20] J. T. Lee, "Simulation and Experimental Investigation of Hot Forming of Aluminum Alloy AA5182 with Application toward Warm Forming," 2012.

[21] M. Kumar, N. Sotirov, and C. M. Chimani, "Investigations on warm forming of AW-7020-T6 alloy sheet," *J. Mater. Process. Technol.*, vol. 214, no. 8, pp. 1769–1776, 2014.

[22] M. Ghosh, A. Miroux, R. J. Werkhoven, P. J. Bolt, and L. A. I. Kestens, "Warm deep-drawing and post drawing analysis of two Al-Mg-Si alloys," *J. Mater. Process. Technol.*, vol. 214, no. 4, pp. 756–766, 2014.

[23] R. Neugebauer, T. Altan, M. Geiger, M. Kleiner, and A. Sterzing, "Sheet

metal forming at elevated temperatures," *CIRP Ann. - Manuf. Technol.*, vol. 55, no. 2, pp. 793–816, 2006.

[24] M. Kleiner, M. Geiger, and a. Klaus, "Manufacturing of Lightweight Components by Metal Forming," *CIRP Ann. - Manuf. Technol.*, vol. 52, no. 2, pp. 521–542, 2003.

[25] S. Mahabunphachai and M. Ko??, "Investigations on forming of aluminum 5052 and 6061 sheet alloys at warm temperatures," *Mater. Des.*, vol. 31, no. 5, pp. 2422–2434, 2010.

[26] X. Fan, Z. He, S. Yuan, and K. Zheng, "Experimental investigation on hot forming-quenching integrated process of 6A02 aluminum alloy sheet," *Mater. Sci. Eng. A*, vol. 573, pp. 154–160, 2013.

[27] X. Fan, Z. He, S. Yuan, and P. Lin, "Investigation on strengthening of 6A02 aluminum alloy sheet in hot forming-quenching integrated process with warm forming-dies," *Mater. Sci. Eng. A*, vol. 587, pp. 221–227, 2013.

[28] L. K. Berg, D. Schryvers, and L. R. Wallenberg, "GP-ZONES IN Al – Zn – Mg ALLOYS AND THEIR ROLE IN ARTIFICIAL AGING," *Acta Mater.*, vol. 4, pp. 3443–3451, 2001.

[29] A. Bardelcik, A. Bouhier, and M. J. Worswick, "Three Point Bend Performance of Solutionized, Die Quenched and Heat Treated AA7075 Beam Members," *Alum. Alloy. 2014 - ICAA14*, vol. 794, pp. 431–436, 2014.

[30] R. Clark *et al.*, "On the correlation of mechanical and physical

properties of 7075-T6 Al alloy," *Eng. Fail. Anal.*, vol. 12, no. 4, pp. 520–526, 2005.

[31] R. S. Kaneko, L. Bakow, and E. W. Lee, "Aluminum alloy 6013 sheet for new U.S. Navy aircraft," *Jom*, vol. 42, no. 5, pp. 16–18, 1990.

[32] K. Dehghani, A. Nekahi, and M. A. M. Mirzaie, "Optimizing the bake hardening behavior of Al7075 using response surface methodology," *Mater. Des.*, vol. 31, no. 4, pp. 1768–1775, 2010.

[33] R. Clark *et al.*, "On the correlation of mechanical and physical properties of 7075-T6 Al alloy," *Eng. Fail. Anal.*, vol. 12, no. 4, pp. 520–526, 2005.

[34] R. S. Long, E. Boettcher, and D. Crawford, "Current and Future Uses of Aluminum in the Automotive Industry," *JOM*.

[35] Y. F. Lung, M. C. Lin, H. C. Lin, and K. M. Lin, "The stamping behavior of an early-aged 6061 aluminum alloy," *Mater. Des.*, vol. 32, no. 8–9, pp. 4369–4375, 2011.

[36] P. F. Bariani, S. Bruschi, A. Ghiotti, and F. Michieletto, "Hot stamping of AA5083 aluminium alloy sheets," *CIRP Ann. - Manuf. Technol.*, vol. 62, no. 1, pp. 251–254, 2013.

[37] L. Wang, M. Strangwood, D. Balint, J. Lin, and T. A. Dean, "Formability and failure mechanisms of AA2024 under hot forming conditions," *Mater. Sci. Eng. A*, vol. 528, no. 6, pp. 2648–2656, 2011.

[38] S. J. Yuan, X. B. Fan, and Z. Bin He, "Hot forming-quenching integrated process with cold-hot dies for 2A12 aluminum alloy sheet," *Procedia*

Eng., vol. 81, no. October, pp. 1780–1785, 2014.

[39] O. El Fakir, L. Wang, D. Balint, J. P. Dear, J. Lin, and T. A. Dean, "Numerical study of the solution heat treatment, forming, and in-die quenching (HFQ) process on AA5754," *Int. J. Mach. Tools Manuf.*, vol. 87, pp. 39–48, 2014.

[40] M. S. Mohamed, A. D. Foster, J. Lin, D. S. Balint, and T. A. Dean, "Investigation of deformation and failure features in hot stamping of AA6082: Experimentation and modelling," *Int. J. Mach. Tools Manuf.*, vol. 53, no. 1, pp. 27–38, 2012.

[41] J. Gilbert Kaufman, *Introduction to Aluminum Alloys and Tempers*. Materials Park: ASM International, 2000.

[42] J. C. Benedyk, "International Temper Designation Systems for Wrought Aluminum Alloys," *Light Met. Age*, vol. 67, no. October, pp. 3–6, 2009.

[43] A. K. Gupta, D. J. Lloyd, and S. A. Court, "Precipitation Hardening Processes in an Al–0.4%Mg–1.3%Si–0.25%Fe Aluminum Alloy," *Mater. Sci. Eng. A*, vol. 301, no. 2, pp. 140–146, 2001.

[44] G. Sha and A. Cerezo, "Early-stage precipitation in Al-Zn-Mg-Cu alloy (7050)," *Acta Mater.*, vol. 52, no. 15, pp. 4503–4516, 2004.

[45] S. D. Dumolt, D. E. Laughlin, and J. C. Williams, "Formation of a modified beta" phase in aluminium alloy 6061," *Scr. Metall.*, vol. 18, no. 150, pp. 1347–1350, 1984.

[46] M. Vivas, P. Lours, C. Levaillant, A. Couret, M. J. Casanove, and A. Coujou, "Transmission electron microscopy study of precipitate

morphology and precipitate overcoming processes in aluminum alloy 6056 T6," *Mater. Sci. Eng. A*, vol. 234–236, no. 0, pp. 664–667, 1997.

[47] J. D. Bryant, "The effects of preaging treatments on aging kinetics and mechanical properties in AA6111 aluminum autobody sheet," *Metall. Mater. Trans. A*, vol. 30, no. 8, pp. 1999–2006, 1999.

[48] A. Perovic, D. D. Perovic, G. C. Weatherly, and D. J. Lloyd, "Precipitation in aluminum alloys AA6111 and AA6016," *Scr. Mater.*, vol. 41, no. 7, pp. 703–708, 1999.

[49] W. F. Miao and D. E. Laughlin, "Precipitation hardening in aluminum alloy 6022," *Scr. Mater.*, vol. 40, no. 7, pp. 873–878, 1999.

[50] K. Omer, L. ten Kortenaar, C. Butcher, M. Worswick, S. Malcolm, and D. Detwiler, "Testing of a hot stamped axial crush member with tailored properties – Experiments and models," *Int. J. Impact Eng.*, vol. 103, pp. 12–28, 2017.

[51] M. Merklein and T. Svec, "Hot stamping: Manufacturing functional optimized components," *Prod. Eng.*, vol. 7, no. 2–3, pp. 141–151, 2013.

[52] Z. W. Xing, J. Bao, and Y. Y. Yang, "Numerical simulation of hot stamping of quenchable boron steel," *Mater. Sci. Eng. A*, vol. 499, no. 1–2, pp. 28–31, 2009.

[53] H. Karbasian and A. E. Tekkaya, "A review on hot stamping," *J. Mater. Process. Technol.*, vol. 210, no. 15, pp. 2103–2118, 2010.

[54] M. Merklein, J. Lechler, and T. Stoehr, "Investigations on the thermal behavior of ultra high strength boron manganese steels within hot

stamping," *Int. J. Mater. Form.*, vol. 2, no. SUPPL. 1, pp. 259–262, 2009.

[55] A. Bardelcik, M. J. Worswick, S. Winkler, and M. A. Wells, "A strain rate sensitive constitutive model for quenched boron steel with tailored properties," *Int. J. Impact Eng.*, vol. 50, pp. 49–62, 2012.

[56] A. Bardelcik, C. P. Salisbury, S. Winkler, M. A. Wells, and M. J. Worswick, "Effect of cooling rate on the high strain rate properties of boron steel," *Int. J. Impact Eng.*, vol. 37, no. 6, pp. 694–702, 2010.

[57] J. Lin, T. A. Dean, R. Garret, and A. D. Foster, "Process for forming aluminium alloy sheet components," WO2008059242, 2008.

[58] J. Zhou, B. Wang, J. Lin, and L. Fu, "Optimization of an aluminum alloy anti-collision side beam hot stamping process using a multi-objective genetic algorithm," *Arch. Civ. Mech. Eng.*, vol. 13, no. 3, pp. 401–411, 2013.

[59] F. Ozturk, A. Sisman, S. Toros, S. Kilic, and R. C. Picu, "Influence of aging treatment on mechanical properties of 6061 aluminum alloy," *Mater. Des.*, vol. 31, no. 2, pp. 972–975, 2010.

[60] F. Ozturk, E. Esener, S. Toros, and C. R. Picu, "Effects of aging parameters on formability of 6061-O alloy," *Mater. Des.*, vol. 31, no. 10, pp. 4847–4852, 2010.

[61] J. Jabra *et al.*, "The Effect of Thermal Exposure on the Mechanical Properties of 2099-T6 Die Forgings, 2099-T83 Extrusions, 7075-T7651 Plate, 7085-T7452 Die Forgings, 7085-T7651 Plate, and 2397-T87 Plate Aluminum Alloys," *J. Mater. Eng. Perform.*, vol. 15, no. October, pp.

601–607, 2006.

[62] T. Oppenheim *et al.*, “On the correlation of mechanical and physical properties of 6061-T6 and 7249-T76 aluminum alloys,” *Eng. Fail. Anal.*, vol. 14, no. 1, pp. 218–225, 2007.

[63] M. Erdoğan, A. Erçetin, and İ. Güneş, “Investigation of Mechanical Properties of Natural Aged Aa 7075 Aluminum Alloy,” no. October, pp. 15–17, 2014.

[64] S. Esmaeili and D. J. Lloyd, “Modeling of precipitation hardening in pre-aged AlMgSi(Cu) alloys,” *Acta Mater.*, vol. 53, no. 20, pp. 5257–5271, 2005.

[65] S. Esmaeili, D. J. Lloyd, and W. J. Poole, “Modeling of precipitation hardening for the naturally aged Al-Mg-Si-Cu alloy AA6111,” *Acta Mater.*, vol. 51, no. 12, pp. 3467–3481, 2003.

[66] P. Li, B. Xiong, Y. Zhang, and Z. Li, “Temperature variation and solution treatment of high strength AA7050,” *Trans. Nonferrous Met. Soc. China*, vol. 22, no. 3, pp. 546–554, 2012.

[67] a. Deschamps and Y. Bréchet, “Influence of quench and heating rates on the ageing response of an Al–Zn–Mg–(Zr) alloy,” *Mater. Sci. Eng. A*, vol. 251, no. 1–2, pp. 200–207, 1998.

[68] ASM International, *ASM International. Metals Handbook. 10th ed.* 1990.

[69] S. Kurukuri, A. H. van den Boogaard, A. Miroux, and B. Holmedal, “Warm forming simulation of Al-Mg sheet,” *J. Mater. Process. Technol.*, vol. 209, no. 15–16, pp. 5636–5645, 2009.

[70] N. Sotirov, P. Simon, D. Uffelmann, C. Melzer, and F. I. Gmbh, “Feasibility of high-strength 7xxx aluminium sheet components through warm forming,” *Metall.*

[71] N. Sotirov, P. Simon, C. Chimani, D. Uffelmann, and C. Melzer, “Warm Deep Drawability of Peak-Aged 7075 Aluminium Sheet Alloy,” *Key Eng. Mater.*, vol. 504–506, no. 0, pp. 955–960, 2012.

[72] A. H. Van Den Boogaard, — Pieter, J. Bolt, R. J. Werkhoven, and A. H. V. U. Nl, “Modeling of AlMg Sheet Forming at Elevated Temperatures,” *Int. J. Form. Process.*, vol. 4, no. 3, pp. 4–361, 2001.

[73] F. Shehata, M. J. Painter, and R. Pearce, “Warm forming of aluminium/magnesium alloy sheet,” *J. Mech. Work. Technol.*, vol. 2, no. 3, pp. 279–290, 1978.

[74] G. Palumbo and L. Tricarico, “Numerical and experimental investigations on the Warm Deep Drawing process of circular aluminum alloy specimens,” *J. Mater. Process. Technol.*, vol. 184, no. 1–3, pp. 115–123, 2007.

[75] M. M. H. Takuda, K. Mori, I. Masuda, Y. Abe, ““Finite element simulation of warm deep drawing of aluminium alloy sheet when accounting for heat conduction,” *J. Mater. Process. Technol.*, vol. 120, pp. 412–418, 2002.

[76] and J. D. D. Finch, S. Wilson, “Deep-drawing aluminum alloys at elevated temperatures,” *ASMTransactions*, vol. 36, pp. 254–289, 1946.

[77] H. Laurent *et al.*, “Mechanical Behaviour and Springback Study of an

Aluminium Alloy in Warm Forming Conditions," *Int. Sch. Res. Netw.*, vol. 2011, no. 2, pp. 1–9, 2011.

[78] J. Mckinley, "Warm Forming of Aluminum Brazing Sheet Experiments and Numerical Simulations," 2010.

[79] L. R. Morris and R. A. George, "Warm Forming High-Strength Aluminum Automotive Parts," in *SAE Technical Paper*, 1977.

[80] N. Abedrabbo, F. Pourboghrat, and J. Carsley, "Forming of AA5182-O and AA5754-O at elevated temperatures using coupled thermo-mechanical finite element models," *Int. J. Plast.*, vol. 23, no. 5, pp. 841–875, 2007.

[81] E. J. F. R. Caron, K. J. Daun, and M. a. Wells, "Experimental heat transfer coefficient measurements during hot forming die quenching of boron steel at high temperatures," *Int. J. Heat Mass Transf.*, vol. 71, pp. 396–404, 2014.

[82] E. Caron, K. J. Daun, and M. A. Wells, "Experimental characterization of heat transfer coefficients during hot forming die quenching of boron steel," *Metall. Mater. Trans. B Process Metall. Mater. Process. Sci.*, vol. 44, no. 2, pp. 332–343, 2013.

[83] Z. Malinowski, J. G. Lenard, and M. E. Davies, "A study of the heat-transfer coefficient as a function of temperature and pressure," *J. Mater. Process. Tech.*, vol. 41, no. 2, pp. 125–142, 1994.

[84] Y. T. Keum, B. Y. Ghoo, and R. H. Wagoner, "3-dimensional finite element analysis of nonisothermal forming processes for non-ferrous

sheets," *Simul. Mater. Process. Theory, Methods Appl.*, p. 813, 2001.

[85] N. Abedrabbo, F. Pourboghrat, and J. Carsley, "Forming of aluminum alloys at elevated temperatures - Part 1: Material characterization," *Int. J. Plast.*, vol. 22, no. 2, pp. 314–341, 2006.

[86] F. Barlat *et al.*, "Yield function development for aluminum alloy sheets," *J. Mech. Phys. Solids*, vol. 45, no. 11–12, pp. 1727–1763, 1997.

[87] F. Barlat *et al.*, "Plane stress yield function for aluminum alloy sheets—part 1: theory," *Int. J. Plast.*, vol. 19, no. 9, pp. 1297–1319, 2003.

[88] A. P. Karafillis and M. C. Boyce, "A general anisotropic yield criterion using bounds and a transformation weighting tensor," *J. Mech. Phys. Solids*, vol. 41, no. 12, pp. 1859–1886, 1993.

[89] P. Oscar and R. L. Eduardo, "Impact Performance of Advanced High Strength Steel Thin-Walled Columns," *Engineering*, vol. II, no. 0, pp. 2–7, 2008.

[90] T. Mukai, K. Higashi, and S. Tanimura, "Influence of the magnesium concentration on the relationship between fracture mechanism and strain-rate in high-purity Al-Mg alloys," *Mater. Sci. Eng. A*, vol. 176, no. 1–2, pp. 181–189, 1994.

[91] T. Rahmaan, A. Bardelcik, J. Imbert, C. Butcher, and M. J. Worswick, "Effect of strain rate on flow stress and anisotropy of DP600, TRIP780, and AA5182-O sheet metal alloys," *Int. J. Impact Eng.*, vol. 88, pp. 72–90, 2016.

[92] W. Moćko, J. A. Rodríguez-Martínez, Z. L. Kowalewski, and A. Rusinek,

"Compressive viscoplastic response of 6082-T6 and 7075-T6 aluminium alloys under wide range of strain rate at room temperature: Experiments and modelling," *Strain*, vol. 48, no. 6, pp. 498–509, 2012.

[93] G. R. Johnson and W. H. Cook, "A constitutive model and data for metals subjected to large strains, high strain rates and high temperatures," *7th International Symposium on Ballistics*. pp. 541–547, 1983.

[94] F. J. Zerilli and R. W. Armstrong, "Dislocation-mechanics-based constitutive relations for material dynamics calculations," *J. Appl. Phys.*, vol. 61, no. 5, pp. 1816–1825, 1987.

[95] E. Voce, "The relationship between stress and strain for homogeneous deformations," *J. Inst. Met.*, vol. 74, pp. 537–562, 1948.

[96] J. E. Hockett and O. D. Sherby, "Large strain deformation of polycrystalline metals at low homologous temperatures," *J. Mech. Phys. Solids*, vol. 23, no. 2, pp. 87–98, 1975.

[97] Z. Chen and C. Butcher, *Micromechanics Modelling of Ductile Fracture*, vol. 195. 2013.

[98] J. Lemaitre, "A Continuous Damage Mechanics Model for Ductile Fracture," *J. Eng. Mater. Tech.*, vol. 107, no. 1, pp. 83–89, 1985.

[99] L. ten Kortenaar, "Failure Characterization of Hot Formed Boron Steels with Tailored Mechanical Properties," University of Waterloo, 2016.

[100] K. Omer, "Development and Testing of a Hot Stamped Axial Crush Member with Tailored Properties," University of Waterloo, 2014.

[101] A. Zhumagulov, “Crashworthiness and Material Characterization of Multi-Cellular AA6063 Extrusions,” University of Waterloo, 2017.

[102] F. Neukamm, M. Feucht, and A. Haufe, “Considering damage history in crashworthiness simulations,” *Ls-Dyna Anwenderforum*, 2009.

[103] Y. Bai and T. Wierzbicki, “A new model of metal plasticity and fracture with pressure and Lode dependence,” *Int. J. Plast.*, vol. 24, no. 6, pp. 1071–1096, 2008.

[104] M. Basaran, S. D. Wölkerling, M. Feucht, D. Weichert, and D. Ag, “An Extension of the GISSMO Damage Model Based on Lode Angle Dependence,” *LS-DYNA Anwenderforum.*, 2010.

[105] L. Hua, F. Meng, Y. Song, J. Liu, X. Qin, and L. Suo, “A constitutive model of 6111-T4 aluminum alloy sheet based on the warm tensile test,” *J. Mater. Eng. Perform.*, vol. 23, no. 3, pp. 1107–1113, 2014.

[106] D. Li and A. Ghosh, “Tensile deformation behavior of aluminum alloys at warm forming temperatures,” *Mater. Sci. Eng. A*, vol. 352, no. 1–2, pp. 279–286, 2003.

[107] J. S. Robinson, D. A. Tanner, C. E. Truman, A. M. Paradowska, and R. C. Wimpory, “The influence of quench sensitivity on residual stresses in the aluminium alloys 7010 and 7075,” *Mater. Charact.*, vol. 65, pp. 73–85, 2012.

[108] L. Sang-Yong, L. Jung-Hwan, and L. Young-Seon, “Characterization of Al 7075 alloys after cold working and heating in the semi-solid temperature range,” *J. Mater. Process. Technol.*, vol. 111, no. 1–3, pp.

42–47, 2001.

[109] M. R. Rokni, A. Zarei-Hanzaki, A. A. Roostaei, and A. Abolhasani, “Constitutive base analysis of a 7075 aluminum alloy during hot compression testing,” *Mater. Des.*, vol. 32, no. 10, pp. 4955–4960, 2011.

[110] K. Omer, S. Kim, C. Butcher, and M. Worswick, “Characterizing the Constitutive Properties of AA7075 for Hot Forming,” *Proc. Int. Deep Draw Res. Gr. Conf.*, 2017.

[111] ASTM Int., “Standard Test Methods for Tension Testing of Metallic Materials 1,” *Astm*, no. C, pp. 1–27, 2009.

[112] A. Ochsner and H. Altenbach, *Experimental and numerical investigation of advanced materials and structures*. 2013.

[113] ASM International, “Metals Handbook,” 10th ed., ASM International, 1990.

[114] The Aluminum Assosciation, *International Alloy Designations and Chemical Composition Limits for Wrought Aluminum and Wrought Aluminum Alloys*. 2009.

[115] L. Xiwu *et al.*, “Effect of aging treatment on properties and microstructure of an Al-7.5Zn-1.3Mg-1.4Cu-0.12Zr alloy,” *Mater. Sci. Forum*, vol. 638–642, pp. 273–278, 2010.

[116] U.S. Government Printing Office, “Heat Treatment of Aluminum Alloys,” 1991, p. MI L-H-6088G.

[117] G. B. Burger, A. K. Gupta, P. W. Jeffrey, and D. J. Lloyd, “Microstructural

control of aluminum sheet used in automotive applications," *Mater. Charact.*, vol. 35, no. 1, pp. 23–39, 1995.

[118] R. George, "Hot Forming of Boron Steels with Tailored Mechanical Properties Experiments and Numerical Simulations," University of Waterloo, 2011.

[119] K. Omer, "Personal Communication," University of Waterloo, 2017.

[120] P. Archambault, J. C. Chevrier, G. Beck, and J. Bouvaist, "A contribution to the optimization of the 7075 heat treatment," *Mater. Sci. Eng.*, vol. 43, no. 1, pp. 1–6, 1980.

[121] S. Chen, K. Chen, G. Peng, L. Jia, and P. Dong, "Effect of heat treatment on strength, exfoliation corrosion and electrochemical behavior of 7085 aluminum alloy," *Mater. Des.*, vol. 35, pp. 93–98, 2012.

[122] S. Chen, K. Chen, G. Peng, X. Chen, and Q. Ceng, "Effect of heat treatment on hot deformation behavior and microstructure evolution of 7085 aluminum alloy," *J. Alloys Compd.*, vol. 537, pp. 338–345, 2012.

[123] K. Omer, C. Butcher, and M. Worswick, "Calculation and Validation of Heat Transfer Coefficient for Warm Forming Operations," *Esaform*, pp. 2–7, 2017.

[124] K. Omer, "Forthcoming Paper," 2017.

[125] J. R. Cahoon, W. H. Broughton, and A. R. Kutzak, "The determination of yield strength from hardness measurements," *Metall. Trans.*, vol. 2, no. 7, pp. 1979–1983, 1971.

[126] S. DiCecco, “Personal Communication,” University of Waterloo, 2017.

[127] J. Noder, “Characterization and Simulation of Warm Forming of 6xxx and 7xxx Series Aluminum Alloys by,” 2017.

[128] M. DiCiano, “Personal Communication,” University of Waterloo, 2017.

[129] Y. Prajogo, “Hot Stamping of a Boron Steel Side Impact Beam with Tailored Flange Properties - Experiments and Numerical Simulations,” p. 125, 2015.

[130] Plascore CrushLite, “Plascore CrushLite.” p. 2, 2012.

[131] Livermore Software Technology Corporation (LSTC), *LS-DYNA Keyword User’s Manual - Volume I*, vol. I. 2015.

[132] F. Beer, J. DeWolf, and D. Maxurek, *Mechanics of Materials*, 6th ed. New York, N.Y.: McGraw Hill, 2012.

[133] J. Y. Touloukian, *Thermal Properties of Matter*. IFI/Plenum, 1970.

[134] W. F. Gale and T. C. Totemeir, *Smithells Metals Reference Book*, 8th Editio. Butterworth-Heinemann, 2003.

[135] Livermore Software Technology Corporation (LSTC), *LS-DYNA Keyword User’s Manual - Volume II Material Models*, vol. II. 2015.

[136] F. Barlat and K. Lian, “Plastic behavior and stretchability of sheet metals. Part I: A yield function for orthotropic sheets under plane stress conditions,” *Int. J. Plast.*, vol. 5, no. 1, pp. 51–66, 1989.

[137] A. B. Shapiro, “Using LS-Dyna for Hot Stamping,” no. 2, 2009.

[138] T. L. Bergman, A. S. Lavigne, F. P. Incropera, and D. P. Dewitt, *Fundamentals of Heat and Mass Transfer*. 2011.

[139] M. T. Rahmaan, “Personal Communication,” University of Waterloo, 2017.

[140] M. T. Rahmaan, “Forthcoming Doctoral Theses,” University of Waterloo.

[141] AWS D8.9M-2002, “Standard test method AWS D8.9M (Recommended Practices for Test Methods for Evaluating the Resistance Spot Welding Behavior of Automotive Sheet Steel Materials),” *Am. Weld. Soc.*, 2012.

[142] Q. Majid Pouranvari, Pirooz Marashi, “Failure Behaviour of Resistance Spot Welded Low Carbon Steel in Tensile-Shear and Coach-Peel Tests,” *Eng. Metall. Sci. Serbia Ames*, vol. 15, pp. 145–157, 2009.

Appendix A

The normal and shear failure strength of the rivets were characterized using the lap shear test [141] and cross tension test [141]. In addition to these test, coach peel tests [142] were also conducted. The load *versus* displacement response can be seen in Figure 99. The test specimen and fixture for the lap shear test and cross tension tests can be seen in Figure 99, Figure 95 and Figure 97 respectively. The 5 kN rivet dimensions are shown in Table 11.

Figure 93: Lap shear specimen with 5 kN rivet

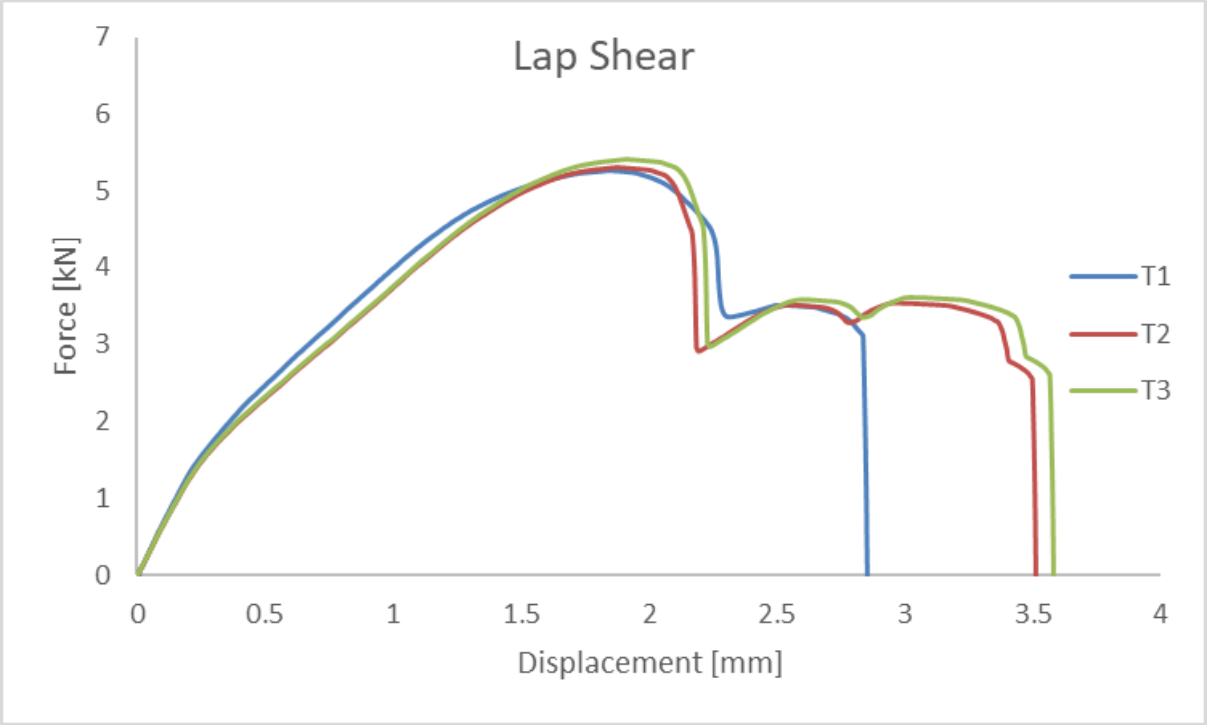

Figure 94: Load *versus* displacement response of 5 kN rivets for lap shear test

Figure 95: Cross tension fixture and specimen with 5 kN rivet

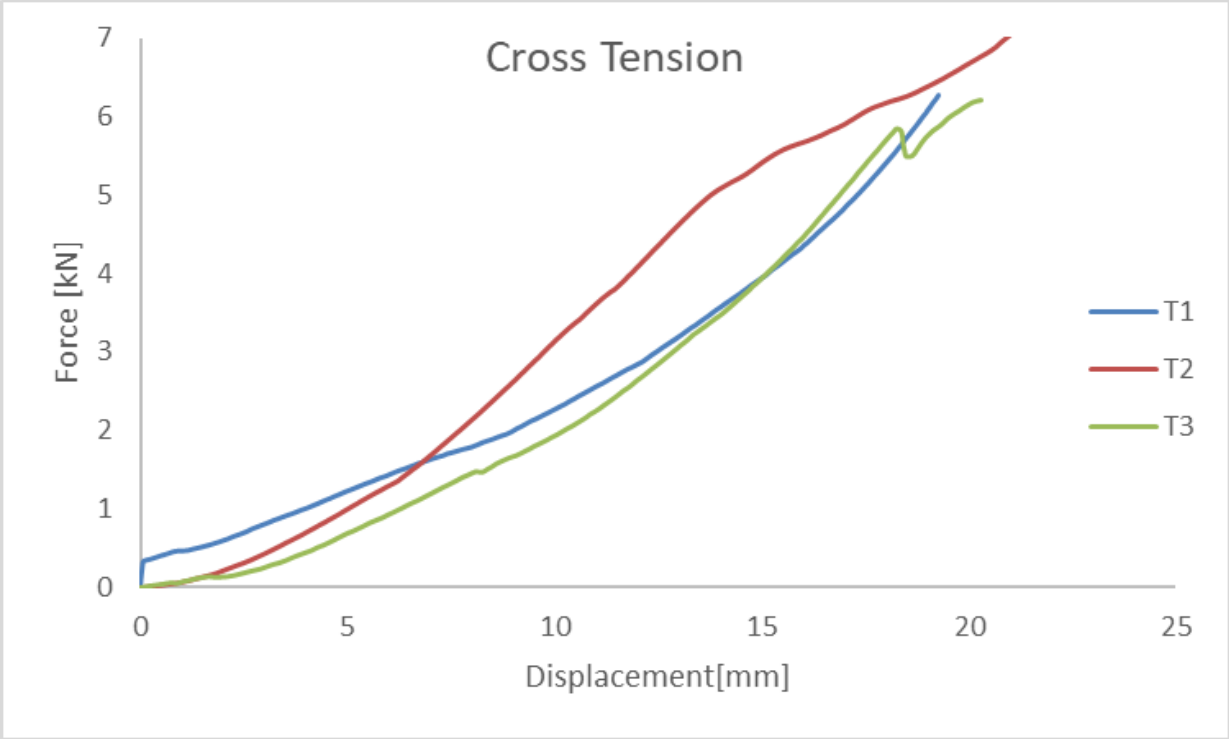

Figure 96: Load *versus* displacement response of 5 kN rivets for cross tension test

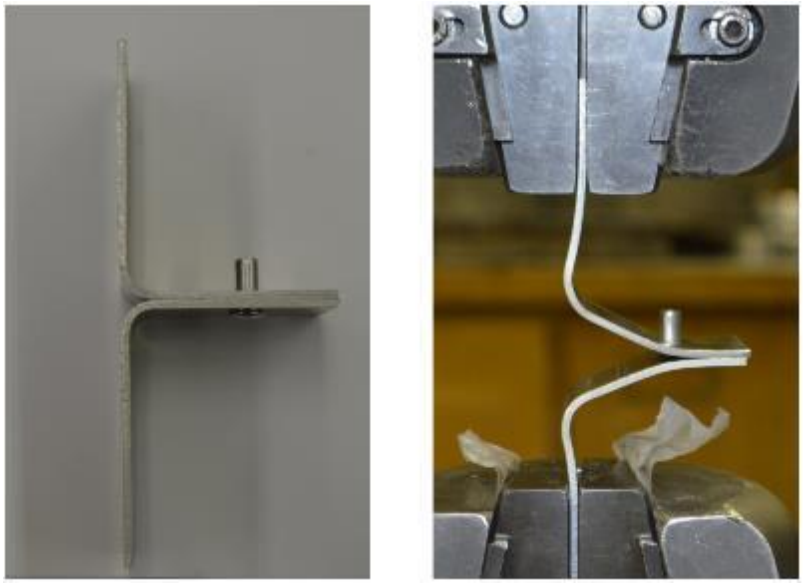

Figure 97: Coach peel test specimen with 5 kN rivet

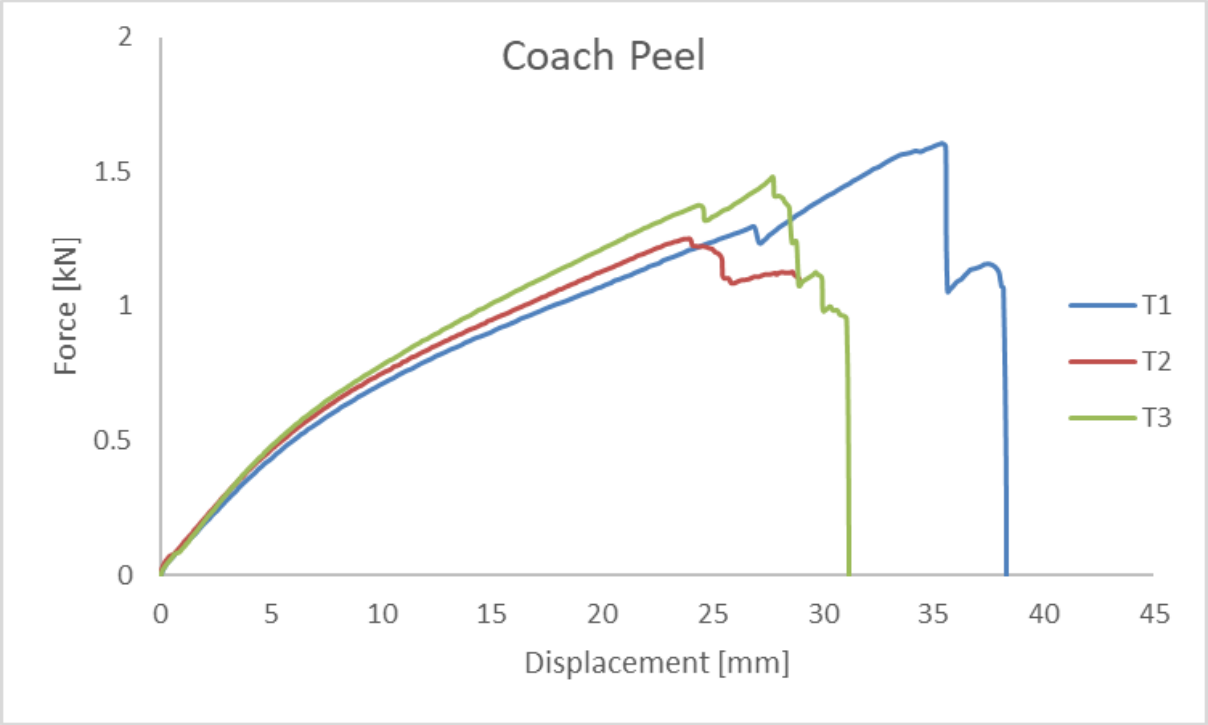

Figure 98: Load *versus* displacement response of 5 kN rivets for coach peel test

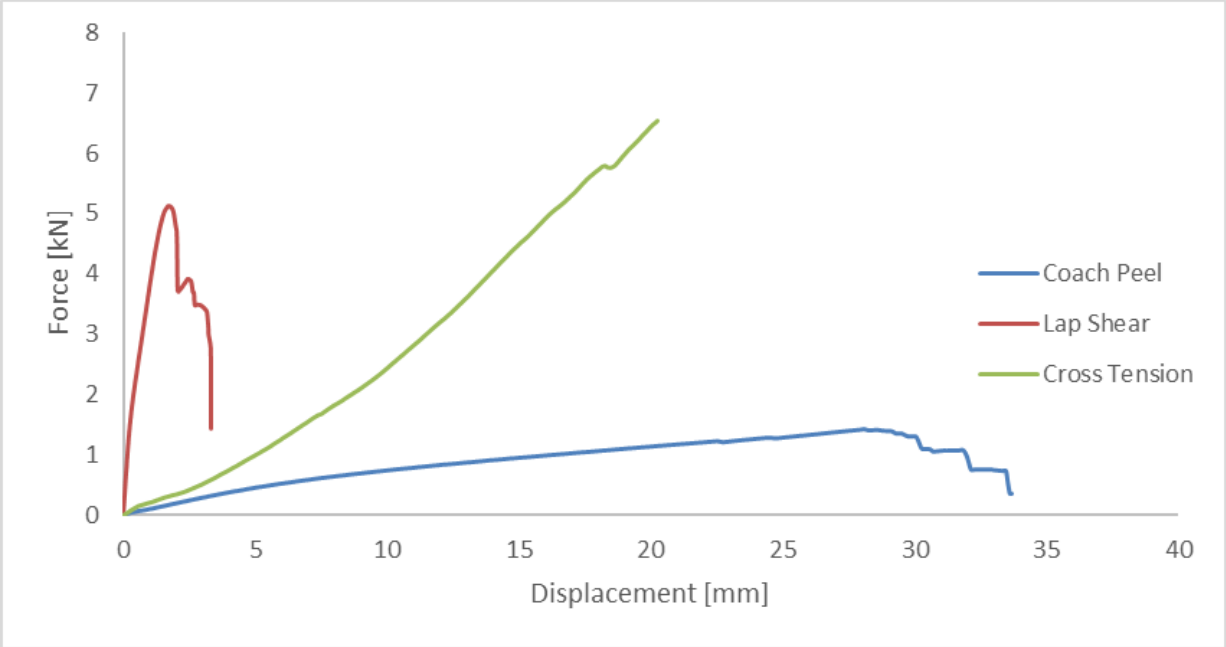

Figure 99: Typical load *versus* displacement response for all three rivet strength tests

Appendix B

This appendix presents the measured force-displacement and absorbed energy-displacement histories for all of the quasi-static and dynamic three-point bend experiments. All repeat experiments are shown in the figures, below.

B.1 Quasi-static Warm Formed Three-Point Bend Test Data

AA6013

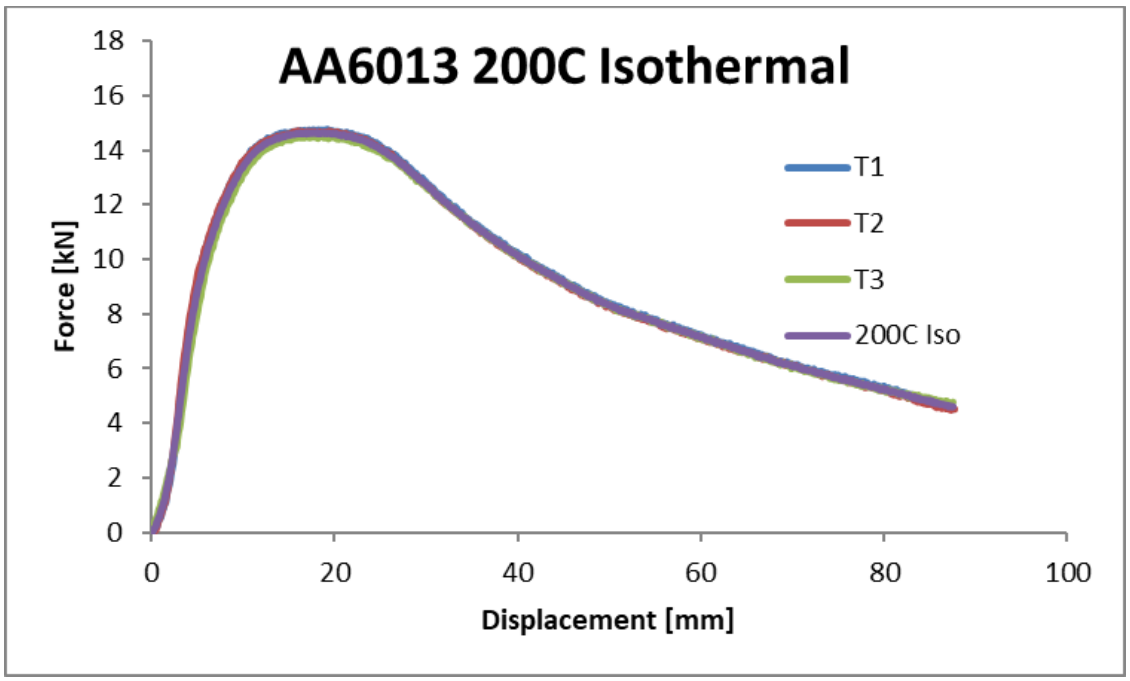

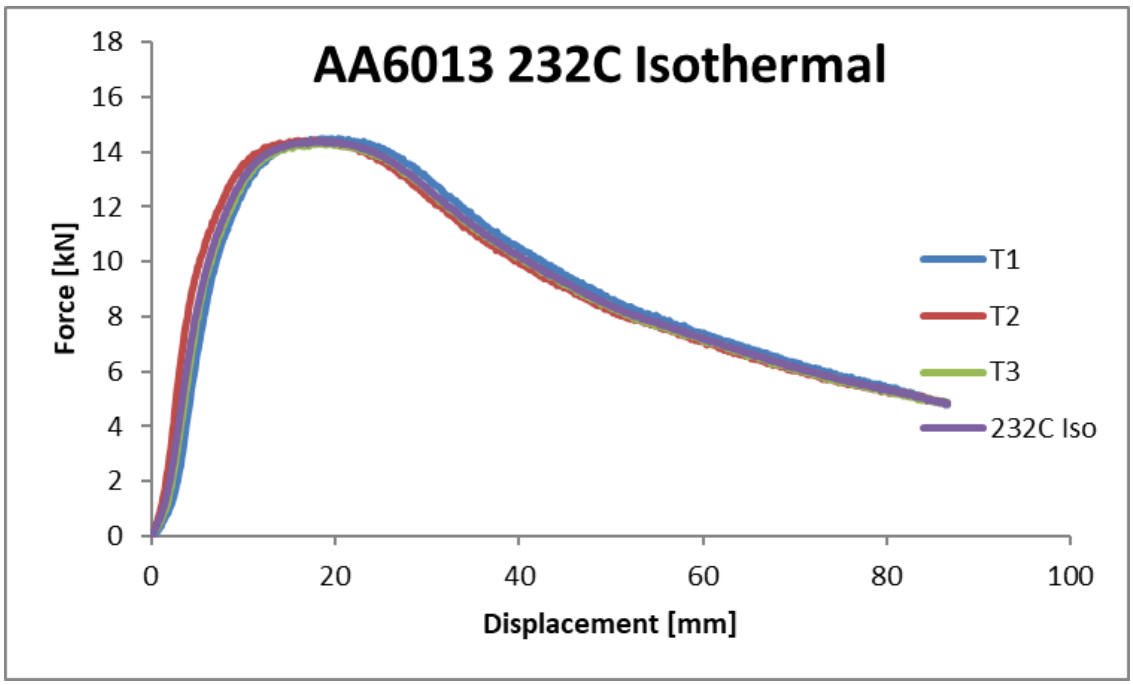
AA6013 232C Isothermal
Force [kN]
Displacement [mm]
T1
T2
T3
232C Iso

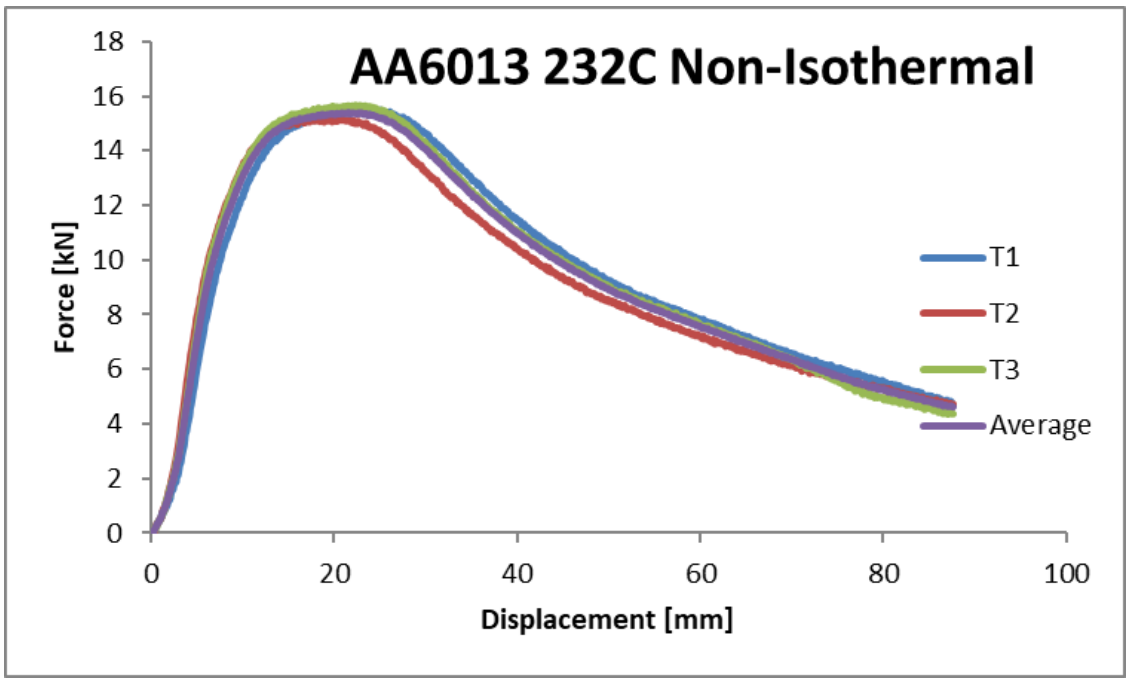
AA6013 232C Non-Isothermal
Force [kN]
Displacement [mm]
T1
T2
T3
Average

AA7xxx

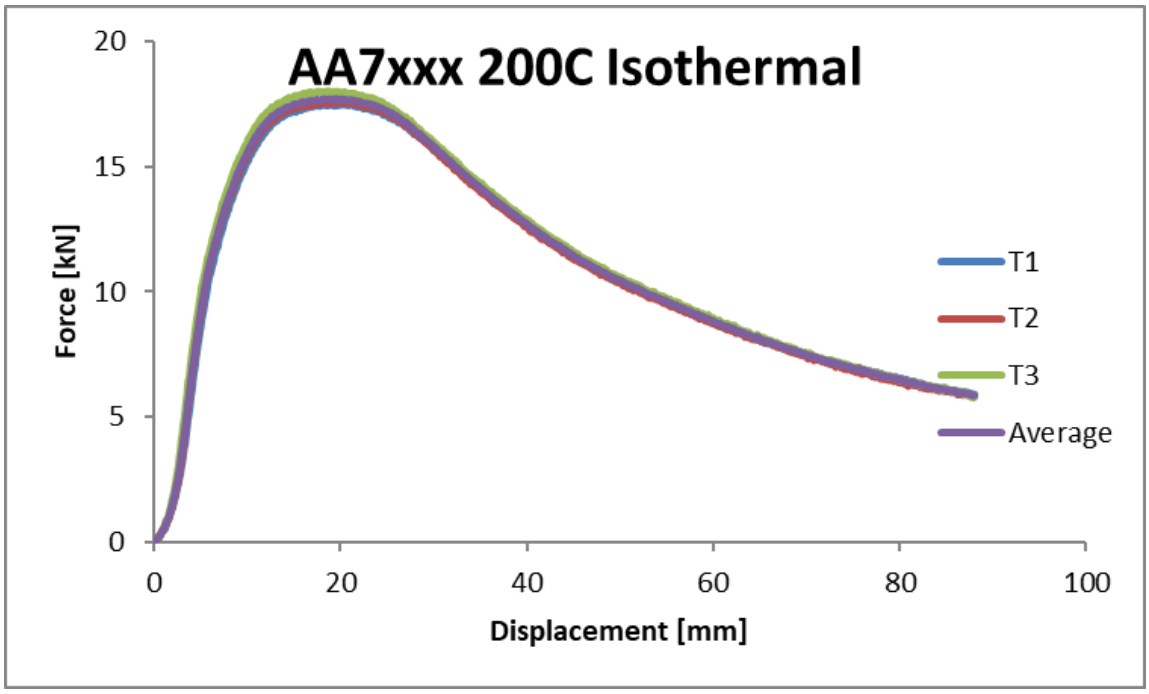
AA7xxx 200C Isothermal
Force [kN]
Displacement [mm]
0
5
10
15
20
0
20
40
60
80
100
T1
T2
T3
Average

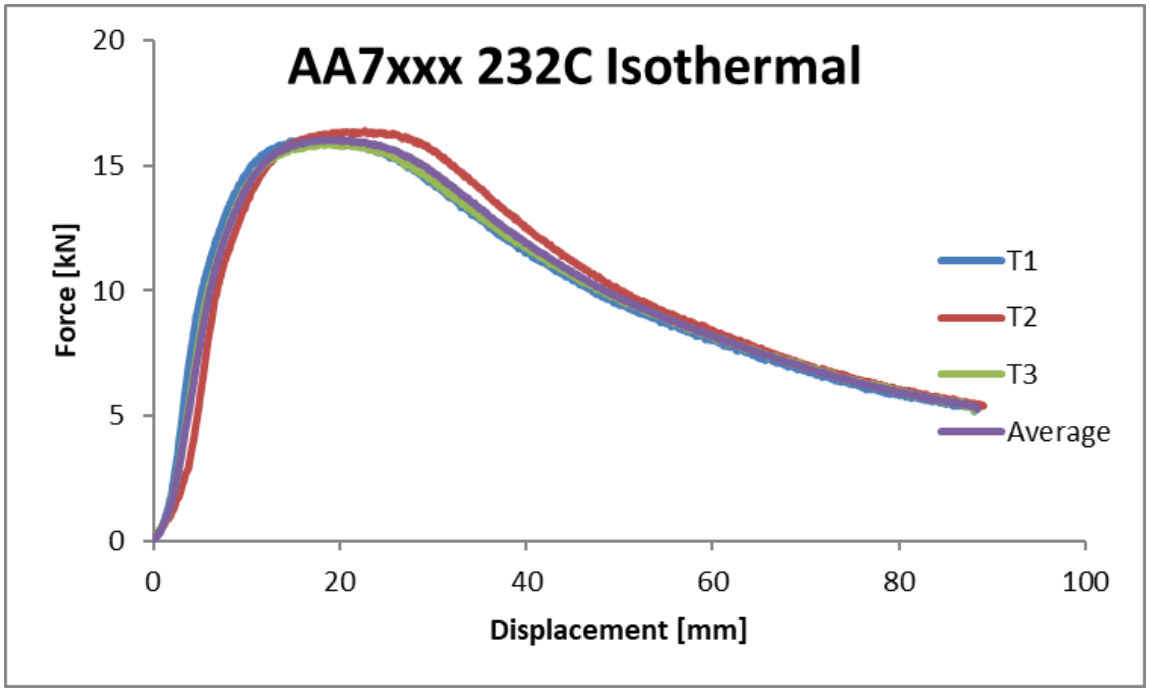
AA7xxx 232C Isothermal
Force [kN]
Displacement [mm]
0
5
10
15
20
0
20
40
60
80
100
T1
T2
T3
Average

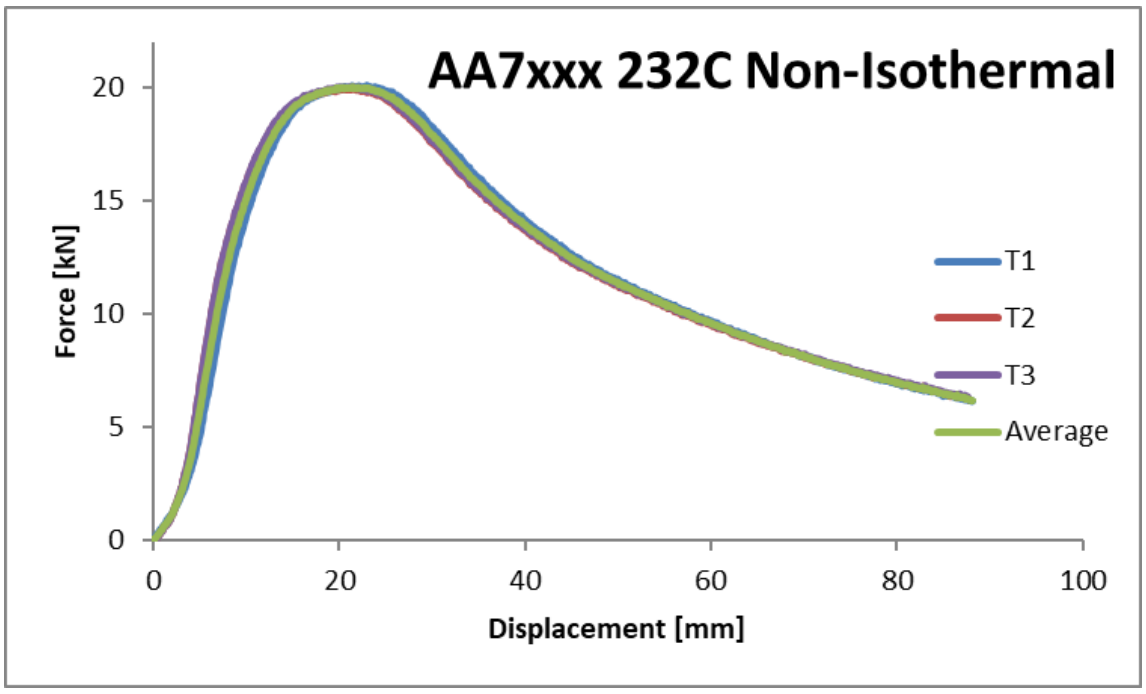
AA7xxx 232C Non-Isothermal
Force [kN]
Displacement [mm]
T1
T2
T3
Average
0
5
10
15
20
0
20
40
60
80
100

AA7075

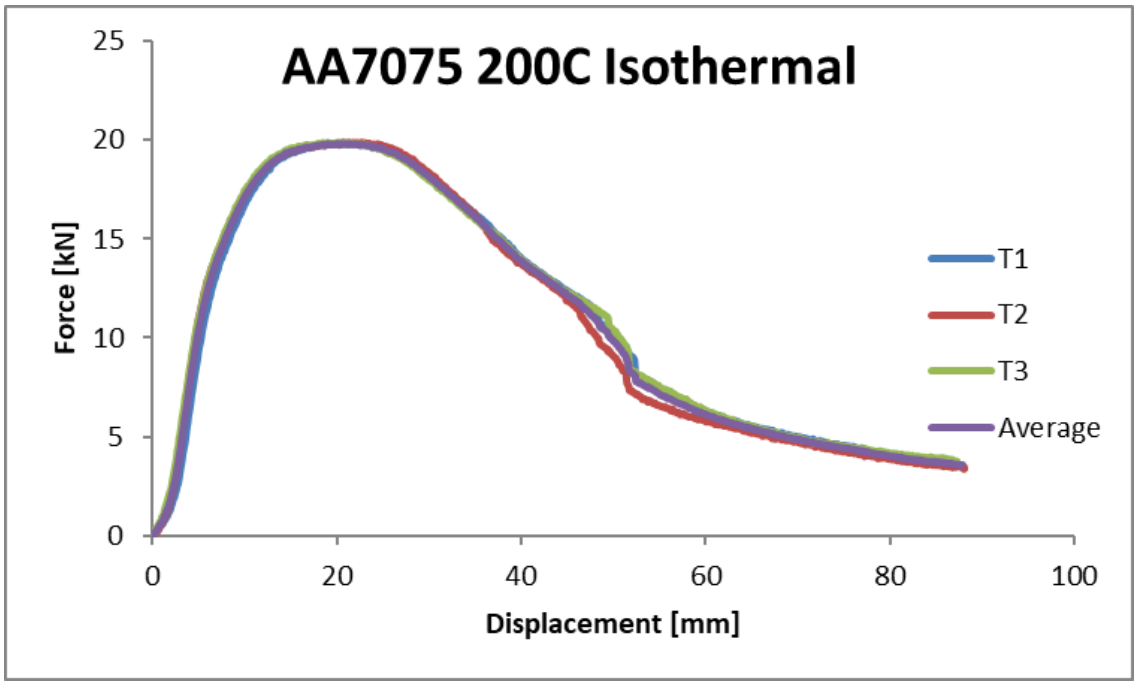
AA7075 200C Isothermal
Force [kN]
Displacement [mm]
T1
T2
T3
Average
0
5
10
15
20
25
0
20
40
60
80
100

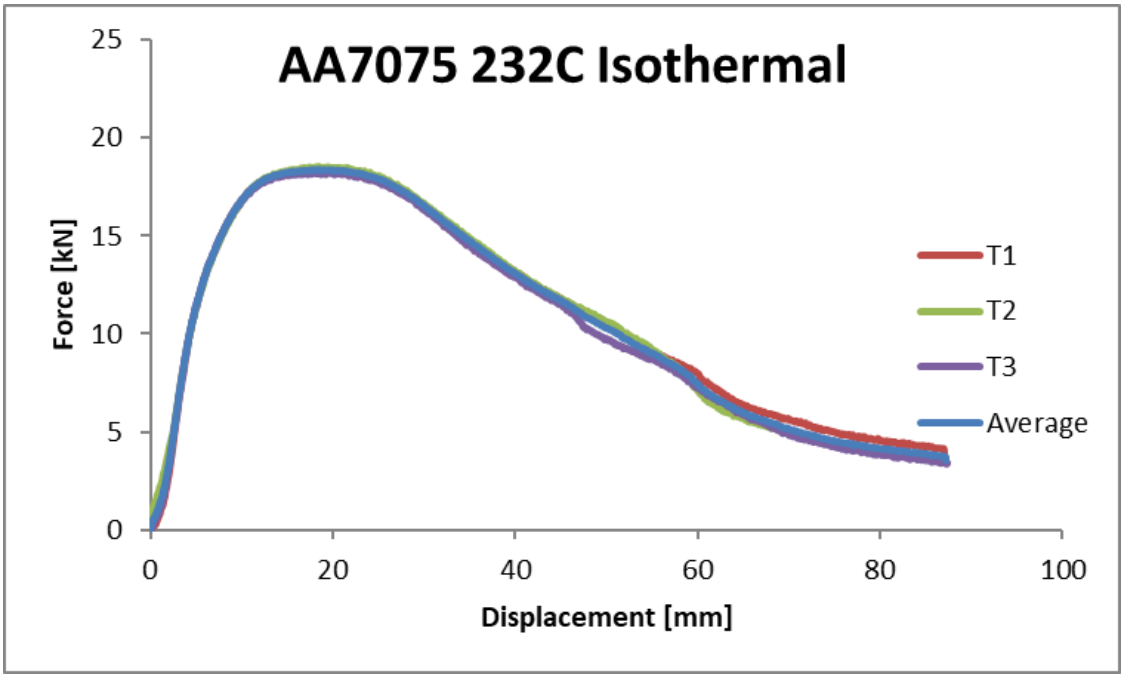

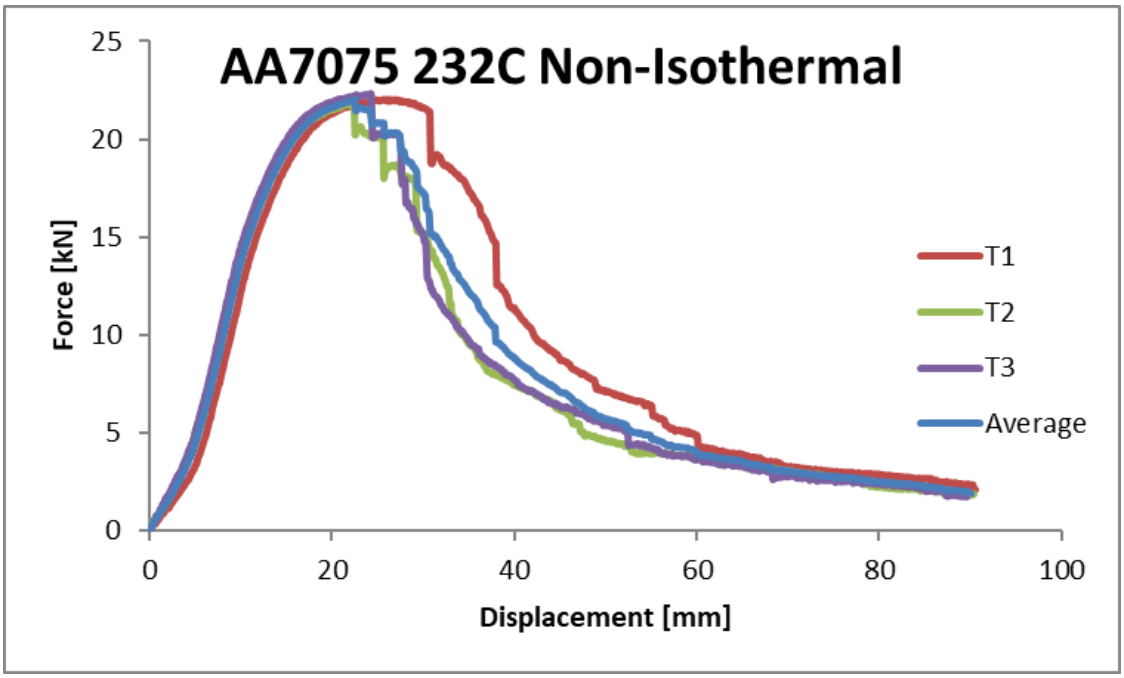

B.2 Quasi-static Die Quenched Three-Point Bend Test Data

AA7xxx

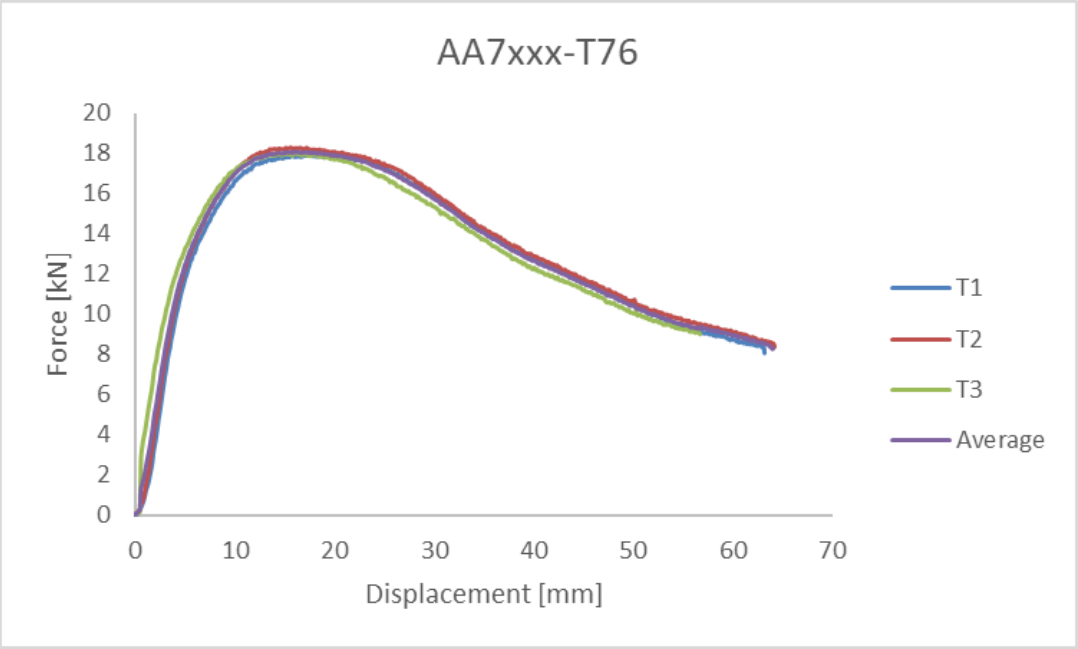
AA7xxx-T76
Force [kN]
Displacement [mm]
T1
T2
T3
Average

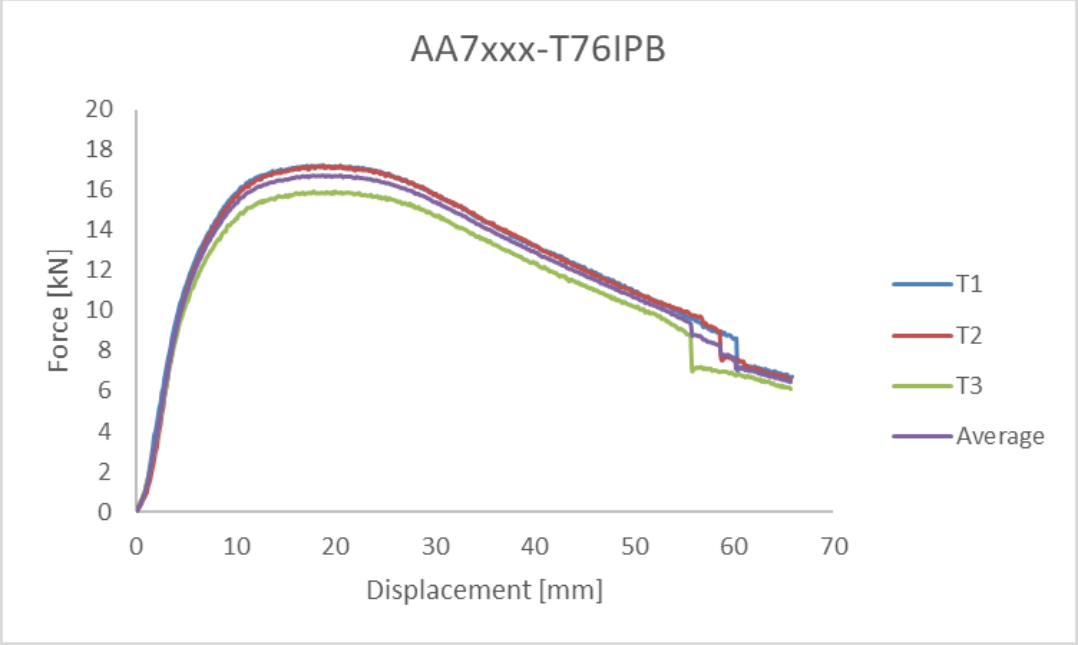
AA7xxx-T76IPB
Force [kN]
Displacement [mm]
T1
T2
T3
Average

AA7075

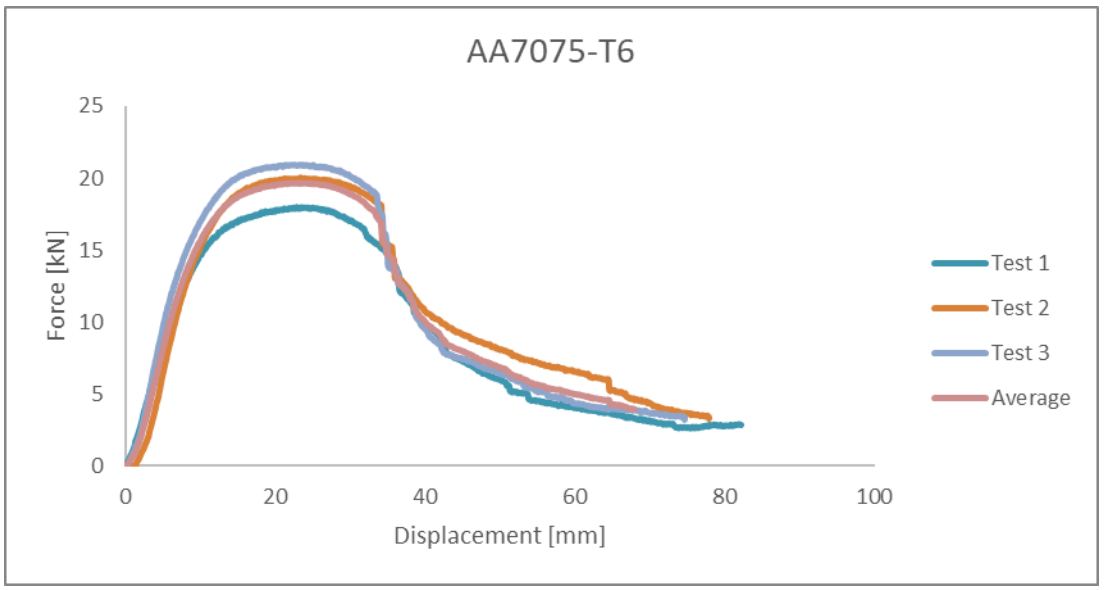

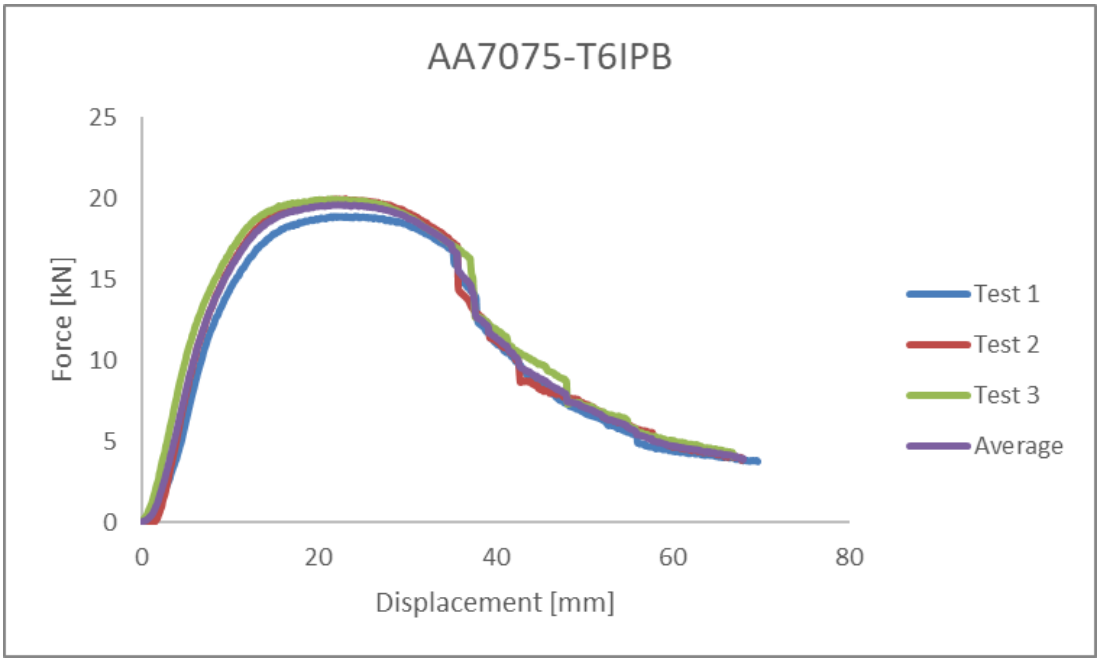

B.3 Dynamic Die Quenched Three-Point Bend Test Data

AA7xxx

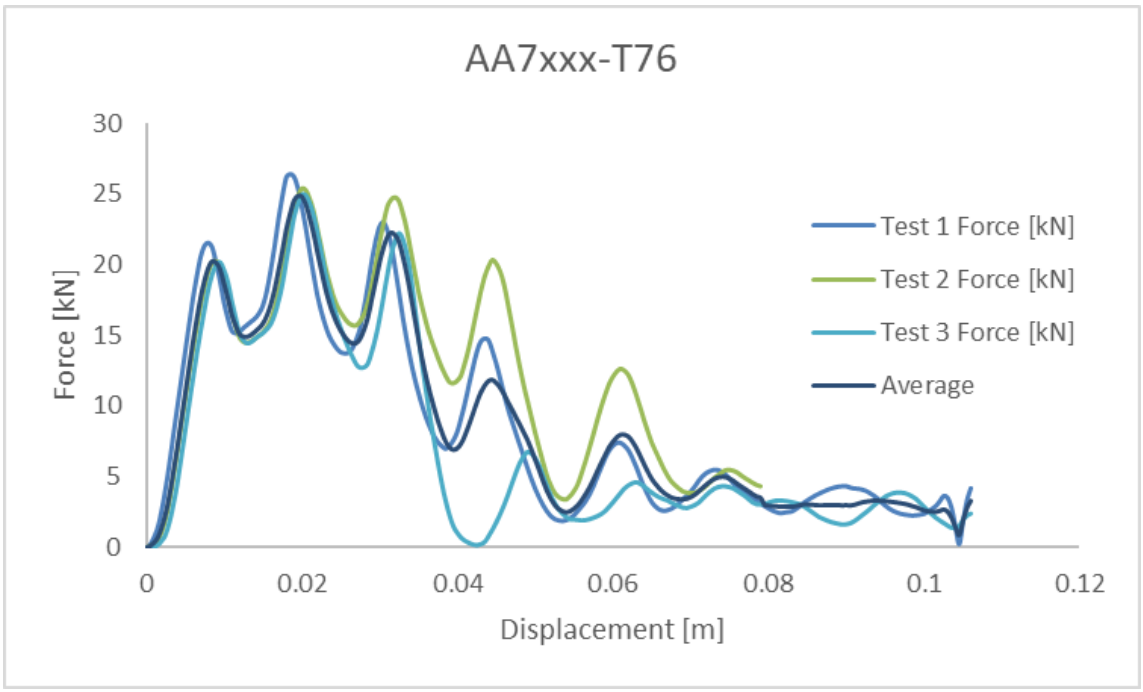
AA7xxx-T76
30
25
20
15
10
5
0
Force [kN]
0
0.02
0.04
0.06
0.08
0.1
0.12
Displacement [m]
Test 1 Force [kN]
Test 2 Force [kN]
Test 3 Force [kN]
Average

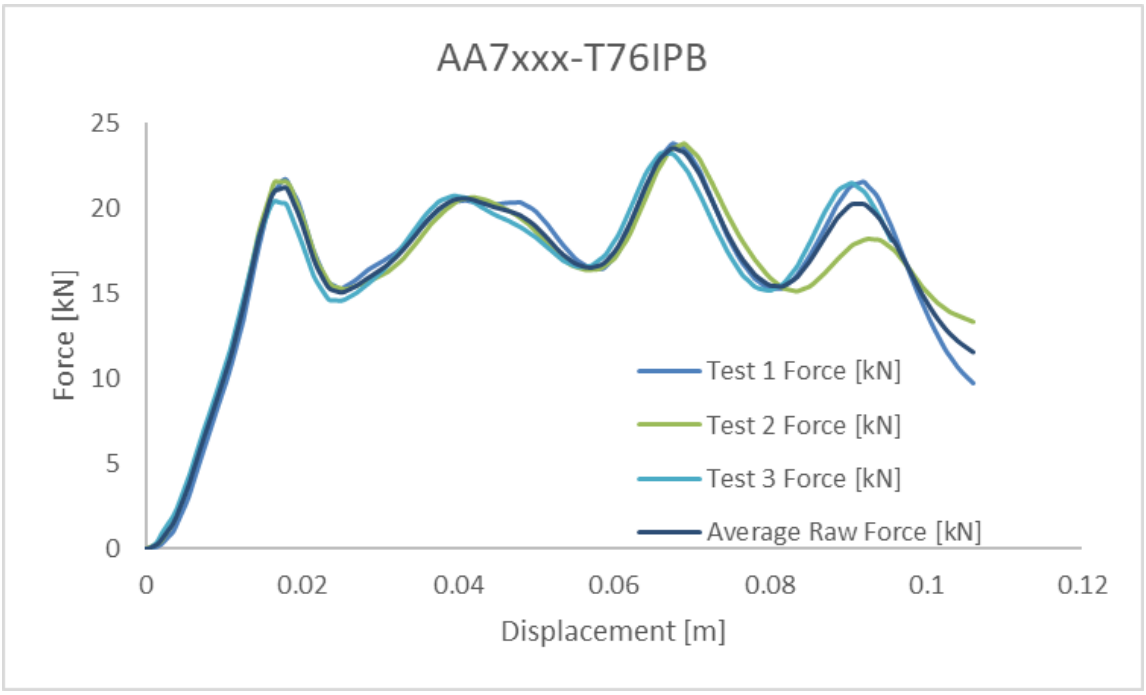
AA7xxx-T76IPB
25
20
15
10
5
0
Force [kN]
0
0.02
0.04
0.06
0.08
0.1
0.12
Displacement [m]
Test 1 Force [kN]
Test 2 Force [kN]
Test 3 Force [kN]
Average Raw Force [kN]

AA7075

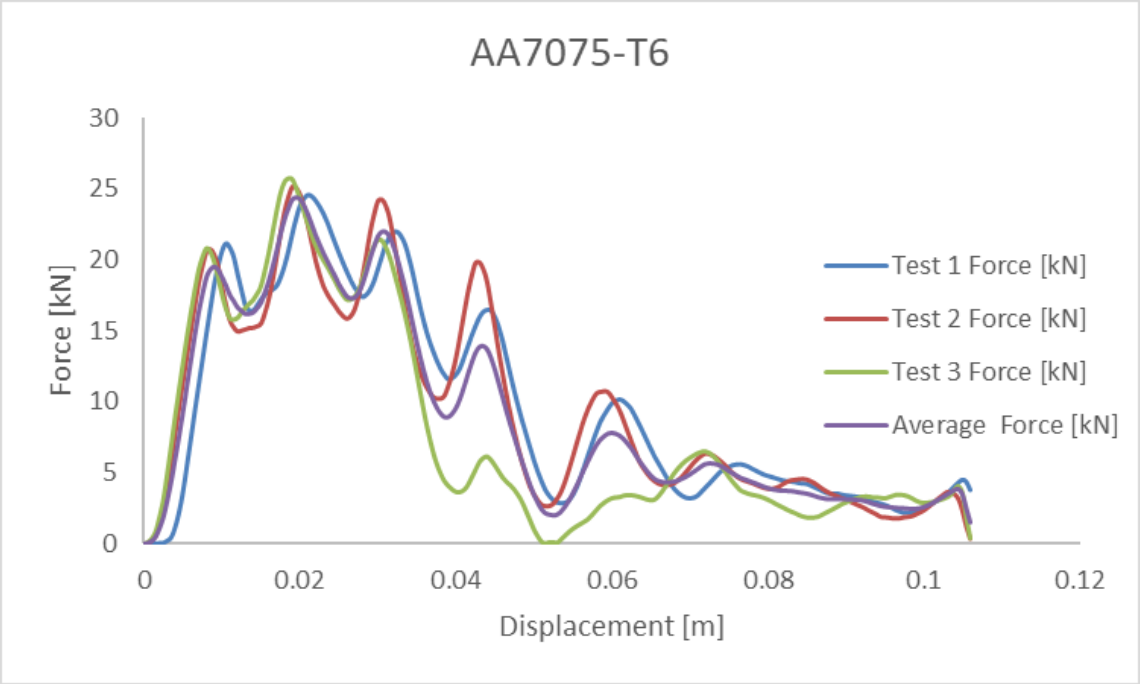
AA7075-T6
Force [kN]
30
25
20
15
10
5
0
0
0.02
0.04
0.06
0.08
0.1
0.12
Displacement [m]
Test 1 Force [kN]
Test 2 Force [kN]
Test 3 Force [kN]
Average Force [kN]

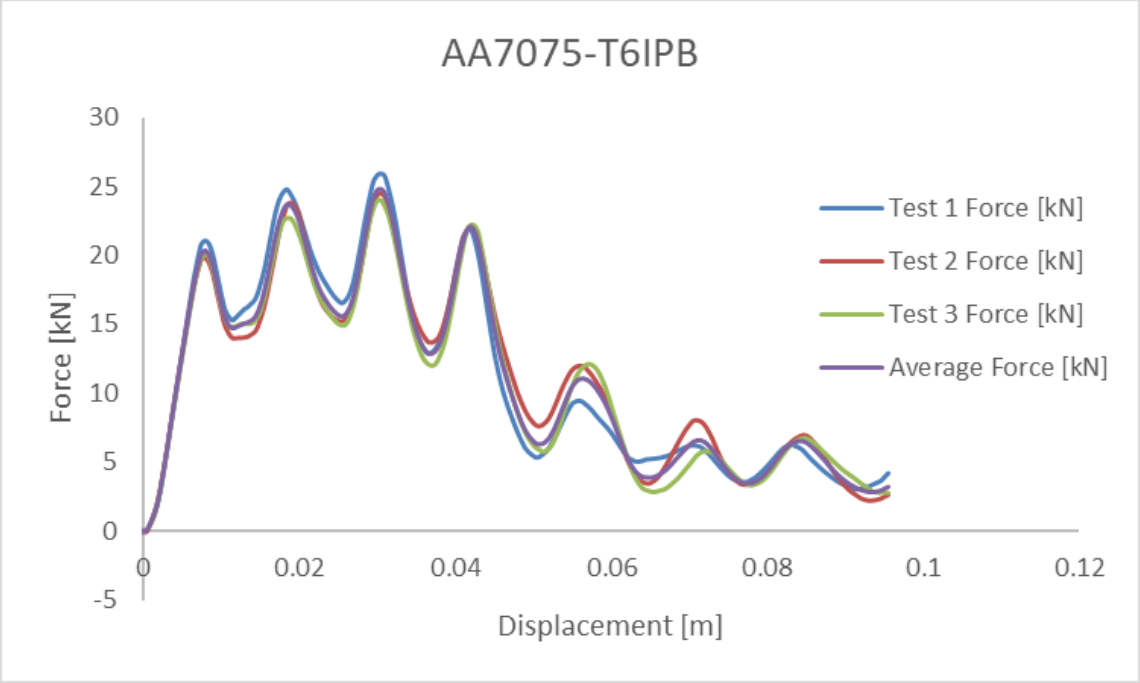
AA7075-T6IPB
Force [kN]
30
25
20
15
10
5
0
-5
0
0.02
0.04
0.06
0.08
0.1
0.12
Displacement [m]
Test 1 Force [kN]
Test 2 Force [kN]
Test 3 Force [kN]
Average Force [kN]